REVIEW ARTICLE

Check for updates

Dynamic synergy of tin in the electron-transfer layer and absorber layer for advancing perovskite solar cells: a comprehensive review

Azaharuddin Saleem Shaikh, [iD][a] Subhash Chand Yadav, [iD][a] Abhishek Srivastava, [iD][a] Archana R. Kanwade, [iD][a] Manish Kumar Tiwari, [iD][a] Shraddha Manohar Rajore, [iD][a] Jena Akash Kumar Satrughna, [iD][b] Mahesh Dhonde [iD][c] and Parasharam M. Shirage [iD] *[a]

The landscape of metal halide-perovskite solar cells (MH-PSCs) has witnessed significant progress in terms of efficiency over the past decade. Nevertheless, concerns over the toxicity of lead (Pb)-based perovskite structures have restrained their full market potential. In response, the exploration of Sn perovskites has emerged as a promising alternative, fueled by their narrow band gaps, superior carrier mobilities, low-temperature production, economic viability, and reduced hysteresis. These Sn perovskites exhibit competitive PCE while addressing the toxicity issues of Pb-based PSCs. This comprehensive review delves into the pivotal role of Sn in advancing PSCs, offering a consolidated understanding of its multifaceted applications. The report extensively examines the incorporation of Sn-based electron-transfer layers (ETLs) and absorber layers within PSCs, encompassing various dimensions, such as synthesis techniques, optoelectrical features, the future of Pb-free solar cells, integration into double PSCs, and the impact of doping strategies. Finally, this review proposes the future perspectives and investigations needed to make Sn-based PSCs a viable alternative to Pb-based MH-PSCs.

1. Introduction

Renowned for their extraordinary potential in solar cells, metal halide perovskite semiconductors have emerged as propitious materials for solar cells, attracting considerable attention since 2009. Over the past few years, the efficiency of PSCs has impressively increased from 3.8% to 26.1%,[1] rivalling the advances seen in thin-film solar cells and silicon solar cells. Leading perovskite materials, such as $MAPbI_3$, $FAPbI_3$, and mixed-cation perovskites, have emerged as candidates for high-performance solar devices.[2] However, the toxicity associated with lead-based PSCs poses a significant challenge in their widespread adoption and commercial application.[3]

Addressing this concern, the search for alternative environmentally friendly elements to replace Pb in PSCs has gained importance.[4] Suitable metal elements should be able to produce a stable perovskite crystal structure; typically exhibiting an

ABX3 structure, where A is a monovalent organic or inorganic cation, B is a coordinate divalent metal ion, and X can be any halogen like Cl^-, Br^-, or I^-.[5] To obtain a stable perovskite structure, precise ionic radii (*r*) of A, B, and X ions are essential, as determined by the tolerance factor:[6,7]

$$t = \frac{(r_A + r_B)}{(\sqrt{2}(r_B \times r_X)}$$

The optimal range for the tolerance factor (*t*) lies between 0.813 and 1.107; if it deviates from this range, the crystal structure, resembling a cubic structure, would experience deformation, distortion, and eventual disintegration of the perovskite structure.[8] ABX3 perovskites exhibit exceptional optoelectronic properties, making them a favored option for photovoltaic (PV) devices. However, only a few selected metals, such as Cu, Ge, Bi, Sn, and Sb, possess the potential to replace Pb in the synthesis of metal hybrid perovskites.[9] Over the last five years, among the limited range of metals suitable for replacing Pb in perovskite synthesis, Sn has emerged as the most promising candidate.[10] Sn perovskites exhibit enhanced optoelectronic properties, such as a higher and narrower optical band gap (~ 1.3 eV) and higher total charge-carrier mobilities (~ 2 cm^2 V^{-1} s^{-1}). The utilization of Sn in lead-free perovskites stems from its valence electron set-up, which closely resembles Pb.

[a] *Department of Metallurgical Engineering and Materials Science, Indian Institute of Technology Indore, Simrol, Khandwa Road, Indore 453552, India.*
E-mail: pmshirage@iiti.ac.in, paras.shirage@gmail.com

[b] *Department of Physics, Indian Institute of Technology Indore, Simrol, Khandwa Road, Indore 453552, India*

[c] *Department of Physics, Medi-Caps University, Pigdamber, Rau, Indore, Madhya Pradesh 453331, India*

Additionally, the ionic radius of Pb^{2+} (119 pm) is similar to that of Sn^{2+} (115 pm). This similarity in ionic radii between Pb and Sn makes Pb suitable for this particular application. Moreover, Sn possesses a lower electronegativity (Sn^{2+} with 1.96) than Pb (Pb^{2+} with 2.33).[11] As a result, Sn perovskites can produce an increased short-circuit current density (J_{sc}), moving closer to the theoretical upper limit of efficiency (known as the Shockley–Queisser efficiency limit for single-junction solar cells), which stands at approximately 33%.[12] Unlike Pb perovskites, Sn perovskites display minimal toxicity and can breakdown into environmentally friendly SnO_2 upon air exposure. This characteristic dramatically enhances their attractiveness for producing top-notch, lead-free PSCs with exceptional performance.[13]

In 2014, Snaith et al. pioneered the utilization of $MASnI_3$ as a light-absorbing material in PSCs, yielding a remarkably promising power conversion efficiency (PCE) of 6.4% within a mesoporous structure.[14] This ground-breaking achievement has since sparked substantial interest in Sn perovskites, fuelling extensive research to attain high-performance Sn-based PSCs. Indeed, Sn-based PSCs have received considerable research attention, approximating to the efforts that boosted Pb-based perovskites. Despite their low PCEs and vulnerability of Sn to oxygen and moisture in the ambient atmosphere, which can lead to structural transitions and difficulty in creating pinhole-free films, extensive research has been done globally to develop Sn-based PSCs as an alternative to Pb-based PSCs. Notably, $CsSnI_3$, $CH_3NH_3SnI_3$ ($MASnI_3$), and $(NH_2)_2CHSnI_3$ ($FASnI_3$) have been prevalently used in PSCs, and the best-reported PCEs for these devices have reached approximately 7.5%, 12.5%, and 14.1%, respectively,[15] indicating high performance even with reduced or Pb-free Sn-based perovskites. The ongoing work in tin-based perovskite research promises to lead the way toward safer, more efficient, and eco-friendly solar cell technologies, thereby contributing significantly to the sustainable development of renewable energy.

Apart from its usage in Pb-free PSCs, Sn oxide (SnO_2) has emerged as a preferable choice for the ETL in PSCs, gaining significant attention due to its various advantages,[16] including: (i) SnO_2 possesses an acute conduction band (CB) with favourable energy levels and band alignments. The ETL–perovskite interface actively enhances the extraction of electrons and effectively prevents the movement of holes. Also, it may help to reduce interfacial strain (by reducing the lattice mismatch) induced during the synthesis process; (ii) SnO_2 possesses a wide optical bandgap (~ 3.6 eV), which can block UV-light infiltration while allowing excellent transparency throughout the visible range. As a result, a significant portion of light can effectively infiltrate and be assimilated by the perovskite film; (iii) SnO_2 displays remarkable bulk electron mobility, reaching 240 $cm^2\,V^{-1}\,s^{-1}$, coupled with exceptional conductivity ($\sim 7.5 \times 10^{-6}$ S cm^{-1}). These characteristics promise to improve electron transport effectively while reducing recombination disadvantages; (iv) SnO_2 demonstrates remarkable chemical stability, resistance to UV-light filtration, and reduced photocatalytic activity compared to materials like titanium dioxide (TiO_2) and other ETLs, which are critical for maintaining

devices' overall stability and reliability; and (v) SnO_2 is ideally suited to low-temperature processing (<200 °C), making it ideal for flexible solar cells, tandem solar cells, and a wide range of commercial perspectives.

Herein, we comprehensively present an overview of the recent progress, remaining challenges, and future perspectives concerning the potential applications of Sn-based ETLs and absorber layers to be utilized in Pb-free PSCs. The review begins by describing and discussing the various synthesis procedures aimed at making high-quality Sn-based perovskite films, focusing on their impact on the performance and operational stability of PSCs. In addition, a comprehensive assessment of the structural, electrical–optical, and modification methodologies, as well as current breakthroughs in SnO_2-type ETLs and their significance in PSCs, are discussed. Further, this review thoroughly explores the emerging field of Sn-based perovskites in solar cell applications. In contrast to the prevailing focus on metal halide perovskite semiconductors, it uniquely emphasizes the potential of Sn as a promising lead-free alternative. This review meticulously examines the intricacies, offering a comprehensive understanding of the challenges and opportunities for replacing Pb with environmentally friendly elements. Notably, it goes beyond Sn perovskites' light-absorbing properties to discuss their application as an ETL, strategically highlighting the advantages of SnO_2 in this area. This dual focus, addressing Sn perovskites as both ETLs and absorber layers, provides a holistic perspective on the potential application of Sn perovskites in solar cell technologies. The article's distinctive approach, seamlessly integrating historical perspectives, material properties, synthesis approaches, and potential applications, positions it as a valuable resource for potential readers exploring the evolving landscape of Pb-free PSCs.

2. Role of Sn in the ETL

In recent years, there has been an increasing interest in employing SnO_2 as an ETL in PSCs. Despite the initial challenges faced by SnO_2 in organic solar cells and dye-sensitized solar cells compared to zinc oxide (ZnO) and TiO_2, the landscape shifted significantly in 2015, when several research groups independently introduced SnO_2 into PSCs and reported notable improvements in device efficiency. For example, Ma et al. and Kuang et al. reported efficiencies of 7.43 and 14.69%, respectively.[17,18] Despite these advancements, challenges related to charge traps and recombination centres, such as oxygen vacancies resulting from high-temperature annealing at 450 °C, were initially encountered in SnO_2-based PSCs. To address these issues, researchers developed low-temperature processing methods for SnO_2. For instance, Tian et al. achieved a PCE of 13% by spin-coating SnO_2 nanoparticles and annealing at 200 °C.[19] Fang et al. reported a noteworthy 17.21% efficiency using a low-temperature thermal decomposition process at 180 °C.[20] Additionally, Hagfeldt and colleagues employed a low-temperature atomic layer deposition (ALD)

approach, achieving a PCE of over 18% with the open-circuit voltage (V_{oc}) exceeding 1.19 V.[21]

Building on these findings, recent breakthroughs by You's group[22] demonstrated a certified efficiency of 19.9%, utilizing high-quality SnO_2 nanocrystal colloids annealed at a moderate temperature of 150 °C. Recent developments, including meticulous control of the surface passivation layers and interface modifications, have propelled SnO_2-based PSCs to efficiencies surpassing 21.6%.[23–26] Moreover, the competitiveness of SnO_2 with TiO_2 in terms of performance is underscored by recent studies. Noteworthy achievements include planar PSC architectures with PCEs exceeding 21% and exceptional stability, retaining 82% of the original PCE after 60 h of use. Other configurations, such as SnO_2/PCBM composites and SnO_2 alloyed with c-TiO_2, have reported PCE values surpassing 19%.[27,28] The favourable optoelectronic properties of SnO_2 make it a compelling candidate for the ETL in PSCs.[29–32] Low-temperature processed SnO_2 has demonstrated great promise, showing a PCE of 13% with high stability. Chemical treatments and surface modifications, including elemental doping, surface passivation, and bilayer structures, have further elevated the performance of SnO_2-based PSCs.[20,33–35] The evolving role of SnO_2 as an ETL in PSCs reflects the substantial progress in the use of SnO_2, with recent accomplishments showcasing its potential to compete with TiO_2-based devices. Ongoing research endeavours are aiming to refine SnO_2-based PSCs through innovative approaches, setting the stage for improving the efficiency and stability of next-generation solar cell technologies.

2.1. Synthesis methods for SnO_2

Various synthesis techniques are utilized for SnO_2 thin films, including sol–gel, hydrothermal, sonochemical, microwave-assisted, ALD, chemical vapour deposition (CVD), and sputtering techniques. The sol–gel method involves converting a precursor sol into a solid gel, offering good film thickness and composition control. Hydrothermal synthesis uses high-pressure and high-temperature conditions to promote film growth with improved crystallinity. Sonochemical and microwave-assisted methods utilize ultrasonic or microwave irradiation to enhance the nucleation and crystallization processes. ALD enables a precise and conformal film deposition, while CVD allows large-scale production. Sputtering offers excellent uniformity and composition control. Understanding the characteristics and experimental conditions of each method is vital for tailoring SnO_2 films to specific applications.

2.1.1. Sol–gel method. The sol–gel method is versatile for producing solid materials by inducing gelation in solution. It offers various possibilities for creating various morphologies with practical applications.[36–38] A suspension of particles or polymer molecules in a liquid is considered as a sol. At the same time, gelation occurs when the interactions among sol components become strong enough to immobilize the liquid.[39] Different materials can be formed using the sol–gel method, as shown in Fig. 1.

In materials synthesis, gelation typically involves the irreversible establishment of covalent bonds. When the solution

Fig. 1 Graphical overview of the sol–gel method and its potential applications.

experiences gelation, it culminates in creating unified materials. These gel frameworks can undergo additional treatment through meticulous dehydration and heating, fabricating top-notch ceramic or glass structures. Alternatively, supercritical solvent extraction permits highly porous and lightweight unified forms. Gelation can also occur during various processing stages, frequently via the evaporation of solvents, which yields valuable materials. For instance, films created through spinning or dipping encounter gelation during the drying phase and can subsequently be subjected to heating to generate compact films. Spherical particles can be produced by spray drying, while fibres may emerge through spinning accompanied by evaporation. Furthermore, the introduction of templating agents enables the utilization of gelation to fashion nanoporous materials and other nanostructures, like tubes, fibres, helices, and ribbons.[40–43]

Films of SnO_2 were generated through a spin-coating technique, involving the application of SnO_2 organic sol onto pristine substrates at 5000 rpm for 30 s, followed by sintering at 450 °C for 2 h. The SnO_2 organic sol was derived by dissolving $SnCl_2 \cdot 2H_2O$ in absolute ethyl alcohol, stirring at 80 °C for 3 h, ageing, and subsequently employing it to coat the films at different concentrations. The optimal concentration was found to be 0.5 M.[44] The SnO_2 ETLs were formed through a solution-based spin-coating technique using $SnCl_2 \cdot 2H_2O$ precursor solution, followed by thermal annealing at 180 °C for 1 h and UV-ozone treatment. This low-temperature process yielded excellent SnO_2 ETLs, resulting in efficient PSCs. Also, the method is compatible with low-cost, roll-to-roll manufacturing on flexible substrates.[45] In a separate investigation, SnO_2 nanoparticles were fabricated through a process involving the reaction of $SnCl_4 \cdot 5H_2O$ and aqueous TMAH in ethanol. Ultrasonic treatment was then applied, followed by hydrothermal synthesis at 200 °C for 12 h. The outcome was the formation of layers of SnO_2 through spin-coating a precursor solution at 2000 rpm, leading to the development of layers with an approximate thickness of 120 nm. This layer of SnO_2 could serve as an effective material for transporting electrons in PSCs. The cells achieved an impressive PCE of 18.8%. Notably, even after being stored under standard environmental conditions for 30 days, the SnO_2 layer maintained its initial PCE at a level

exceeding 90%. This underscores the improved stability of the SnO$_2$ layer.[46] Using a different approach, a colloidal solution of SnO$_2$ quantum dots (QD) was created, resulting in a substantial increase in the PSC of 20.1%. This advancement was due to the remarkable optical and electronic characteristics of the ETL based on SnO$_2$ QDs. Experimental assessment illustrated the elevated efficiency of solar cells with this material due to the augmentation of electron extraction and mitigation of charge recombination. The most suitable solution concentrations and ratios for optimal efficacy were also determined.[47]

Gu *et al.* successfully prepared SnO$_2$ nanopowders through a hydrous Sn chloride dissolution method, followed by the controlled dropwise addition of 2 M aqueous ammonia solution. The SnO$_2$ nanopowders exhibited a quantum confinement effect, leading to a higher energy absorption edge as the particle size decreased. Samples treated at different temperatures showed varying absorption positions, indicating direct electron transitions in the SnO$_2$ nanocrystals.[48] Also, in the work of Adnan *et al.*, a sol–gel synthesis of SnO$_2$ nanoparticles involved mixing Sn(IV) chloride with water, then gradually adding ammonia solution and stirring for 2 h before ageing the solution. The gel obtained was rinsed, dried, and subjected to calcination at 400 °C. This simple method resulted in the creation of nanoparticles of SnO$_2$ showcasing a significant surface area.[49] Zhang *et al.* employed a sol–gel method to synthesize SnO$_2$ nanoparticles by adding 8 mol L^{-1} of HNO$_3$ to a granulated Sn and citric acid mixture. This addition stabilized the precursor solution, resulting in smaller, evenly shaped SnO$_2$ particles after calcination at different temperatures. The study highlighted the potential of this straightforward approach for controlling the production of SnO$_2$ nanoparticles with desirable properties.[50] Aziz *et al.* used a process involving dissolving hydrated Sn chloride in pure ethanol and stirring for 30 min,

followed by adding acetylacetone to initiate the hydrolysis of SnO$_2$. The solution was refluxed at 80 °C for 5 h to form the SnO$_2$ solution. The researchers introduced polyethylene glycol (PEG) as a chemical modifier to control the nanoparticle size and aged the solution for 72 h. Subsequently, the solution was dried at 100 °C for 30 min and subjected to calcination at 450 °C and 600 °C for 1 h, forming SnO$_2$ nanoparticles. By adjusting the calcination temperature and the molecular weight of the PEG, the nanoparticle size could be precisely controlled. This method is a solid foundation for future studies focusing on synthesizing metal oxide nanoparticles with a controlled size and shape, paving the way for various applications in various fields.[51] Table 1 summarizes the synthetic conditions and improved results obtained with sol–gel methods in some studies.

Table 2 compares devices utilizing SnO$_2$ layers as the ETL, synthesized through the sol–gel method. The FTO/SnO$_2$/MAPbI$_3$/spiro-OMeTAD/Au configuration seems to be the most favourable option, with a higher V_{oc}, improved FF, and superior PCE compared to the FTO/SnO$_2$-ESL/perovskite/HTM/Ag structure. However, the latter configuration exhibited a higher J_{sc}, indicating efficient light absorption and carrier generation. Further optimization efforts could focus on enhancing the FF and overall device performance of both structures. These discoveries emphasize the importance of carefully selecting materials and designing device structures when aiming for higher performance in PSCs. Ongoing exploration and progress in this domain are needed for enhancing the effectiveness and economic feasibility of these technologies within the realm of renewable energy applications.

2.1.2. Hydrothermal method. The hydrothermal synthesis process involves creating single crystals by taking advantage of the ability of the desired material to dissolve in hot water under

Table 1 Overview of the precursors and synthesis conditions used in the sol–gel method

Precursors	Synthesis conditions	Result	Ref.
SnCl$_2$·2H$_2$O and ethyl alcohol	Sol temp.: 80 °C Stirring: 3 h Ageing: 3 h	Minimized the occurrence of a charge shunt pathway	44
SnCl$_2$·2H$_2$O and ethyl alcohol	Sol temp.: 80 °C Annealing temp.: 180 °C for 1 h	Surface becomes uniform, hence having a positive impact on light transmission	45
SnCl$_4$·5H$_2$O and TMAH in ethanol	Sol temp.: 100 °C for 12 h	High degree of crystallinity, effective electron transfer, and enhancement in the stability of the devices against oxygen and water	46
SnCl$_2$·2H$_2$O and CH$_4$N$_2$S in deionized water	Sol temp.: RT Ageing: 2 days	97% transmission in visible light	52
SnCl$_4$·5H$_2$O and ammonia solution	Sol temp.: 80 °C Annealing temp.: 400 °C, 500 °C, and 600 °C for 2 h	Increased absorption edge energy due to the quantum confinement effect	48
SnCl$_4$·5H$_2$O and ammonia solution	Sol temp.: 30 °C to 90 °C Stirring: 2 h Ageing: 24 h Calcination: 400 °C for 2 h	Formation of numerous small nuclei results in a larger sample surface area	49
Granulated tin, citric acid, nitric acid, aqueous ammonia	Sol temp.: 100 °C Drying: 100 °C for 5 h in air Calcination: 300 °C for 2 h, 400 °C for 2 h, 500 °C for 2 h	Reduction in particle size	50
SnCl$_2$·2H$_2$O and ethyl alcohol, acetylacetone, PEG	Sol temp.: 80 °C for 5 h Ageing: 72 h Drying: 100 °C for 0.5 h Calcination: 450 °C for 1 h and 600 °C for 1 h	Control over the size of particles	51

Table 2 Comparison of different device structures utilizing SnO₂ layers using the sol–gel method and their respective solar cell parameters

Device structure	V_{oc} [V]	J_{sc} [mA cm^{-2}]	FF [%]	PCE [%]	Ref.
FTO/SnO₂-ESL/MAPbI₃/HTM/Ag	0.86	30.99	0.39	10.33	44
FTO/SnO₂/MAPbI₃/spiro-OMeTAD/Au	1.11	22.83	0.64	16.02	45
FTO/NiO/MAPbI₃/C₆₀/SnO₂NCs/Ag	1.12	21.8	0.77	18.8	47
ITO/P3CTK/MAPbI₃/PC₆₁BM:SnO₂/Al	1.12	23.13	0.72	18.7	53
ITO/PEN/SnO₂QD-ESL/CsMAFA/spiro-OMeTAD/Au	1.12	23.55	0.78	20.3	52

elevated pressure. This approach involves the growth of crystals within a sealed autoclave, which is a steel pressure vessel. The typical procedure is shown in Fig. 2. Hydrothermal synthesis has garnered significant attention in SnO₂ thin-film deposition, enabling the production of nanocrystals with precise control over the crystal sizes, excellent dispersibility in solutions, and the ability to achieve diverse morphologies.[54,55] Table 3 presents the reaction conditions employed in the hydrothermal method, including details about the reagents used and morphological characteristics. This method employs an aqueous solvent within a closed system, thus demonstrating environmental friendliness. Notably, one of its notable advantages over other solution-based routes lies in its ability to obtain the final product at a relatively low temperature without calcination. Additionally, meticulous control over the composition, morphology, and purity is facilitated by the hydrothermal method, thus allowing fine crystalline structures with the desired phase to be attained.[56]

The hydrothermal method, leveraging its unique capacity to engineer SnO₂ thin films with tailored properties, presents a promising avenue for a wide range of applications, encompassing sensing devices and energy-storage systems. By harnessing the advantages offered by hydrothermal synthesis, researchers can forge ahead in developing SnO₂ thin films characterized by enhanced functionality and performance, thereby contributing to significant advancements across various technological domains.[63]

Significant advancements in SnO₂ synthesis have been achieved using the hydrothermal method. Through a hydrolysis reaction, ultrathin single-crystalline nanorods of SnO₂ were synthesized by Ye *et al.*, showcasing a nonclassical crystallization process. Zeng *et al.* successfully fabricated hierarchical flower-like SnO₂ architectures using a hydrothermal route, as shown in Fig. 2, with the assistance of solid citrate and PEG 600, elucidating the role of chelate complex formation and soft templates. Cheng *et al.*[62] created SnO₂ nanorods with a preferred (001) growth direction and high aspect ratio. Hussain *et al.* achieved the catalyst-free growth of SnO₂ micro-sheets, with the thickness increasing as the reaction temperature rose.[64] Guo *et al.* demonstrated the fabrication of hierarchical SnO₂ nanostructures using shuttle-shaped nanosheets that transformed into cone-shaped and rod-shaped structures under thermal treatment.[65] Wang *et al.* reported controlling the size and morphology of SnO₂ nanoparticles through solution adjustments.[66] A novel biomolecule-assisted hydrothermal method for synthesizing sub-10 nm SnO₂ nanocrystals with exceptional photocatalytic performance, addressing significant challenges in nanoparticle synthesis and offering a highly efficient approach for organic dye degradation.[67] Yin *et al.* investigated the influence of the reaction conditions on the SnO₂ nanocrystal morphology using L-lysine.[68] Wang *et al.* investigated a hydrothermal method to obtain nanoflowers of SnO₂ at a large scale.[69] Zhang *et al.* developed a simplistic method for SnO₂ microsphere synthesis.[70] Lou *et al.* reported the synthesis of hierarchical SnO₂ structures from nanosheets.[71] Maksimov *et al.* obtained SnO₂ nanocrystals with diverse morphologies *via* a hydrothermal synthesis.[72] Talebian *et al.* explored the role of surfactants in controlling the morphology of SnO₂.[73] Lee *et al.* utilized a solvothermal synthesis to create a hollow core–shell mesosphere composed of SnO₂ nanoparticles.[74]
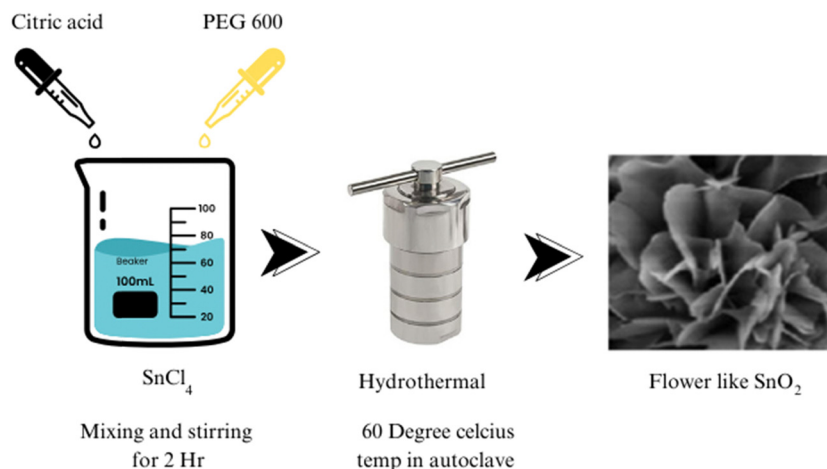

Fig. 2 Synthesis of a flower-like morphology of SnO₂ using the hydrothermal method.

Table 3 Reaction conditions for the hydrothermal method, reagents, and morphological characteristics

Reaction temp. (°C)	Reaction time (h)	Basic reagents	Morphology	Ref.
240	15	$SnCl_4 \cdot 5H_2O$, lysine	Nanoparticles	57
250	24	$SnCl_4 \cdot 5H_2O$, CTAB, Triton X-100, sodium hydroxide, sodium dodecyl sulphate	Nanoparticles	58
200	18	Urea, $SnCl_2 \cdot 2H_2O$, NaOH	3D nano spheres	59
140	16	SnCl, NH_3, NaOH	Nanorods	60
140	24	$SnCl_4 \cdot 5H_2O$, NaOH, CTAB	Nanosheets	61
150	24	$SnCl_4 \cdot 5H_2O$	Nanorods	62

2.1.3. CVD method. CVD has emerged as a highly effective method for synthesizing nanostructured materials with exceptional purity and performance by exposing a substrate to volatile precursors. CVD aids in the interaction and/or breakdown of the nanostructured materials on the substrate's surface, leading to the intended creation of deposits. CVD offers numerous advantages compared to other deposition techniques, making it an attractive choice for nanostructure production.

Uniform distribution over large areas can be achieved by CVD, ensuring a consistent deposition of the desired material, which is particularly beneficial when homogeneity across the substrate is essential. Additionally, CVD enables the deposition of materials without compositional gradients, ensuring uniformity throughout the deposited layer.[75–77] The CVD procedure utilizes a heated furnace that can attain elevated temperatures, a critical factor facilitating effective reactions and/or the breakdown of volatile precursor materials on the substrate's surface, which culminates in the desired formation of deposits. A pressure sensor is integrated into the system to ensure precise control and monitoring during the CVD process. This sensor helps maintain the optimal pressure conditions within the furnace, essential for achieving a consistent and uniform deposition of the desired material. In the CVD set-up, the substrate, typically a wafer, is vertically placed to facilitate the deposition process. This vertical orientation allows for better substrate exposure to the volatile precursors, improving deposition efficiency and uniformity. The process may involve the liberation of gases during the chemical reactions, and so a vacuum pump is employed to manage these gases and maintain controlled conditions. The vacuum pump helps create and sustain the required vacuum environment within the furnace, which is necessary for the CVD process to proceed effectively.[63,78,79] The overall set-up and components of the CVD process, including the heated furnace, pressure sensor, vertically placed wafer for deposition, and vacuum pump, are depicted in Fig. 3.

In synthesizing SnO_2 nanostructures, CVD offers a simple and efficient technique. By evaporating targets, such as Sn, SnO, and SnO_2, at varying temperatures, a wide range of SnO_2 nanostructures can be prepared. Hierarchical nano-homojunctions and nano-heterojunctions were achieved with controlled growth by Sun et al.,[80] using a multistep thermal vapour deposition route. On the exterior of the single-crystal SnO_2 nanobelt bases, multiple aligned SnO_2 nanowires or nanobelts were cultivated through a catalyst-free vapor–solid (VS) growth process. The successive development of nanowire or nanobelt levels allowed for a theoretically limitless structure complexity, with different lengths, sizes, and chemical compositions at each branch level. SnO_2 nanostructures with various morphologies were synthesized by Ge et al.[81] using a catalyser-assisted CVD method, and it was noted that the quality of the SnO_2 nanowires could be considerably impacted by the temperature during growth, and as the growth temperature rose, the magnetization lessened. A correlation between magnetization, morphology, and surface-to-volume ratio was also observed, with an increasing trend of magnetization as the surface-to-volume ratio increased. Other authors, including Mathur et al.,[82] Yang et al.,[83] Manna et al.,[84] Liu et al.,[85] and Zhang et al.,[86] demonstrated control over the morphology, size, and other properties of SnO_2 nanostructures could be achieved by adjusting the synthesis conditions such as temperature, deposition time, flow rates, and precursor selection. Barth et al.[87] employed a molecule-assisted and gold-catalysed CVD method to obtain aligned SnO_2 nanowires using a single-molecular source $[Sn-(OtBu)_4]$. The catalysing function of gold facilitated the advancement of SnO_2 on a single-crystal rutile substrate. The Sn^{4+}–O species released during
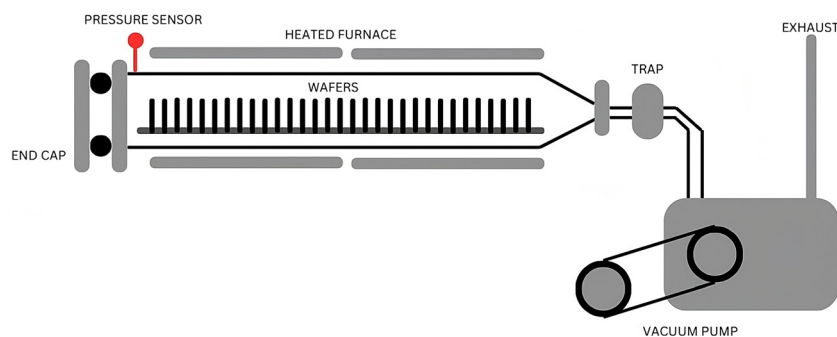

Fig. 3 Schematic illustrating the chemical vapour deposition process.

Table 4 Reaction conditions for the CVD method, reagents, and morphological characteristics

Morphology	Reaction temp. (°C)	Reaction time (h)	Basic reagents	Ref.
Thin film	850	0.3	Stannous 2-ethylhexanoate	86
Nanostructures	900	0.5	Metallic Sn	87
Nanowires	750	—	Tin(IV) tert-butoxide, tert-butyl alcohol, diethyl amine	88
Nanobelt	1000	1	Metallic Sn, tetrachloroauric acid	87

precursor decomposition were especially alloyed with gold nanoparticles or diffused to energetically favoured nucleation sites, leading to a heteroepitaxy of SnO_2 on TiO_2. Table 4 presents the reaction conditions employed in the CVD method and details of the reagents used.

2.1.4. Sonochemical method. Advanced techniques have revolutionized the synthesis of nanostructured materials, and sonochemistry is one such technique that stands out. Sonochemistry harnesses the power of ultrasound radiation to induce chemical reactions in molecules. By applying intense ultrasound radiation within the frequency range of 20 kHz to 10 MHz, sonochemistry offers a simple and effective approach for fabricating nanoscale materials with a uniform distribution of particle sizes. Sonochemistry utilizes ultrasonic signals as an energy source, creating a distinct environment for chemical reactions.[89] In the sonochemical process, the solution experiences high and low pressures due to high-energy ultrasonication. This pressure variation leads to the formation and subsequent collapse of acoustic cavitation bubbles, facilitating the synthesis of nanomaterials, such as SnO_2 nanocrystals. Notably, this synthesis method eliminates the need for external heating, as the ultrasonic waves generate the necessary conditions for SnO_2 nanocrystal formation.[90] The growth mechanism of sonochemically manufactured SnO_2 is strongly linked to the breakdown of these microscopic bubbles during cavitation. The simultaneous mechanical and chemical effects resulting from the collapsing bubbles under high temperatures and pressures create an oxidative environment that promotes the unvarying growth of SnO_2 nanocrystals. This unique approach allows exact control over the size and morphology of the synthesized nanomaterials, thus enabling the development of desirable properties for diverse applications.[63,91–94]

Using a mild ultrasonic method that was also rapid, facile, and efficient, Qurashi et al. successfully synthesized SnO_2 nanoparticles at lower temperatures. Their process offered a simple and effective means to prepare SnO_2 nanoparticles.[95] Goswami et al. documented the development of hollow SnO_2 nanostructures on cellulose acetate using a sonochemical spinning process. By subjecting an ethylene glycol solution of stannous chloride to microwave irradiation, then utilizing ultrasonication, they were able to create hollow SnO_2 nanotubes with a notable surface roughness and porosity.[96]

Gedanken et al. utilized this method to prepare spherical SnO_2 nanoparticles, employing a solution of $SnCl_4$ and azodicarbonamide in water. The nanoparticles formed a porous irregular network structure. They also showed an increased particle size with heating, exhibiting rounded hexagonal shapes after sintering at 800 °C.[97] Zhu et al. developed a method for fabricating SnO_2 nanotubular materials from cotton fibres. Ultrasonic treatment of the cotton fibres in $SnCl_2$ solution followed by calcination preserved the initial cotton morphology, resulting in nanotubular materials.[98] Kundu et al. compared the properties, such as microstructural and structural properties, of biosynthesized SnO_2 powder through a gel calcination method with those synthesized by sonochemical and sol–gel methods resulting in the formation of highly crystalline SnO_2 nanoparticles.[99] Table 5 outlines the conditions used in the sonochemical method.

2.1.5. Microwave synthesis method. The synthesis of nanomaterials using microwave irradiation has emerged as an up-and-coming and efficient method, offering numerous advantages over traditional synthesis techniques. This review paper aimed to explore the potential of microwave-assisted synthesis for producing SnO_2 nanoparticles, highlighting its benefits as an environmentally friendly synthesis method.

Microwave irradiation has gained significant attention due to its ability to expedite the synthesis process, allowing reactions to complete in just a few minutes. This rapid reaction time is a substantial advantage, as it not only saves time but also enhances the overall efficiency of the synthesis process. Microwave heating facilitates the avoidance of temperature and concentration gradients, thus ensuring a uniform environment for the nucleation of nanomaterials.[103] One of the crucial benefits of microwave synthesis is its ability to suppress side reactions, resulting in an improved yield and reproducibility of the desired product. By precisely controlling the reaction conditions, microwave-assisted synthesis minimizes undesired by-products and facilitates the production of high-quality SnO_2 nanoparticles. This characteristic makes microwave synthesis an essential consideration for developing greener synthesis methodologies. Moreover, microwave-assisted synthesis holds immense potential for advancing the field of nanotechnology by offering a more environmentally friendly approach for the

Table 5 Reaction conditions utilized in the sonochemical method and the reagents employed

Morphology	Reaction temp. (°C)	Reaction time (h)	Basic reagents	Ref.
Nanoparticles	80	2	Tin(IV) chloride, azodicarbonamide	100
Mesoporous nanoparticles	25	3	Tin ethoxide, cetyltrimethyl ammonium bromide, ammonium hydroxide	101
QD	80	2	Tin(IV) chloride, ammonium hydroxide	102

synthesis of nanoparticles. The utilization of microwave irradiation reduces the energy consumption required for synthesis, contributing to sustainable practices. With the increasing global demand for green and sustainable technologies, microwave synthesis is poised to play an important role in the future of synthetic nanotechnology.[63,104,105]

Kar et al. achieved the rapid synthesis of SnO_2 nanorods and nanoparticles using microwave irradiation, where the morphology could be meticulously controlled by changing the irradiation temperature and time. The use of microwave irradiation facilitated a uniform growth and homogeneous heating, producing small, refined, and discrete particles.[106] Yoshida et al. improved the microwave-assisted method for synthesizing shape- and size-controlled SnO_2 nanocrystals in ethanol–water solvents. Their approach significantly promoted uniform nucleation and shortened the synthesis time, leading to a narrow size distribution of SnO_2 particles.[107] Patra et al. prepared SnO_2 nanoparticles utilizing oleylamine and a capping agent. The choice of capping agents played a crucial role in tuning the crystal growth and morphology, and a texturing effect was observed, indicating preferred directional growth.[108] Aoyagi et al. synthesized single SnO_2 crystals with different shapes (columnar crystals and silver grass-like nanowhiskers) through the careful microwave heating of a TiO_2–SnO_2 blend. The shape of the crystals was found to be strongly influenced by the atmosphere during microwave irradiation, indicating a variation in growth mechanisms. Yao et al. synthesized organic-component-wrapped SnO_2 QDs using this method. As the irradiation time increased, the QDs formed short chains due to the "oriented attachment" mechanism, which could effectively reduce the interface energy.[109] Mathur et al. combined the benefits of microwave heating and a sole-origin molecular precursor for orchestrating the formation of SnO_2 nanocrystals. Uniform SnO_2 nanocrystals with good water dispersibility were achieved through the utilization of a tin alkoxide source within an ionic liquid medium in their strategy, possibly making them useful for conductive ink applications.[110] Ochs et al. documented the microwave-assisted production of nanocrystals of SnO_2 that exhibited varied shapes, a trait determined by the specific synthesis parameters. Utilizing the microwave technique enabled the precise creation of SnO_2 nanocrystals with customized configurations.[111] Table 6 outlines the reaction conditions applied in the microwave method, offering a comprehensive overview of the reagents utilized and the resulting morphological characteristics.

2.1.6. Atomic layer deposition (ALD) method. In addition to the abovementioned methods, ALD is another prevalent technique for depositing compact SnO_2 films. Derived from CVD, ALD has been widely applied in producing top-tier semiconductor films within the semiconductor industry. The ALD deposition process comprises distinct phases, starting with commencement, which entails the pulsed introduction of precursor A into a reaction chamber, which forges a monomolecular film on the substrate through chemical absorption. Subsequently, any unreacted precursor gets purged by an inert gas stream. Next, a different precursor, B, enters the chamber and reacts with the precursor A adhered to the substrate, forming a delicate product film. The residual precursor and reaction by-products are then expelled via the inert gas flow. This method is confined by the boundaries of chemical absorption, allowing each reaction cycle to precipitate a solitary molecular layer.[63,113,114] Consequently, it allows precise management of the entire procedure, ensuring an extensive scope of coverage for the generated film. Further, the ALD deposition technique involves significantly reduced energy levels, safeguarding the substrate from potential harm caused by energetic ions. This makes ALD a prevalent choice for producing ultrathin, top-notch SnO_2 films tailored for applications as ETL materials.[115–118]

Lu et al.[119] explored the microstructural aspects of epitaxial thin layers of SnO_2 grown on α-Al_2O_3 (012) substrates at a temperature of 600 °C. This could be accomplished using $SnCl_4$ or SnI_4 as the Sn source in an ALD set-up. The results revealed that the interface between the film and substrate maintained a flat profile, with no discernible supplementary phases. Table 7 showcases the thickness variation with varying the experimental conditions. However, the metal precursor's selection significantly impacted the film's internal structure and external surface characteristics. Intriguingly, films produced through the SnI_4-based process exhibited a consistent thickness, smooth surface, and minimal anti-phase boundaries (APBs), resembling the attributes of a flawless single crystal.

Contrastingly, a roughened surface, uneven thickness, and a high concentration of defects, including growth twins, stacking faults, APBs, and dislocations, were observed in films created via the $SnCl_4$ route. Valuable insights into the microstructure of epitaxial SnO_2 thin films on α-Al_2O_3 (0 1 2) substrates at 600 °C using different Sn precursors were provided by these findings, which have implications for various applications, such as gas sensors, transparent conductive electrodes, and solar cells. Understanding the influence of the metal precursors on the properties a film can aid in developing high-quality SnO_2 thin films for enhanced performance in diverse technologies. Choi et al.[120] presented a novel approach for synthesizing SnO_2 thin film using the $Sn(dmamp)_2$ precursor. This ALD process involved introducing $Sn(dmamp)_2$ into the reactor with a N_2 carrier gas flow, while O_3 gas was generated by mixing O_2 and

Table 6 Reaction conditions for the microwave synthesis method, reagents, and morphological characteristics

Morphology	Reaction temp. (°C)	Reaction time (h)	Basic reagents	Ref.
Nanoparticles	120	0.08	Tin(IV) acetate, oleic acid, oleylamine	106
Nanospheres	120	0.75	Tin(IV) chloride, 1-butyl-3-methylimidazolium tetrafluoroborate, sodium hydroxide	108
Nanocrystals	180	0.75	Tin chloride pentahydrate	107
QDs	180	0.01	1-Butyl-3-methylimidazolium tetrafluoroborate, tin(IV)tert-butoxide	112

Table 7 ALD process parameters and the resulting thickness of the deposited films acquired from TEM cross-sections

Precursor	T_{vap} (°C)	P_{tot} (Torr)	Oxygen source	No. of cycles	Thickness (nm)	Ref.
SnCl$_4$	0	1.8	H$_2$O$_2$	3000	93	119
SnCl$_4$	0	2.1	H$_2$O	3000	117	
SnI$_4$	84	1.9	H$_2$O$_2$	1000	41	
SnI$_4$	115	10	O$_2$	1000	117	

N$_2$. Purging between the precursor pulses was carried out with N$_2$, with a purging duration of 10 s and 5 s for Sn(dmamp)$_2$ and O$_3$, respectively. The film growth temperatures ranged from 100 °C to 230 °C. Additionally, certain films underwent rapid thermal annealing under a N$_2$ atmosphere at temperatures ranging from 400 °C to 500 °C for 1 min. The ALD process using Sn(dmamp)$_2$ and O$_3$ thus demonstrated promise for producing highly pure and robust SnO$_2$ films with low carbon and nitrogen contents, making them suitable for diverse applications. Further, the exceptional conformality of the ALD process on the hole structures with aspect ratios of approximately 9 indicate its potential use in microelectronics and nanotechnology.

Furthermore, light was shed on the growth behaviour of SnO$_2$ thin films at varying temperatures in the study, offering valuable insights for optimizing the growth conditions tailored to specific applications. Also, introducing a new Sn precursor expands the range of materials that can be grown *via* ALD, opening up new possibilities for further research and development in thin-film deposition. Sundqvist's team[121] used ALD in a process in which SnI$_4$ was evaporated from a quartz crucible at 115 °C and conveyed to the reaction zone through a nitrogen flow, with oxygen as the source of oxygen. Both computer-

controlled ALD and CVD processes were utilized, employing specific pulsing sequences. In the ALD process, pulse durations of 4 s for SnI$_4$, 6 s for the initial nitrogen purge, 4 s for the oxygen pulse, and 6 s for the subsequent nitrogen purge were employed in all the depositions. The simultaneous supply of SnI$_4$ and O$_2$ was carried out in the CVD process. Film depositions were conducted on α-Al$_2$O$_3$ (0 1 2) substrates that had been pre-cleaned in methanol at 75 °C using an ultrasonic bath for 5 min. The growth experiments were performed at temperatures ranging from 350 °C to 750 °C, under a total pressure of 1.3 kPa and a linear gas flow velocity of 0.5 m s^{-1} for both processes. Upon comparison of the SnO$_2$ thin-film growth using the ALD and CVD techniques with the same precursor combination (SnI$_4$ and O$_2$), it was observed that higher-quality films were achieved through the ALD process. The near-perfect single crystallinity, minimal density of defects, and nearly atomically smooth surfaces were demonstrated by these films. Table 8 provides a comprehensive overview of the precursors, synthesis conditions, growth particulars, and structural characteristics in ALD processes.

In contrast, the CVD process produced films with a considerably rougher morphology, featuring grain boundaries and the formation of twins. This suggests that the ALD method is more suitable for producing high-quality epitaxial films. These findings have important implications for the fabrication of SnO$_2$ films, offering valuable insights into the choice of deposition technique based on the desired film characteristics.

The selection of the reactants in the SnO$_2$ ALD process has a pivotal role in shaping the characteristics of the resultant films. Opting for metal–organic precursors confers notable benefits, including reduced synthesis temperatures, enhanced growth rates, and higher film purity. Among the inorganic precursors,

Table 8 Overview of the precursors, synthesis conditions, growth, and structural characteristics of ALD processes

Precursor	Oxygen source	Substrate	Temp. (°C)	Growth per cycle (Å)	Structure	Ref.
SnCl$_4$	H$_2$O	Si (100) glass	300	0.21	Amorphous	120
			350	0.38	Polycrystalline	
			400	0.58	Polycrystalline	
			450	0.52	Polycrystalline	
SnCl$_4$	H$_2$O	Al$_2$O$_3$-(012)	300	0.4	Polycrystalline	121
			600	0.3	Polycrystalline	
			700	—	Epitaxial	
SnI$_4$	O$_2$	Al$_2$O$_3$-(012)	400	1.0	—	121 and 122
			500	1.0	Low-grade	123
			600	1.1	Epitaxial	
			750	1.2	Epitaxial	
SnI$_4$	H$_2$O	Al$_2$O$_3$-(012)	100–200	0.65	Amorphous	
			200	0.65	Polycrystalline	
			300	0.25	Epitaxial	
			400	0.2	Epitaxial	
SnCl$_4$	H$_2$O	SiGaAs	180	0.04	Amorphous	124
			300	0.17	Polycrystalline	
SnI$_4$	O$_2$	Si/SiO$_2$ (100)	400	0.4	Polycrystalline	125
			600	1.5	—	
			750	2.4	—	
TDMASn	H$_2$O$_2$	Glass Si (100)	—	1.2	Amorphous	126
DBTA	O$_2$	(110) (a-cut) (100) (m-cut) sapphire	300	1.1	Epitaxial/stoichiometric	127
Sn(acac)$_2$	O$_3$	Si (100)	175–300	1	—	128
			200	—	Amorphous	
			200–300	—	—	

Table 9 Comparison of different device structures with their respective solar cell parameters

Device structure	V_{oc} [V]	J_{sc} [mA cm^{-2}]	FF [%]	PCE [%]	Ref.
FTO/SnO$_2$/perovskite/spiro-MeOTAD/gold	1.14	21.3	0.74	18.4	129
Glass/FTO/PEALD-SnO$_2$/C$_{60}$SAM/perovskite/HSL/Au	1.07	21.4	0.73	17.4	130
Glass/FTO/PEALD-SnO$_2$/C$_{60}$-SAM/perovskite/spiroOMeTAD/Au	1.13	22.69	0.76	20.41	131
Flexible ITO/SnO$_2$/perovskite/spiro/Au	1.101	22.11	75.42	18.36	132

SnI$_4$ holds significant promise in generating films with an even thickness, smooth surfaces, and minimal defect concentrations. To attain polycrystalline films, it is necessary to either elevate the synthesis temperature beyond 250–300 °C or introduce an additional annealing phase. Commonly employed substrates include TiO$_2$ single crystals, sapphire, and YSZ. Table 9 presents a comparative analysis of various device structures, with their corresponding solar cell parameters listed to comprehensively understand their performance.

The choice of oxidants is also vital. The TDMASn/H$_2$O$_2$ combination typically yields a reasonably high growth rate. Film deposition at temperatures below 100 °C is facilitated by using H$_2$O, benefiting the production of thermally sensitive materials, such as photovoltaic cells and organic light-emitting diodes. The films exhibit the highest conductivity when O$_3$ is utilized as the oxidant, a critical factor for their application in transparent conducting oxides (TCOs).

2.1.7. Radiofrequency (RF) sputtering method. RF sputtering is a widely utilized technique for vapour-based PSC fabrication. Employed within a vacuum coating framework, this technology is particularly suited to the deposition of TCO thin films, such as SnO$_2$, TiO$_2$, ZnO, indium-doped tin oxide (ITO), and fluorine-doped tin oxide (FTO).[133–136] This method operates at elevated frequencies and voltages, inducing the creation of high-energy ion streams from the gas used. An inert gas (*i.e.* argon) is typically introduced into a vacuum chamber. The resulting ionized gas particles then pummel a designated target, causing sputtering and a subsequent deposition of target materials onto a substrate.

The resultant film, comprising the material from the target, takes form upon the substrate's surface. The properties of the film produced are collectively shaped by certain key parameters, such as the RF power, working gas pressure, sputtering duration (equivalent to film thickness), the proportion of different working gases, bias voltage, target composition, and purity, as depicted in Fig. 4. It has been proven that RF sputtering is a reliable and efficient method for depositing SnO$_2$ films.[119,137–139] Table 10 summarises the typical conditions used during RF sputtering.

Herein, we discuss the reported studies that have been done using RF sputtering, the parameters utilized, and the results and study achievements. Zhu *et al.* reported using RF magnetron sputtering for a SnF$_2$–Sn target in an Ar–O$_2$ atmosphere, whereby FTO films could be successfully obtained at higher O$_2$ fluxes and increasing substrate temperatures. The FTO films exhibited improved crystallinity and a preferred orientation with a higher substrate temperature and O$_2$ flux.[140] In another study, the films were found to be amorphous, highly transparent, and exhibited thermoelectric properties. Further, a subsequent annealing at 400 °C in air resulted in crystallization. Notably, the annealed films achieved transmittance above 95% and a high figure of merit (PF) of 1×10^{-4} W m^{-1} K^{-2} at room temperature.[142]

Abdul Faheem Khan *et al.* found that annealing led to precipitation of the SnO phase within the tetragonal SnO$_2$ matrix. The particle size of the films remained around 20–30 nm after deposition and annealing. The band gap energy decreased from 3.55 eV to 3.50 eV at 500 °C annealing
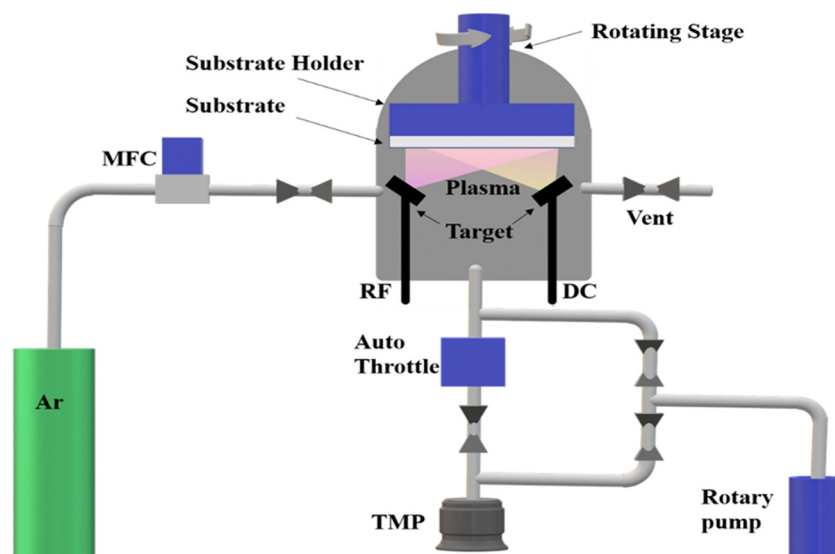

Fig. 4 Schematic representation of the components involved in RF sputtering.

Table 10 Experimental conditions used during film deposition by RF sputtering

Target	Substrate	Vacuum pressure (mbar)	Gas mixture	Annealing conditions (°C)	Power supply (W)	Substrate–target distance (cm)	Ref.
Sn and SnF$_2$	Soda-lime-silica glass	3.5×10^{-5}	O$_2$ and Ar	100	75	—	140
Sn	—	3–4×10^{-3}	O$_2$ and Ar	300, 400, 500	15	10	141
SnO$_2$	Corning glass	0–5	Ar + O$_2$ (15% O$_2$)	100–500	~ 35	5	142
Sn	Glass slides, p-Si, ITO	4×10^{-6}	O$_2$ and Ar	200, 400	50	—	142
Sn	—	—	O$_2$, Ar/O$_2$ mixtures	500	25	—	143
Sn	Quartz	10^{-6}	Ar and O$_2$	—	30	5	144
Sn	Corning glass	3–4×10^{-3}	Ar and O$_2$	300, 400, 500	15	10	145
Ceramic SnO$_2$	—	2.6×10^{-2}	98% Ar + 2% O$_2$	200, 400, 550	100	—	146
Sn	Glass and Si wafers	3×10^{-6}	Ar/O$_2$ mixture	—	400	10	147
Ceramic SnO$_2$	—	2×10^{-6}	98% Ar + 2% O$_2$	200, 400, 550	100	—	148
SnO$_2$	Alumina plates	4×10^{-7}	O$_2$ + Ar	320–370	800	8	149

temperature. In comparison, the SnO$_2$ films demonstrated a high optical conductivity up to 10^{14} s^{-1}.[143] UV-Vis-NIR spectroscopic analysis revealed a high optical transparency $> 90\%$ at 600 nm wavelength and an optical band gap ranging from 3.4 to 3.8 eV. The n-type conductivity of the samples was investigated by Hall measurements, revealing enhanced carrier concentration and mobility. It was suggested by the results that SnO$_2$ deposited at a substrate temperature of 200 °C holds promise as an efficient ETL for PSCs.[144] Also, whether the O$_2$/Ar ratio plays a significant role in the film thickness was investigated, and it was found that the thickness increased with the higher Ar content. Conversely, the band gap increased with decreasing the Ar content. The refractive index exhibited an oscillatory behaviour, and annealing resulted in a decrease in the band gap. The experimental data suggested the involvement of oxygen vacancies and interstitials in the observed phenomena.[145] The effect of the substrate temperature and oxygen flow rate on SnO$_2$ thin films was tested for gas sensor applications. It was found that thermal treatment before sensor use stabilized the film's microstructure.[146] M. Ruske *et al.* concluded that his approach could improve the process stability and result in modified layer properties, including higher densities and hardness, than from DC sputtering. The morphology of the layers exhibited a similar dependency on the sputtering pressure, but high pressure led to different crystal orientations. Additionally, the MF samples had higher internal stress, which could be mitigated by increasing the sputtering pressure.[150] Annealing was also investigated, and it was found that this led to an augmentation in the particle dimensions, expanding them from 165 nm to 280 nm. Concurrently, the direct optical energy gap experienced a marginal reduction, shifting from 4.21 eV to 4.14 eV. Moreover, alterations in the annealing temperature had a discernible impact on the third-order nonlinear susceptibility, as well as on the values of the free carrier concentration and plasma frequency.[148]

A relationship between the electronic properties of SnO$_x$ films and the sputtering deposition power was reported, which stated that a slight increase in power of less than 2% causes a significant shift in carrier transport from an n-type to p-type behaviour. The optimal performance could be achieved at a sputtering power below the critical value of 120 W, with the highest on/off ratio and a subthreshold swing. However, a slight increase beyond the critical power drastically decreased the on/off ratio. These findings highlight the critical role of the sputtering power in determining the stoichiometry of the SnO$_x$ film.[149] M. Di Giulio *et al.* employed reactive sputtering techniques on SnO$_2$ targets and activators like Pt. In comparison, pure SnO$_2$ films could only sense CO at around 300 °C, delivering a peak sensitivity of 120% at a concentration of 500 ppm. However, the performance was markedly elevated in the case of Pt–SnO samples. These samples could detect CO at a mere 170 °C, showcasing a significantly heightened maximum sensitivity of approximately 400% at the same concentration level.[148] Further, the optimized annealing condition of 500 °C for 1 h resulted in films with a high hole concentration of 1.14×10^{18} cm^{-3} and low resistivity of 1.38 Ω cm. Additionally, the films exhibited excellent optical transmission, exceeding 80%.[151]

2.2. Structural configuration of SnO$_2$

A diverse range of characteristics are displayed by the various phases of SnO$_2$ crystal structures, wherein distinct physical and chemical characteristics are presented by each phase. Understanding and controlling these phase transitions are crucial for tailoring SnO$_2$ for diverse applications, including photovoltaics, battery technologies, gas sensing, and beyond. Incorporating dopants and manipulating the deposition conditions are effective strategies to stabilize and engineer specific phases of SnO$_2$. Nonetheless, challenges persist in achieving pure single-phase cubic or orthorhombic SnO$_2$ at atmospheric pressure, highlighting the need for continued research and innovation in materials science and thin-film deposition techniques.

SnO$_2$ is a fascinating material with diverse crystal structures that can be stabilized and transformed through numerous growth techniques and dopants. The most prevalent polymorph of SnO$_2$ is the tetragonal rutile structure (*P*4$_2$/*mnm*), which serves here as the starting point for understanding the phase transitions and potential applications of SnO$_2$.

SnO$_2$ transforms to its polymorphs under pressure, as shown in Fig. 5. One notable phase transition in SnO$_2$ is from the tetragonal rutile structure (Fig. 5(a)) to the orthorhombic *Pnnm* phase. This transformation typically occurs under high-pressure conditions, around 12 GPa.[152] The metastable version of the orthorhombic phase can also be present, such as the α-PbO$_2$-type orthorhombic or scrutinyite structure (Fig. 5(b)),

Fig. 5 Bulk formations of SnO$_2$ polymorphs, with blue and red representing Sn and O atoms, respectively. (a) Rutile in the *P42/mnm* and CaCl$_2$-type in the *Pnnm* space groups, (b) R-PbO$_2$-type in the *Pbcn* space group, (c) pyrite-type in the *Pa3h* space group, (d) ZrO$_2$-type in the *Pbca* space group, (e) fluorite-type in the *Fm3hm* space group, and (f) cotunnite-type in the *Pnam* space group.

depending on the specific conditions and oxygen content. The scrutinyite phase, which exhibits exciting physical properties, like improved gas sensing, is an under stoichiometric phase with oxygen vacancies formed by incorporating dopants. For example, introducing dopants like Co and Mn demonstrated the capability to stabilize the scrutinyite phase. This was achieved by replacing Sn within the structure, creating oxygen vacancies.[152,153] Continuing the pressure-induced phase transitions, at approximately 17 GPa, the scrutinyite phase transforms into the pyrite-type cubic (*Pa3*) phase (Fig. 5(c)).[154] This cubic phase can be further stabilized at higher pressures, even up to 48 GPa. Around 28 GPa, a ZrO$_2$-type I orthorhombic phase, as shown in Fig. 5(d), becomes stable through a transformation from the pyrite structure (with the *Pbca* space group). At the same time, the unit cell volume experiences a 2% expansion.[33,155,156] Theoretical predictions have proposed that a change in phase from the cubic *Pa3* phase to the cubic fluorite-type (*Fm3m*) phase, as shown in Fig. 5(e), would occur at a reduced pressure of 24 GPa. The key differences between the cubic pyrite and fluorite phases primarily stem from their oxygen arrangement. In the pyrite phase, Sn atoms are coordinated with six oxygen atoms and two more atoms positioned at a greater distance. In contrast, the fluorite phase involves eight oxygen atoms evenly spaced around the Sn. When the pressure is eased, these cubic phases undergo inverse phase changes,[155] converting back to orthorhombic and then to tetragonal structures. Furthermore, when subjected to a pressure of 33 GPa, a new crystal structure emerges, as shown in Fig. 5(f), characterized by the orthorhombic phase II in the cotunnite-like configuration. This phase belongs to the *Pnam* space group; in which within it, the Sn cations are bonded to nine oxygen anions.[33,155,156]

Stabilizing the orthorhombic phase as thin films can be achieved through precise control of the deposition conditions, such as temperature and pressure. Various deposition techniques, including sputtering, pulsed laser deposition (PLD), plasma-enhanced atomic layer deposition (PE-ALD), and mist CVD, have been reported in the literature. Additionally, dopants can play a

crucial role in stabilizing specific SnO$_2$ phases. Transition-metal or rare-earth ions can be introduced as dopants, substituting Sn in the lattice. Significantly, dopants exhibiting atomic radii similar to or smaller than Sn^{4+} cations, such as Mn^{3+}, Mn^{4+}, Zn^{2+}, and Co^{2+}, have exhibited encouraging outcomes in stabilizing the orthorhombic phase. Conversely, ions with larger atomic radii, such as Ce^{4+} and Ce^{3+}, can stabilize the orthorhombic phase by inducing lattice disorder and structural defects. For example, a solid solution of Sn$_{0.7}$Ce$_{0.3}$O$_2$, despite the significant differences in ionic radii, demonstrated a stabilized orthorhombic phase with a molar content of 41%.[157–162]

Challenges remain in synthesizing pure single-phase cubic or orthorhombic SnO$_2$ at standard pressure, as they often occur as a mixture of phases. Many research investigations have aimed to stabilize metastable phases using methods involving thin-film deposition, but achieving single-phase cubic or orthorhombic SnO$_2$ at atmospheric pressure requires further exploration and development.[163,164]

2.3. Optical properties of SnO$_2$

SnO$_2$ stands out for its exceptional superior light transmittance, favourable bandgap properties, and exceptional electron mobility, making it an auspicious material for various optoelectronic applications. Its utilization as a transparent electrode material holds exciting possibilities for advancements in light management and energy-conversion technologies. Its wide bandgap and low reflective index enable it to exhibit outstanding light transmittance, achieving a remarkable 90% transmittance in glass.[165] This surpasses the transmittance of TiO$_2$ films and FTO glass. Furthermore, SnO$_2$'s efficient management of light in the UV-visible region allows photons to penetrate and be absorbed by the perovskite absorber, promoting efficient energy conversion.[166]

One of SnO$_2$'s key advantages is its reduced absorption of UV light compared to TiO$_2$, which results in enhanced device stability. Moreover, SnO$_2$ demonstrates exceptional electron mobility, surpassing TiO$_2$ by a factor of 100. Also, SnO$_2$

possesses a deep CB compared to TiO$_2$, making it highly promising for various optoelectronic applications, including solar cells and photodetectors. SnO$_2$ QDs have been recently introduced in thin films. These QD films have achieved remarkable transmittances exceeding 95% in the visible region,[167,168] further enhancing SnO$_2$'s appeal as a material for transparent conductive oxides. Such characteristics make SnO$_2$ a desirable candidate for transparent electrode materials, offering significant potential for enhancing the efficiency and performance of optoelectronic devices.[21] Fig. 6(a) shows a comparison between a 60 nm thick SnO$_2$ nanocrystalline film-coated FTO substrate and a compact TiO$_2$ film of similar thickness on the same batch of FTO substrates. Better light transmittance and a wider bandgap were demonstrated by the SnO$_2$ film compared to the TiO$_2$ film, indicating a potential route to achieving an enhanced J_{sc} and, consequently, a higher PCE for lead halide PSCs.[169] In Fig. 6(b), the transmission spectra of different SnO$_2$ films (200-SnO$_2$, 500-SnO$_2$, Mg–SnO$_2$, and mp-SnO$_2$) coated on quartz glass substrates are presented. This approach was taken to overcome the challenge of accurately extracting bandgaps from films coated on FTO substrates, where the shielding effect of the FTO substrate would interferes with the absorption edge measurements. While the transmission of mp-SnO$_2$ showed a slight decrease, its structure substantially enhanced the absorption capabilities of the perovskite layer.[168]

These findings indicate the potential of SnO$_2$ films, particularly the nanocrystalline variants, for enhancing light transmittance and promoting efficient light absorption in PSCs. The superior optical properties of SnO$_2$ make it a promising material for optoelectronic applications, and its integration in solar cells could lead to further advancements in solar energy-conversion technologies.

2.4. Electronic properties

The electronic properties of SnO$_2$ make it stand out as a highly versatile material for optoelectronic applications. The bulk form of SnO$_2$ possesses a bandgap energy of approximately 3.6 eV, as determined by theoretical calculations. However, experimental measurements have revealed that the actual bandgap of SnO$_2$ can vary between 1.7 and 4 eV, indicating

its versatility and potential for applications in fields such as photovoltaics and photocatalysis. This wide range of bandgap values opens up new possibilities for tailoring SnO$_2$'s properties to specific optoelectronic requirements.[170–172] As a member of the TCO family, SnO$_2$ possesses a unique dual ability to conduct electricity while transmitting visible light. Such optical transparency and electrical conductivity are essential for various optoelectronic devices, including solar cells and displays. Researchers have devoted significant efforts to bandgap engineering in SnO$_2$, driven by its promise in technological applications. These efforts involve exploring diverse parameters, such as synthesis methods and substrate-induced strain during thin-film growth, to control and manipulate SnO$_2$'s bandgap characteristics precisely.

First-principles calculations have provided valuable insights into the relationship between the bandgap of SnO$_2$ and the distortion of its crystal structure. As shown in Fig. 7, bandgap narrowing can occur in SnO$_2$ under tensile strain due to disorder in the SnO$_6$ octahedra through increasing distortion within the SnO$_6$ octahedra, leading to variations in the bond lengths and angles within the unit cell, and resulting in a reduction of the bandgap energy. This understanding allows for fine-tuning the bandgap properties of SnO$_2$ to meet specific device requirements.[173] A molecular-orbital bonding diagram is provided in Fig. 8 to visually represent the electronic interactions within SnO$_2$.

Hybridization of the B$_{2g}$, A$_{1g}$, and E$_g$ orbitals with $\pi 2p_y$ and $\sigma 2p_z$ orbitals among the Sn and O atoms in SnO$_2$ contributes to its electronic structure. Density of states (DOS) can also graphically depict the energy states that electrons occupy in the valence and CBs of SnO$_2$. The CB is primarily influenced by the hybridization of Sn-4d and O-2p orbitals, while the valence band (VB) encompasses contributions from various orbitals, including O-2s, Sn-5s, O-2p, Sn-5p, Sn-4f, Sn-3d, and additional O-2p orbitals.[174,175] The presence of defects, such as vacancies in the oxygen or Sn positions within the SnO$_2$ structure, significantly impacts the bonding characteristics and induces distortions in the unit cell.

As a result, these defects change SnO$_2$'s bandgap, leading to a reduced value of around 3.5 eV.[176] Understanding and
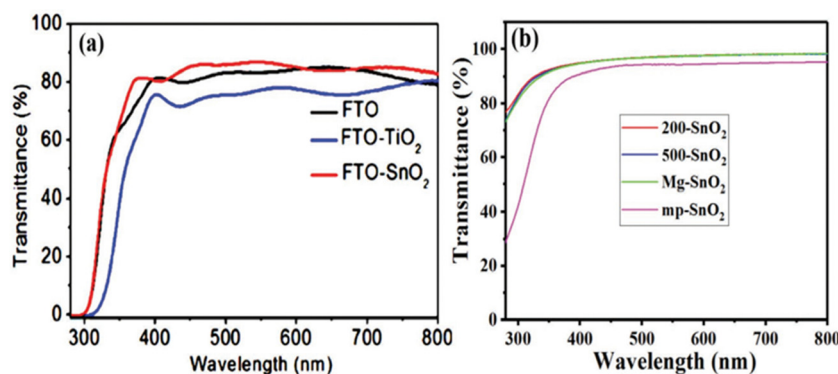

Fig. 6   (a) Transmission spectra of SnO$_2$ films coated on FTO substrates. Reproduced with permission.[167] Copyright 2015, American Chemical Society. (b) Transmission spectra of SnO$_2$ films coated on a silica glass substrate. Reproduced with permission.[168] Copyright 2018, John Wiley and Sons.
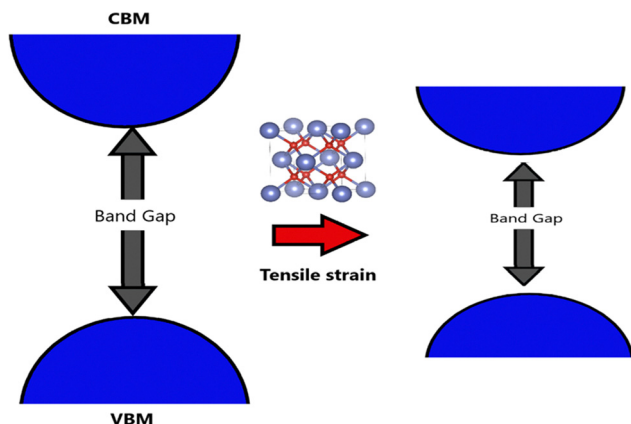
Fig. 7 Bandgap narrowing in SnO_2 under tensile strain due to disorder in SnO_6 octahedra.

controlling the influence of defects is crucial for optimizing SnO_2's electronic properties for specific device applications. SnO_2 exhibits both direct and indirect bandgap transitions.[177,178] Indirect bandgaps are observed at energy levels of 2.62 and 2.90 eV, which include variations in the electronic states within the material.[179] Moreover, the fundamental bandgap energy of SnO_2 has been predicted to be lower at around 3 eV.[180] However, specific optical transitions, known as dipole-forbidden band-to-band transitions, result in an optical bandgap of 3.8 eV.[181] These diverse bandgap characteristics offer diverse optical and electronic properties that can be harnessed for various applications.

An analysis of the electronic structure of pure SnO_2 was performed by Slassi *et al.* through DOS and projected DOS, as depicted in Fig. 9; where the impact of the exchange–correlation terms on the distribution of eigenstates was assessed utilizing the (a) GGA-PBE and (b) TB-mBJ approximations. Notably, strikingly similar distributions of the eigenstates were exhibited by the results from both approximations. It was revealed by the DOS that the upper section of the VB extended

from −7.8 to 0 eV in the PBE calculation and from −7 to 0 eV in the TB-mBJ calculation, while demonstrating a pronounced O-2p character, with minor contributions from an admixture of 4p and d-Sn states. Furthermore, the lower segment of the CB was predominantly characterized by the 4s-Sn orbital at the *G*-point.[182]

2.5. Recent progress of SnO_2 as an ETL

Previously, attempts have been made to utilize SnO_2 in third-generation solar cells. However, these devices still fall short when compared to using ZnO and TiO_2. In 2015, several groups individualistically incorporated SnO_2 in PSCs. For example, Dai and colleagues employed mesoporous SnO_2 films as an ETL and achieved an efficiency of 10.18% by combining them with $TiCl_4$ treatment.[183] Kuang and colleagues employed a nano colloidal film of SnO_2 treated with $TiCl_4$ as the ETL. A PSC achieved an efficiency of 14.69% due to this development. Addressing the challenges posed by high-temperature processing, a SnO_2 layer was developed that could be processed at lower temperatures.[17] The process utilized by Tian's team included applying spin-coated SnO_2 nanoparticles on substrates, and then carrying out a subsequent annealing step at 200 °C. As a result of this approach, a PCE of 13% was achieved.[184] Notably, Fang and colleagues reported a significant advancement in SnO_2-based PSCs by employing decomposition of a $SnCl_2 \cdot 2H_2O$ precursor through thermal treatment at 180 °C under normal atmospheric conditions, resulting in a reverse scan efficiency of 17.21% on an FTO substrate.[185] Moreover, a low-temperature ALD method was utilized by Hagfeldt and colleagues for the production of SnO_2 ETL, resulting in a PCE of approximately 18%, with a V_{oc} exceeding 1.19 V. Despite these results, the performance of these devices continues to lag behind their TiO_2 counterparts.[186] You *et al.* achieved a remarkable PCE of 21.6% in photovoltaic cells based on SnO_2. This accomplishment was made possible by their control of the surface passivation layer on PbI_2. Additionally,
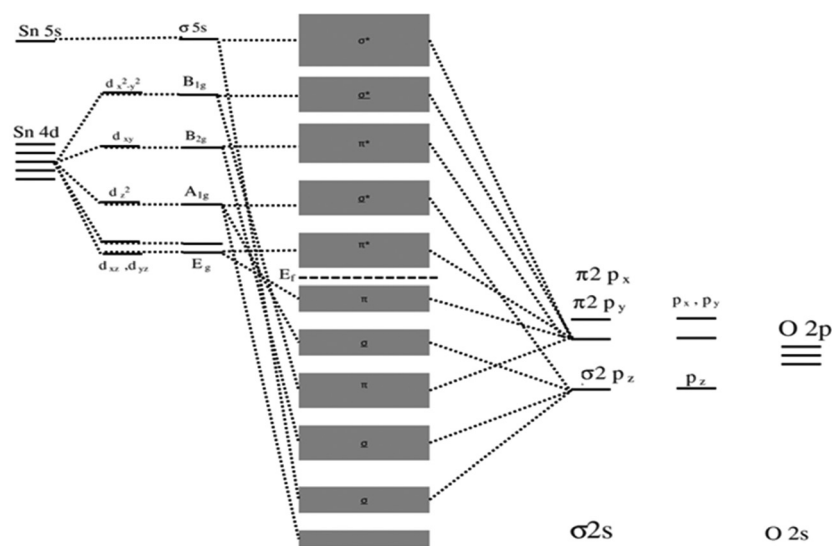

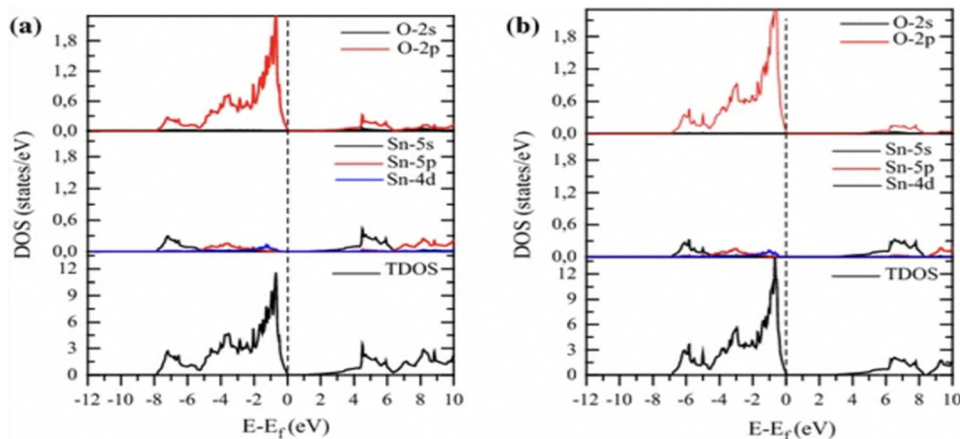**Fig. 8** Molecular–orbital bonding structure for tetragonal SnO_2.

Fig. 9 Pure SnO_2's partial and total densities of states calculated using (a) GGA–PBE and (b) Tb-mBJ. Reproduced with permission.[182] Copyright 2017, Wiley.

they achieved an impressive efficiency rate of 20.9%.[187] Zhu et al. introduced a novel approach using a SnO_2–KCl composite ETL in planar PSCs. This strategy could simultaneously address defects at the ETL/perovskite interface and grain boundaries. By incorporating K and Cl ions, the ETL/perovskite contact could be effectively passivated, leading to an enhanced V_{oc} from 1.077 V to 1.137 V and increased PCE from 20.2% to 22.2%.[188] Zhang's team, focused on reducing electron-transport losses within the ETL of metal oxide-based solar cells, introduced a novel ETL composed of amorphous F-doped TiO_x (F-TiO_x) and crystalline SnO_2. Here, the F-TiO_x was an intermediary between adjacent SnO_2 nanocrystalline molecules, with enhanced electron-transport pathways, reduced charge losses, and enhanced energy-level alignment. This modification led to a remarkable PCE of 22.70% in PSCs together with improved stability.[189] Li's team developed a water-soluble polyelectrolyte combining ethanolamine (EA) and poly-acrylic acid (PAA). They used this to stabilize SnO_2 nanoparticles, creating a 3D network. This hybrid material was then integrated

into the SnO_2 ETL, and helped prevent nanoparticle clumping and enabled a uniform film formation. The PAA–EA-modified SnO_2 also improved the perovskite film quality, enhancing carrier transport. As a result, PSCs achieved outstanding PCEs of 24.34% and 22.88% in different areas.[190] These advancements are illustrated in Fig. 10, showcasing the progress in PSCs utilizing SnO_2 as an ETL in the discussed studies.

A novel method for preparing a mesoporous SnO_2 ETL was presented by Sami Ullah and colleagues, involving the anodization of a metallic Sn film on an FTO substrate in a sodium hydroxide solution. A bilayer architecture was employed consisting of two consecutive layers of mesoporous SnO_2, with the morphology of each layer controlled by adjusting the anodiza-tion voltage and time. This approach allowed for better coverage of the FTO substrate compared to a single-layer configuration. The photovoltaic device incorporating the bilayer mesoporous SnO_2 ETL exhibited a notable 27% improvement in PCE. A comparison of the second layer evaporation, as shown in the FESEM image, and improvement in the PCE are shown in Fig. 11 below.[191]

Zhengjie Xu, Yue Jiang, and their research team studied the rapid synthesis of SnO_2 QDs using a microwave-assisted method for PSCs. The small-sized SnO_2-QDs exhibited remarkable elec-tronic properties compared to crystallized SnO_2 films, including improvements in the Fermi level, conductivity, electron mobility, and trap density. Additionally, the performance of PSCs based on the $CH_3NH_3PbI_3$ perovskite material was significantly enhanced, achieving a PCE of 20.24% with a higher V_{oc} com-pared to the PCE of 19.77% without SnO_2-QDs. Fig. 12 illustrates a cross-sectional FESEM image of the tested device and an image showing the SnO_2-QD deposition on an FTO substrate. Scale bars of 200 nm are included for reference. Additionally, as previously mentioned, TEM images and details on the device's performance are provided. These findings highlight the great potential of the microwave-assisted synthesis of SnO_2-QDs for the efficient, reproducible, and large-scale production of SnO_2-QDs.[192]

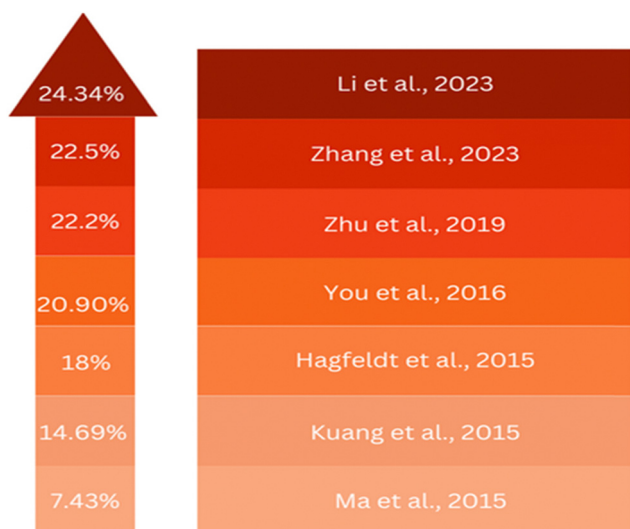Muhammad Salman Kiani researched the synthesis of SnO_2 QDs to be used as an ETL in flexible PSCs. QDs of 2.4 nm

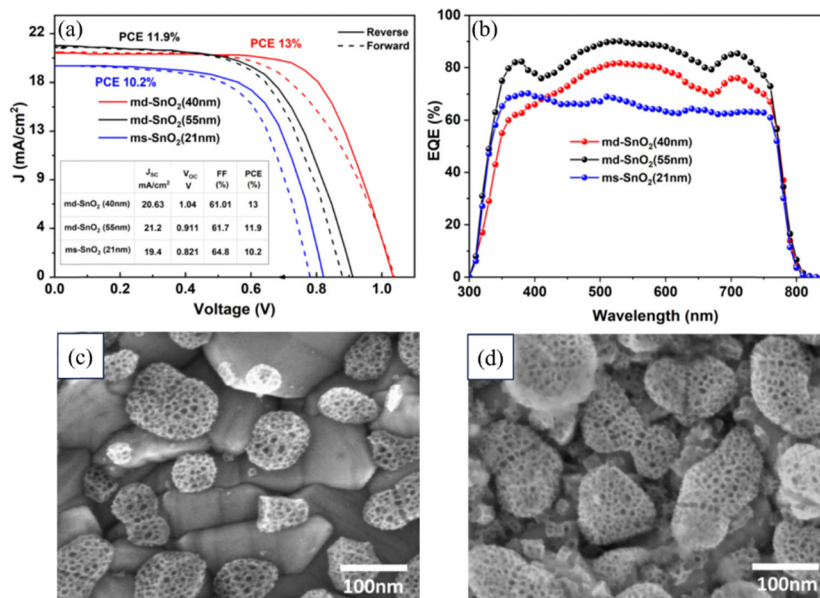**Fig. 10** Advancement in SnO_2 as an ETL layer in recent years.

Fig. 11 (a) Typical J–V curves of PSCs with md-SnO$_2$ (40 and 55 nm) and ms-SnO2 (21 nm) ETLs. (b) External quantum efficiency spectra of PSCs with md-SnO$_2$ (40 and 55 nm) and ms-SnO$_2$ (21 nm) ETLs. (c) FESEM image of the ms-SnO$_2$ layer grown on the FTO substrate showing the anodized evaporated Sn film. (d) FESEM image of the second Sn layer evaporated on anodized ms-SnO$_2$ in md-SnO$_2$. Reproduced with permission.[191] Copyright 2022, American Chemical Society.

diameter were produced through a solvothermal synthesis, and exhibited excellent crystallinity and dispersion. Functional layers were applied using a slot-die coating method, and water-based inks with varying QD concentrations were tested. The optimal performance was achieved with 2 wt% SnO$_2$ QD ink, resulting in an average PCE of 7.23% and a peak PCE of around 10%.[193] The provided information illustrates a comprehensive analysis of an as-fabricated SnO$_2$ QD-based device, as depicted in Fig. 13. The figure includes the J–V curves, a cross-

sectional view of the SnO$_2$ layer captured through FESEM, a micrograph showing the TEM images of the SnO$_2$ QD, and a schematic detailing the fabrication process of the device.

In another study, a novel approach was developed to enhance the electronic-transfer properties of SnO$_2$ layers in PSCs. A small amount of TiAcAc (titanium acetylacetonate) molecules was introduced into a SnO$_2$ nanoparticle solution. The incorporation of TiAcAc served multiple functions: stabilizing the dispersion of SnO$_2$ nanoparticles, enabling the formation of smooth ETL thin
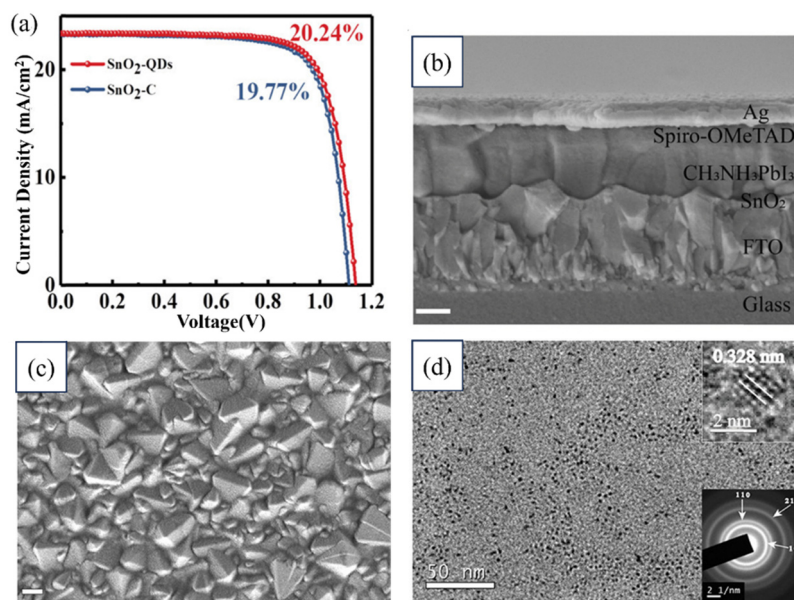

Fig. 12 (a) J–V characteristic curves from forward and reverse scans. (b) FESEM image of the cross-section of a tested device. (c) SEM image of SnO$_2$ coated on an FTO substrate. (d) TEM image of SnO$_2$. Reproduced with permission.[192] Copyright 2022, American Chemical Society.

Fig. 13 (a) $J–V$ curves of a device based on SnO_2 QDs. (b) FESEM image showing the cross-section of the SnO_2 layer. (c) TEM image of the SnO_2 QD. (d) Schematic of the device fabrication process. Reproduced with permission.[193] Copyright 2022, MDPI.

films, tuning the electronic band structure to match the upper perovskite layer, and improving the interface properties between the ETL and the perovskite layer. By varying the doping concentration, the thin-film morphology, surface energy, and optoelectronic properties of the SnO_2 ETL could be finely adjusted. This innovative approach could significantly improve the efficiency and reduce hysteresis in PSCs, comparable to state-of-the-art SnO_2-based PSCs. The findings of this research offer a promising

and efficient method for controlling SnO_2 growth, which could ultimately lead to highly efficient PSCs. Fig. 14 illustrates the typical $J–V$ curves for a device utilizing SnO_2–TiAcAc. It highlights the expected influence of depositing perovskite on thin films composed of TiAcAc-doped SnO_2 nanoparticles. Additionally, FESEM images are provided showing the SnO_2 layer deposited on FTO and the SnO_2–TiAcAc layer deposited on FTO.[194]

Fig. 14 (a) Typical $J–V$ curves of a device based on SnO_2–TiAcAc. (b) Anticipated impact of depositing perovskite on thin films of TiAcAc-doped SnO_2 nanoparticles. FESEM images of (c) SnO_2 layer deposited on FTO and (d) SnO_2–TiAcAc deposited on FTO. Reproduced with permission.[194] Copyright 2021, Wiley.
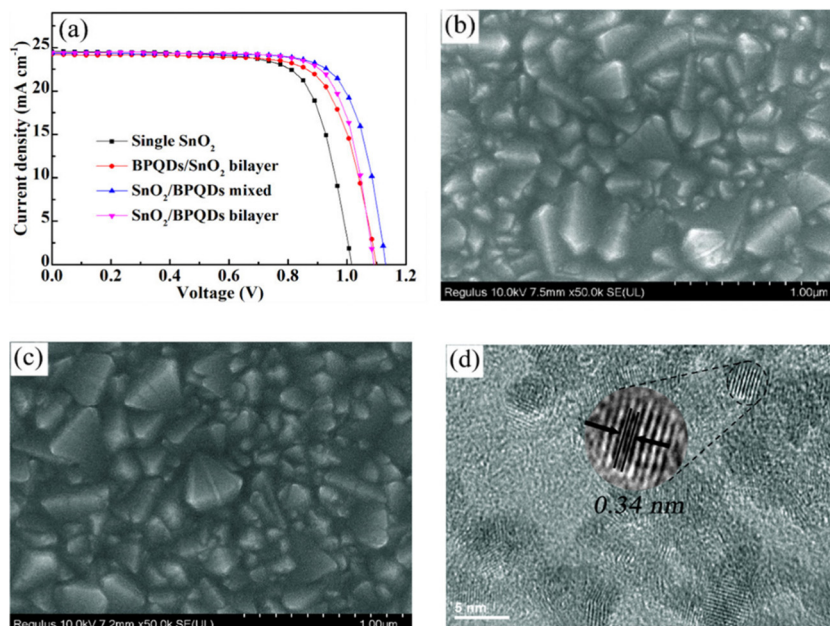
Fig. 15   (a) J–V curves of single SnO$_2$, BPQDs/SnO$_2$ bilayer, SnO$_2$/BPQDs mixed, and SnO$_2$/BPQDs bilayer ETL-based PSCs, FESEM images of (b) single SnO$_2$, (c) SnO$_2$/BPQDs mixed sample. (d) TEM image. Reproduced with permission.[154] Copyright 2022, American Chemical Society.

Gu and Bangkai's team enhanced the performance of SnO$_2$ ETL-based PSCs using bipyramidal quantum dots (BPQDs). The SnO$_2$/BPQDs mixture achieved a remarkable 21% efficiency, with sustained stability (over 90% efficiency after 1000 h of AM 1.5G lamp exposure) and minimal hysteresis. Fig. 15 displays the performance, specifically the J–V curves, employing different ETL configurations, namely in single SnO$_2$, BPQDs/SnO$_2$ bilayer, SnO$_2$/BPQDs mixed, and SnO$_2$/BPQDs bilayer ETL-based PSCs.

Additionally, the figure includes FESEM images illustrating the morphology of a single SnO$_2$, SnO$_2$/BPQDs mixed sample, and a TEM image providing a closer look.[154]

Babak Taheri's team demonstrated a scalable manufacturing process for large-area PSCs that is compatible with various surfaces for industrial applications. They introduced the concept of automated spray-coating (ASC) (at low temperatures) and utilized Np-SnO$_2$ as an effective strategy for creating

Fig. 16   (a) PCEs of complete solar devices based on SnO$_2$ spray-coating at different temperatures along with that of a spin-coated device. (b) Schematic representation of SnO$_2$ deposition with the spray setting parameters, (c) top-view SEM images of spin-coated and spray-coated samples, and (d) surface roughness analysis of spin-coated and spray-coated samples. Reproduced with permission.[195] Copyright 2020, Wiley.

expansive PSCs and modules. Fig. 16 presents the PCEs of all the solar devices fabricated using SnO_2, which were spray-coated at various temperatures, alongside that of a spin-coated device. The figure also includes a schematic depiction of the SnO_2 deposition process, highlighting the spray setting parameters. Additionally, top-view SEM images of both spin-coated and spray-coated samples are provided, along with the surface roughness analysis results for both coating methods. This work enables fabricating stabilized planar PSCs through a low-cost, industrial printing technique.[195]

Zhuldyz Yelzhanova's team investigated the impact of various growth parameters on solvothermal-grown SnO_2 nanostructures. They studied factors like the growth pressure, substrate orientation, solvent ratios, seed layer types, and growth time. Key findings included that adjusting the precursor volume could optimize the pressure, the substrate orientation affects the nanorod growth direction, and the solvent ratios influence the nanorod density. They noted that the seed layers on FTO significantly influenced the SnO_2 structure morphology. Elongated nanorods were used using a two-step solvothermal method, but the thickness increase remained challenging. For PSCs, employing solvothermal SnO_2 nanostructures as ETLs required oxygen plasma surface treatment to enhance the photovoltaic performance. Fig. 17 presents the current–voltage characteristics of photovoltaic cells utilizing SnO_2 nanorod arrays, with and without oxygen plasma treatment. Moreover, SEM top-view and cross-sectional images are displayed for the SnO_2 nanostructures grown in autoclaves of differing volume sizes:

(a, d) 25 mL, (b, e) 50 mL, and (c, f) 100 mL. Additionally, SEM images of the samples exposed to solvothermal growth depict various mounting orientations: (a, d) 45°, (b, e) 90°, and (c, f) 0°. Insights for optimizing the SnO_2 nanostructure growth and for application in photovoltaic devices are provided in this study.[196]

Xiangqing Zhou's team innovatively developed a low-temperature method using Cu-doped SnO_2 as an ETL in planar PSCs. This yielded a remarkable PCE of 21.35%, surpassing the 19.63% of the control device. Cu doping improved SnO_2 conductivity and energy-level alignment, enhancing electron extraction, charge transfer, and reducing charge recombination at the SnO_2/perovskite interface. The Cu:SnO_2 ETL also enhanced the perovskite film quality, leading to more prominent grains and better light absorption and improved J_{sc} and FF values. The PSC device with the Cu:SnO_2 ETL also demonstrated exceptional stability under light and thermal conditions, outperforming the reference device. Fig. 18 presents the $J–V$ characteristics of photovoltaic devices employing SnO_2 and a 5% copper-doped tin dioxide Cu:SnO_2 as the ETL. Additionally, the figure includes FESEM images depicting the cross-section of a device with SnO_2 as the ETL, another featuring a Cu-doped SnO_2 ETL, and a third showcasing the cross-section of a device utilizing Cu-doped SnO_2 as the ETL.[197]

A novel interface modification for planar PSCs was introduced by Razieh Keshtmand's team utilizing SnO_2 and NH_4Cl. The electronic properties of SnO_2 were enhanced by NH_4Cl, while the defects at the ETL/perovskite interface were mitigated. A significant 20% efficiency increase was achieved by the
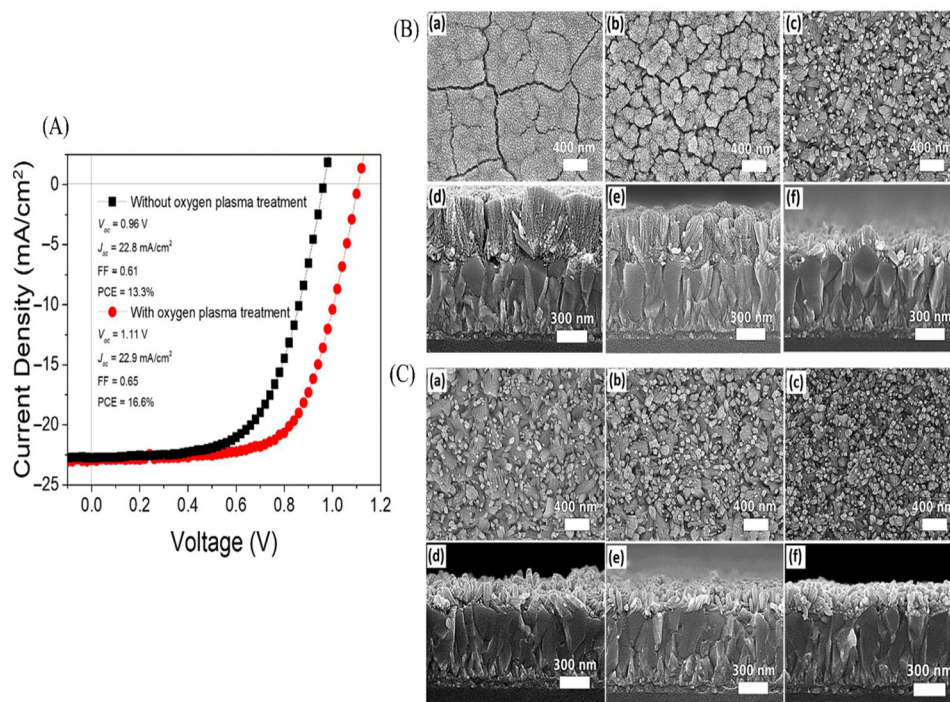

Fig. 17 (A) Current–voltage behaviours in photovoltaic cells employing SnO_2 nanorod arrays with and without oxygen plasma treatment. (B) SEM top-view and cross-sectional images showcasing SnO_2 nanostructures grown in different autoclave volumes: (a) and (d) 25 mL, (b) and (e) 50 mL, and (c) and (f) 100 mL. Additionally, (C) SEM top and cross-sectional images for samples mounted in various orientations for solvothermal growth: (a) and (d) 45°, (b) and (e) 90°, and (c) and (f) 0°. Reproduced with permission.[196] Copyright 2022, MDPI.
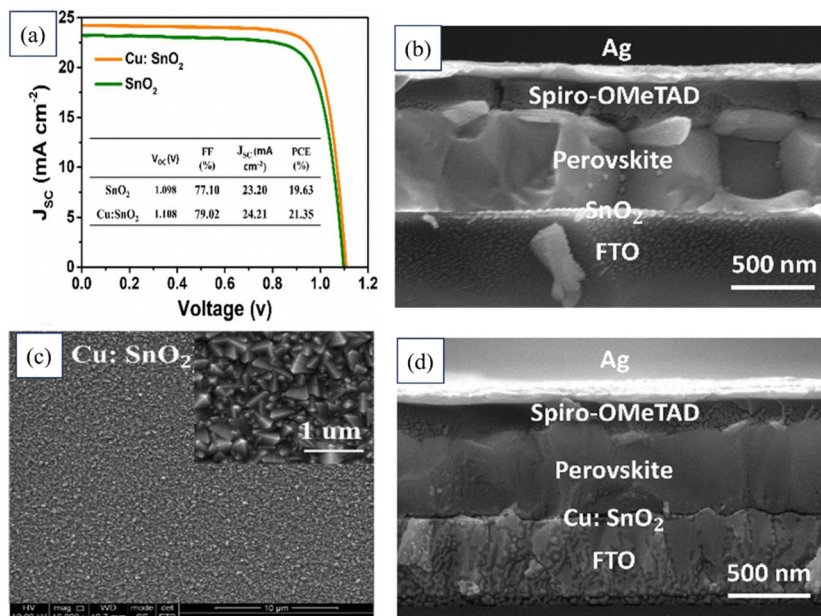
Fig. 18 (a) J–V characteristics of photovoltaic devices utilizing SnO$_2$ and a 5% copper-doped tin dioxide (Cu:SnO$_2$) ETL. FESEM images of (b) cross-section of the device with SnO$_2$ as the ETL, (c) Cu-doped SnO$_2$, (d) cross-section of the device with Cu-doped SnO$_2$ as the ETL. Reproduced with permission.[197] Copyright 2022, Elsevier.

modified SnO$_2$ (SnO$_2$–Cl$_3$) ETL variant, attributed to the improved charge transport, reduced recombination, and smoother morphology. Both SnO$_2$ and modified SnO$_2$ were utilized as ETLs in the device, as illustrated by the J–V curves in Fig. 19. Also shown in that figure are FESEM images of the SnO$_2$–Cl$_3$ sample coated on FTO, a cross-section of the device employing SnO$_2$–Cl$_3$, and the perovskite layer deposited on SnO$_2$–Cl$_3$, which served as the ETL. Notable stability was also

observed, with the strategy retaining 78% of its initial PCE over 30 days. This strategy offers the potential to enhance the efficiency and stability of PSCs.[198]

Huiming Luo's team implemented an ethanol treatment method to enhance the conductivity of SnO$_2$ film in order to improve the efficiency of PSCs and reduce hysteresis. Fig. 20 illustrates the J–V curves for devices utilizing SnO$_2$ and EtOH–SnO$_2$ as ETLs. Additionally, the cross-sectional FESEM image of
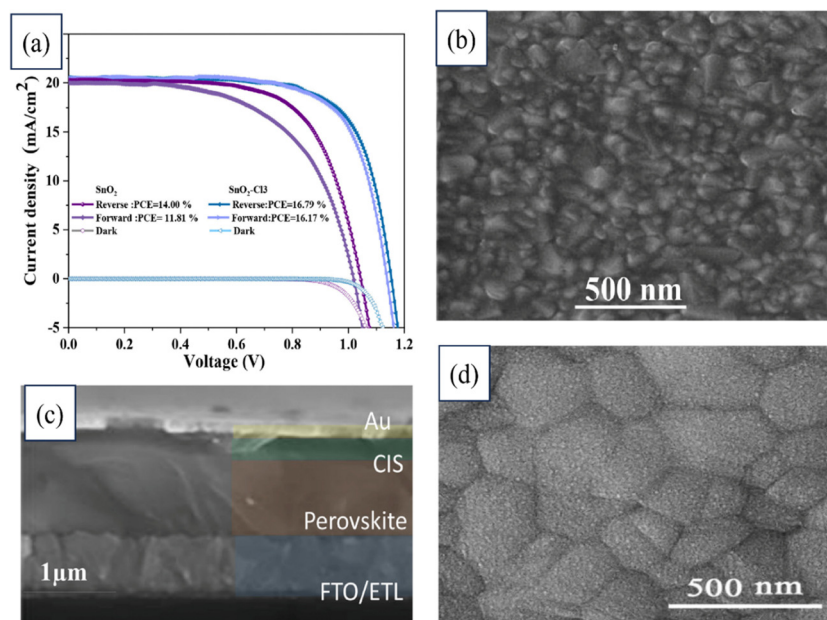

Fig. 19 (a) J–V curves of devices based on SnO$_2$ and modified SnO$_2$ as the ETL. FESEM images of (b) SnO$_2$–Cl$_3$ sample coated on FTO, (c) cross-section of a device based on SnO$_2$–Cl$_3$, (d) perovskite deposited on the SnO$_2$–Cl$_3$ ETL. Reproduced with permission.[198] Copyright 2022, Elsevier.
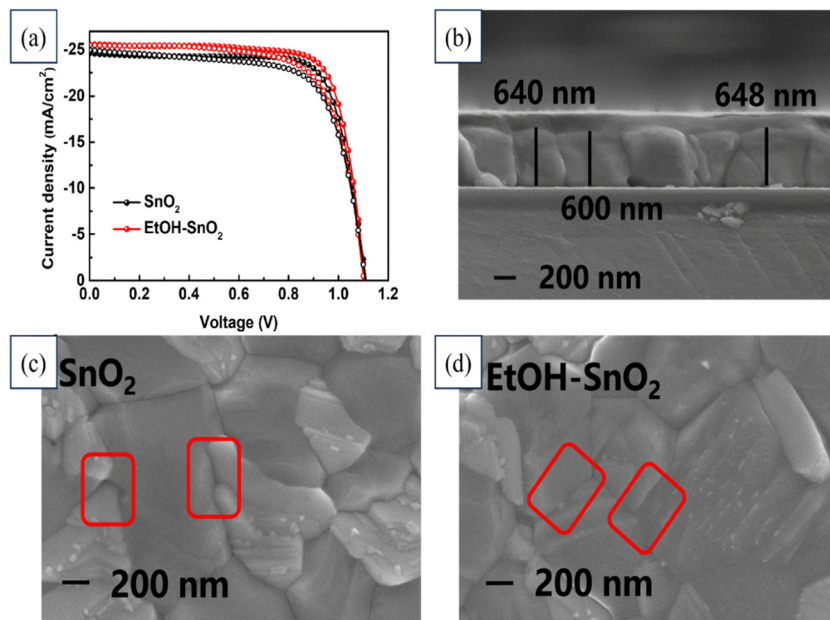
Fig. 20 (a) *J–V* curves of devices based on SnO$_2$ and EtOH–SnO$_2$ as ETLs. FESEM images of (b) cross-section of the device, (c) deposited SnO$_2$ layer, and (d) EtOH–SnO$_2$. Reproduced with permission.[199] Copyright 2022, Elsevier.

the device along with FESEM images depicting the deposited SnO$_2$ layer and EtOH–SnO$_2$ are presented. Consequently, the PSCs utilizing ethanol-treated SnO$_2$ as the ETL exhibited a noteworthy PCE rising from 20.70% to 21.62%, accompanied by a substantial increase in J_{sc}. Additionally, the PSCs encapsulated with EtOH–SnO$_2$ showed only a 20% degradation in efficiency after 1000 h of light soaking. Even the unencapsulated devices retained 80% of their original efficiency after continuous heating on an 85 °C plate for 300 h. These findings indicate that ethanol treatment could positively affect the conductivity of the SnO$_2$ layer and the overall performance of PSCs.[199]

An extensive investigation was conducted on various single- and bilayer SnO$_2$ ETLs by Abed Alrhman Eliwi's team with an aim to enhance the efficiency of planar n–i–p PSCs. Through XPS analysis, they confirmed the successful doping of Li in the c(Li)-SnO$_2$ ETL and the presence of K in ETLs formed using a commercial SnO$_2$ NP colloidal solution. A ground-breaking bilayer c(Li)-NP-SnO$_2$ ETL was introduced that ingeniously combined the advantages of Li and K. Improved charge extraction was achieved, effectively suppressing ion migration and reducing charge accumulation at the perovskite/ETL interface. The exceptional performance of the developed double-cation PSC with c(Li)-NP-SnO$_2$ ETL was demonstrated, whereby a remarkable PCE of 20.4% was exhibited in the $-V$ scan and, even more impressively, a stabilized PCE of around 18.5% was maintained after MPP tracking for 300 s. Notably, substantially reduced hysteresis and significant enhancements in both the FF and J_{sc} were demonstrated by this champion PSC compared to other optimized ETL configurations, as shown in Fig. 21. This figure also shows FESEM images of the perovskite-coated layers of these SnO$_2$ layers.[200]

Haibing Wang's team proposed a simple yet effective strategy by incorporating H$_2$O$_2$ into the commonly used SnO$_2$ colloid

precursor, and revealed this could enhance the ETL quality, while reducing trap densities and making electron extraction more efficient. Introducing H$_2$O$_2$ into the SnO$_2$ precursor also aligned the Fermi level of the H$_2$O$_2$–SnO$_2$ ETL better with the perovskite's CB, thereby benefiting an improvement in the V_{oc}. Moreover, perovskite grown on the H$_2$O$_2$–SnO$_2$ substrate demonstrated fewer trap densities. Employing H$_2$O$_2$–SnO$_2$ as the ETL yielded significant enhancements in PSC performance, long-term stability, and device fabrication repeatability. Fig. 22 illustrates the *J–V* characteristics of devices utilizing SnO$_2$ and H$_2$O$_2$–SnO$_2$ ETLs. The schematic diagram depicts the employed process, while the top-view SEM images showcase the pristine SnO$_2$ film, and H$_2$O$_2$–SnO$_2$ film. This pioneering study revealed the impact of H$_2$O$_2$ on enhancing the SnO$_2$ ETL, offering a novel approach for boosting PSC efficiency and device fabrication consistency. Further, this strategy introduces a new direction for designing SnO$_2$-based devices based on the reduction of oxygen defects.[201]

Enqi Wang and colleagues effectively showcased a novel approach to enhance the efficacy of SnO$_2$ ETLs through ethanol vapour treatment during annealing. In contrast to conventional annealing techniques, this method substantially enhanced the electrical characteristics of the SnO$_2$ film. Additionally, when the perovskite light-absorbing layer was applied to the ethanol-treated SnO$_2$ film, it yielded heightened light absorption and a diminished density of trap states in the light-absorbing material. Consequently, PSCs produced using the ethanol-treated SnO$_2$ film as the ETL demonstrated enhanced electron injection and transfer, leading to minimized charge recombination. These advancements resulted in improved V_{oc} and FF values, culminating in an impressive 17.66% PCE. Fig. 23 presents the *J–V* curves of the device, illustrating the impact of ethanol vapour treatment on the SnO$_2$ film. The schematic of the
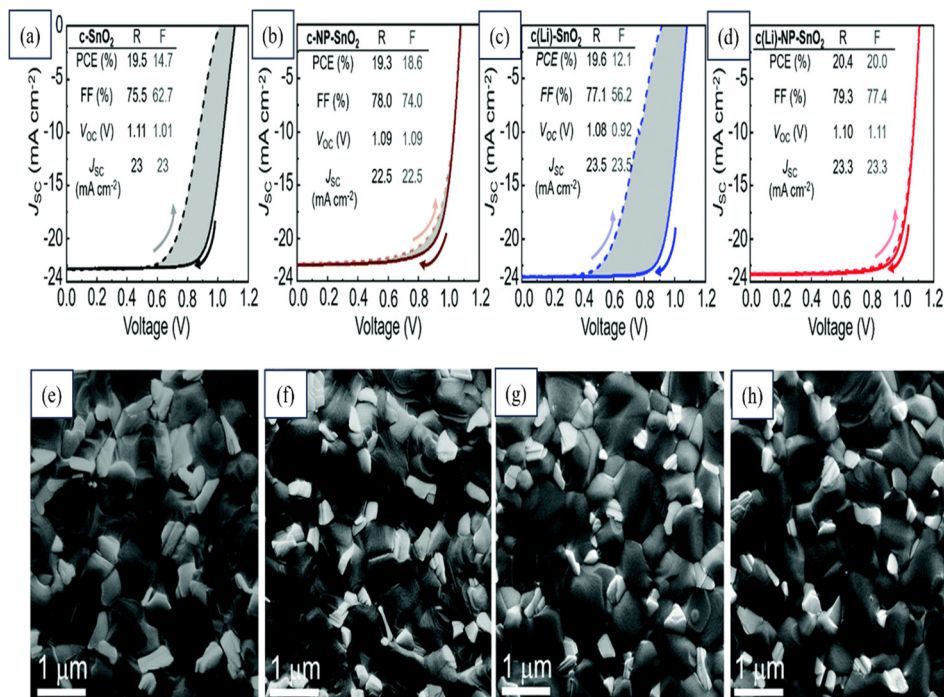
Fig. 21 Reverse (R) and forward (F) $J-V$ scans and stabilized PCE (s-PCE) derived from MPP tracking of champion PSCs with (a) c-SnO$_2$, (b) c-NP-SnO$_2$, (c) c(Li)-SnO$_2$, and (d) c(Li)-NP-SnO$_2$ ETLs. Top SEM images of perovskite thin films deposited on (e) c-SnO$_2$, (f) c-NP-SnO$_2$, (g) c(Li)-SnO$_2$, and (h) c(Li)-NP-SnO$_2$ ETLs. Reproduced with permission.[200] Copyright 2022, Royal Society of Chemistry.

experimental set-up for ethanol vapour is presented, along with SEM images showcasing the SnO$_2$ layer deposited in ethanol vapour and a cross-section of the tested device. These remarkable findings introduce a fresh avenue for enhancing the PCE in PSCs by subjecting the ETL to ethanol vapour treatment during the annealing process.[202]

Table 11 gives an overview of the synthesis methods, device structures, and their respective solar cell parameters, from which it can be seen that spin-coating emerges as a highly effective deposition method in the realm of PSC fabrication, consistently demonstrating favourable outcomes with notable PCE values ranging from 10.18% to 20.9%. Remarkably, certain
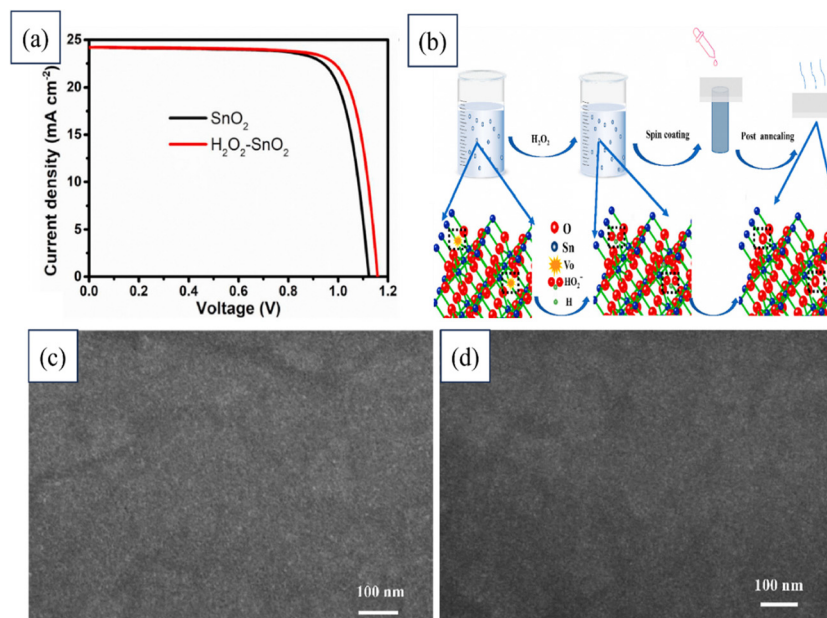

Fig. 22 (a) $J-V$ characteristics of devices with SnO$_2$ and H$_2$O$_2$–SnO$_2$ ETLs. (b) Schematic illustration of process used. Top-view SEM images of (c) pristine SnO$_2$ film, and (d) H$_2$O$_2$–SnO$_2$ film. Reproduced with permission.[201] Copyright 2021, Elsevier.
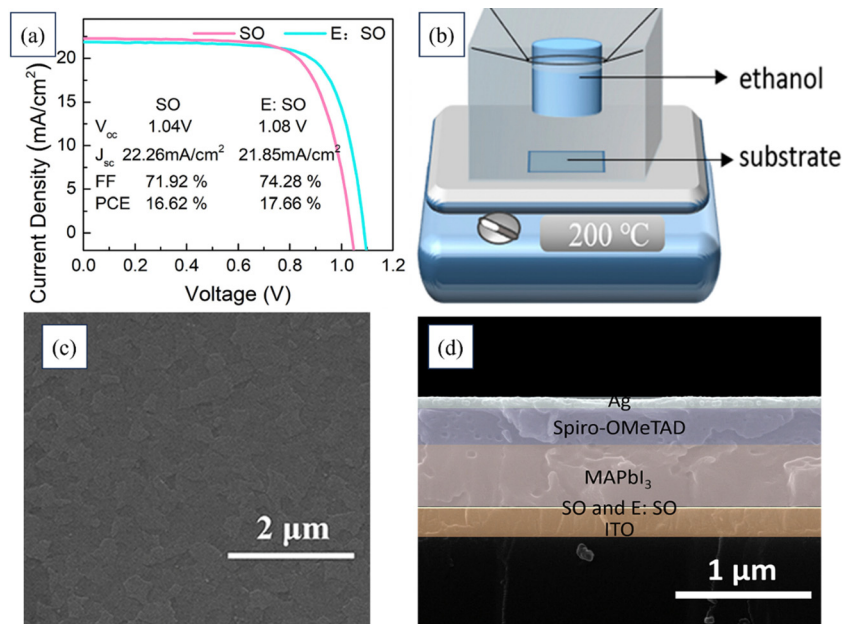
Fig. 23 (a) J–V curves of a device based on the SnO$_2$ film with and without ethanol vapour treatment. (b) Schematics of the ethanol vapour experimental set-up. SEM images of (c) SnO$_2$ layer deposited in ethanol vapour and (d) cross-section of the tested device. Reproduced with permission.[202] Copyright 2020, Elsevier.

devices even surpassed the 20% threshold, underscoring the significant potential of this technique for enhancing PSC technology. In particular, devices incorporating FTO/SnO$_2$ as the ETL exhibited a desirable PCE and FF, indicating the efficacy of this specific ETL combination in improving device performance. Additionally, the highest PCE of 20.9% achieved through spin-coating underscores its promising applicability in producing PSCs with enhanced efficiency. Despite the prominence of spin-coating, alternative deposition methods, such as ALD, also show promise, yielding devices with respectable PCE values. Conversely, hydrothermal and electrodeposited approaches exhibit relatively lower PCE values, suggesting the necessity for further optimization efforts in these deposition methods to enhance their performance in PSC applications. Overall, while spin-coating with FTO/SnO$_2$ as the ETL presents

a consistent and promising option, the exploration of other methods, like ALD and solution-processed chemical bath deposition (SC-CBD), holds potential for achieving high PCE values in PSCs.

2.6. Modification strategies of SnO$_2$ as ETLs

Modifications of the photoanode are often utilized to mitigate electron recombination phenomena in photovoltaic devices. Various strategies, such as elemental doping, incorporating additional ETLs, and surface modifications, have been extensively utilized for modifying SnO$_2$-based photoanodes. Significant improvements in the performance of photovoltaic devices have been demonstrated through these modifications, particularly in the following aspects: (1) the passivation of surface states can be facilitated by elemental doping, leading to a

Table 11 Overview of the synthesis methods, device structures, and their respective solar cell parameters

Deposition method	Device structure	V_{oc} [V]	J_{sc} [mA cm^{-2}]	FF [%]	PCE [%]	Ref.
SC-CBD	FTO/SnO$_2$/(FAPbI$_3$)(MAPbBr$_3$)/spiro-/Au	1.18	22.73	77	20.78	203
Electrodeposition	ITO/SnO$_2$/MAPbI$_3$/spiro-/Ag	1.08	19.75	65	13.88	204
Spin-coating	ITO/SnO$_2$/(FAPbI$_3$)(MAPbBr$_3$)/spiro-/Au	1.09	24.88	75.73	19.9	205
PLD	FTO/SnO$_2$/PCBM/MAPbI$_3$/spiro-/Au	1.11	21.6	71	17.03	203
Spin-coating	ITO/SnO$_2$/MAPbI$_3$/spiro-/Au	1.15	21.74	80.9	20.23	206
Spin-coating	FTO/SnO$_2$/MAPbI$_3$/spiro-/Au	1.023	21.19	67.8	14.69	207
Spin-coating	FTO/SnO$_2$/(FAPbI$_3$)(MAPbBr$_3$)/spiro-/Au	1.13	23.05	79.8	20.79	208
Spin-coating	FTO/Nb:SnO$_2$/MAPbI$_3$/spiro-/Au	1.08	22.36	72.7	17.57	209
ALD	FTO/SnO$_2$/(FAPbI$_3$)(MAPbBr$_3$)/spiro-/Au	1.14	21.3	74	18.4	210
Spin-coating	ITO/SnO$_2$/(FAPbI$_3$)(MAPbBr$_3$)/spiro-/Au	1.12	23.86	80.6	20.9	211
Spin-coating	FTO/SnO$_2$nanosheet/MAPbI$_3$/spiro-/Au	1.11	23.27	67	17.21	212
Spin-coating	FTO/bl-SnO$_2$/mp-SnO$_2$/MAPbI$_3$/spiro-/Au	0.933	17.38	62.8	10.18	213
PEALD	FTO/SnO$_2$/C$_{60}$-SAM/MAPbI$_3$/spiro-/Au	1.13	21.56	78.11	19.03	214
Hydrothermal	FTO/SnO$_2$nanosheet/MAPbI$_3$/spiro-/Au	1.05	22.76	68	16.17	215
Spin-coating	ITO/SnO$_2$/(FAPbI$_3$)(MAPbBr$_3$)/EH44/MoO$_x$/Al	1.091	21.71	77.9	18.5	216

reduction in recombination rates; (2) the morphology of the absorber layer can be enhanced and intimate contact at the interface promoted by modifications, also enhancing charge-transfer efficiency; (3) the long-term stability and durability of photovoltaic systems can be significantly enhanced by modification of the photoanodes.

2.6.1. Doping. Utilizing metal cations in the composition of ETLs presents a promising method to enhance the characteristics of both the ETLs and their interfaces with perovskite materials. Incorporating metal oxides through doping can effectively enhance the coverage of thin films, inducing a favourable change in energy levels that align well with adjacent layers. This process also leads to increased conductivity in thin films, significantly improving device performance. To date, several metal aliovalent cations, including Al^{3+}, Li^+, Sb^{3+}, Mg^{2+}, Cl^-, F^-, Zn^{2+}, Ta^{5+}, Ln and La^{3+}, have been employed for doping into SnO_2 ETLs. A comparative analysis of the PCEs of PSCs with doped SnO_2 ETLs *versus* undoped ones indicated that all devices exhibited enhanced PCEs following the incorporation of metal cations. Table 12 offers a comprehensive overview of the impact of doping. The doping of SnO_2 with various elements has been extensively explored to enhance the performance of PSCs. For instance, tantalum (Ta) doping has been shown to improve the conductivity and optical transmittance of SnO_2 further, thereby enhancing the overall PSC performance.[217] The incorporation of $TaCl_5$ into SnO_2 solutions results in the formation of a neutral and hydrophobic surface, which enables efficient electron transfer by causing downward

shifting of the CB of the ETLs. A reduction in hysteresis in PSCs and enhancement in the energy-level structure and contact between the ETLs and perovskite materials can be achieved through this doping strategy.[218] Similarly, chlorine (Cl) doping improves the energy-level structure and enhances the contact between the ETLs and perovskite materials. This leads to an elevated Fermi level, which enhances energy alignment, reduces barriers, increases carrier extraction, and boosts the V_{oc} of solar cells.[219] Additionally, the hydrophobic surface of SnO_2–Cl increases the grain sizes and reduces interfacial recombination in the perovskite film, further enhancing PSC performance.[220] Introducing lithium (Li) as a dopant within SnO_2 enhances its conductivity, facilitating electron injection and transfer, while inhibiting charge recombination.[221] The incorporation of Li^+ ions also leads to a significant improvement in the electrical conductivity of SnO_2, accompanied by a downward shift in the CB minimum, which aids in the effective injection and transmission of electrons from the CB of the perovskite material.[222,223] Furthermore, sodium (Na) doping of the ETL has been observed to enhance the crystallinity and absorbance characteristics of perovskite films. These doped ETLs have also demonstrated the capability to passivate interface defects between the perovskite film and the SnO_2 ETL, contributing to improved PSC performance.[224] Additionally, doping SnO_2 with rare-earth (Ln) ions enhances the development of uniform and large perovskite crystals, improving interfacial contact within the device. Ln dopants also optimize the energy level of the ETL, resulting in reduced resistance and mitigated charge trap states, thereby facilitating efficient electron transport and charge extraction.[225] Moreover, aluminium (Al) doping of SnO_2 improves transparency, conductivity, and band alignment, further enhancing the photovoltaic properties of PSCs.[226,227] Lastly, doping with zinc (Zn) has been observed to elevate the CB energy and enhance the electrical conductivity of SnO_2, resulting in improved electron transfer and extraction processes, while effectively suppressing charge recombination.[228,229] Valuable insights into the design and optimization of high-performance PSCs are provided by this comprehensive exploration and understanding of the effects of doping on SnO_2-based ETLs, and underscore the effectiveness of metal cation doping as a viable approach to optimize the performance of PSCs without compromising their integrity. The effect of doping is presented graphically in Fig. 24.

2.6.2. Bilayer SnO_2 ETLs. To address the issue of pinholes and cracks occurring in SnO_2 films during fabrication, bilayer ETLs combining SnO_2 with other materials, such as TiO_2, Al_2O_3, Ga_2O_3, ZnO, SnO_2, $ZnTiO_3$, PCBM, and C_{60}, have been employed to suppress the interface and bulk defects, as well as charge recombination.

2.6.2.1. SnO_2/metal oxide ETLs. In photovoltaic systems utilizing the n–i–p architecture, bilayer metal oxide composite configurations are frequently employed as ETLs. Mali *et al.* selected SnO_2-coated c-TiO_2 bilayer ETLs to take advantage of the high electron mobility of SnO_2 compared to TiO_2. Surface traps in the TiO_2 film were suppressed by the SnO_2 layer,

Table 12 Overview of the effect of doping, and the authors' remarks and solar cell parameters

| Doped elements	V_{oc} [V]	J_{sc} [mA cm^{-2}]	FF [%]	PCE (%)	Ref.
Ta^{5+}	1.161	22.79	78.6	20.80	217
Ta^{5+}	1.08	22.73	73.5	18.23	218
Cl^-	1.195	22.1	75.6	20	219
Cl^-	1.1	23.02	69	18.1	220
Li^+	1.065	21.65	67.42	15.54	221
Li^+	0.909	19.97	76	18.35	222
Li^+	1.106	23.27	70.71	18.2	223
MSE-Na$^+$	1.12	23.88	78.69	21.05	224
1%-Sc	1.108	23.12	75.03	19.19	225
2%-Sc	1.113	23.24	75.64	19.56	
3%-Sc	1.117	23.36	76.80	20.03	
4%-Sc	1.016	20.87	69.05	14.64	
1%-Y	1.109	23.21	74.94	19.30	
2%-Y	1.112	23.35	76.56	19.81	
3%-Y	1.117	23.61	78.16	20.63	
4%-Y	1.029	21.02	70.03	15.15	
1%-La	1.106	23.11	74.79	19.13	
2%-La	1.107	23.16	75.15	19.28	
3%-La	1.111	23.21	75.57	19.49	
4%-La	1.011	20.88	67.22	14.19	
La	1.08	21.61	78.17	18.36	226
Mg^{2+}	1.1	21.68	70.5	16.82	221
Sb^{5+}	1.094	22.3	70	17.07	
Sb^{5+}	1.06	22.6	72.0	17.2	230
Al^{3+}	0.85	19.0	62	10.8	227
Al^{3+}	1.09	21.82	77.61	18.45	226
2.5% Zn–SnO_2	0.99	19.51	49.65	49.65	228
5% Zn–SnO_2	1.01	19.57	51.58	10.21	
7.5% Zn–SnO_2	1	19.47	50.1	9.77	
Zn–SnO_2	1.098	23.4	69.2	17.78	229
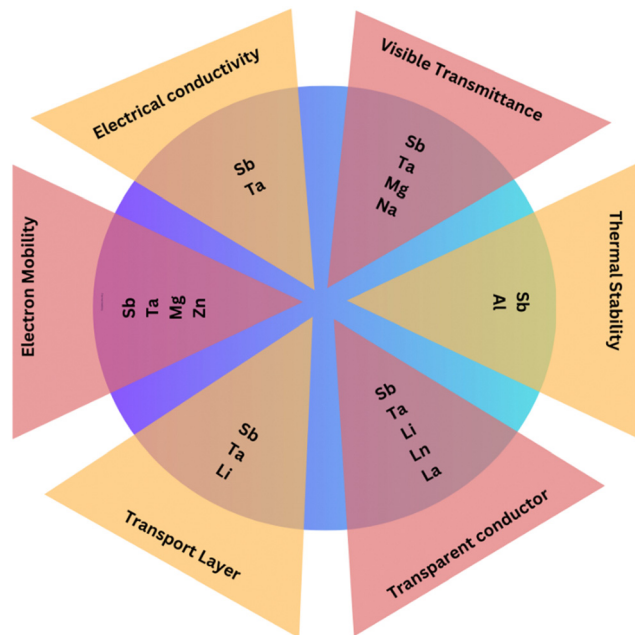
Fig. 24 Graphical representation of the effect of doping in SnO_2 on different physical properties.

allowing the effective extraction of electrons from the perovskite layer and the preservation of charge balance in the device.[231]

Wang et al. developed an In_2O_3/SnO_2 bilayer ETL prepared through a low-temperature process. The introduction of In_2O_3 resulted in smooth and low-defect-density perovskite films. The lower CB of In_2O_3 compared to Sn-doped In_2O_3 (ITO) promoted charge transfer at the interface, reducing voltage loss. The device achieved a high PCE of over 23% and demonstrated good stability.[232] A novel amorphous WO_x/SnO_2 hybrid ETL was proposed by Wang et al. to block holes and enhance charge extraction effectively. The appropriate energy-level alignment and high conductivity of the hybrid ETL facilitated electron transfer. Flexible PSCs with the hybrid ETL exhibited a higher PCE of 20.52% compared to those with the single SnO_2 ETL.[233] Ye et al. developed a doped SnO_2 bilayer ETL composed of two different SnO_2 films combined with NH_4Cl as an additive. This bilayer structure could tune the bandgap alignment at the SnO_2/perovskite interface, reducing strain in the perovskite film growth and minimizing carrier recombination. The optimized device with the doped SnO_2 bilayer ETL achieved a remarkable PCE of 21.75% and increased the V_{oc} to 1.21 V, with negligible hysteresis.[234] The effectiveness of bilayer ETLs incorporating SnO_2 in improving the

performance and stability of PSCs by suppressing defects, enhancing charge extraction, and optimizing bandgap alignment at the interface was demonstrated by these studies.

2.6.2.2. SnO_2/fullerene derivative ETLs. Caruso and colleagues showed that incorporating C_{60} onto the surface of SnO_2 nanosheets led to the partial occupancy of the surface trap states, neutralising both interfaces: C_{60}/perovskite and SnO_2/C_{60}. The enhanced alignment of the bands decreased the recombination of charges between electrons and holes that were injected by light into the perovskite layer. This led to an improved V_{oc} and effectively suppressed the recombination of charges.[235]

Surface modification with a SnO_2/C_{60} self-assembled monolayer (SAM). Like various metal oxides, SnO_2 can establish robust electronic coupling with a self-assembled monolayer of C_{60}. This interaction allows for better surface characteristics and the mitigation of ion migration. Jen et al. and Yan et al. reported impressive PCEs of 15% while minimizing hysteresis by introducing a C_{60}-SAM to the SnO_2 surface. Nevertheless, the slow process of anchoring SAMs poses obstacles to large-scale manufacturing.[236]

SnO_2/PCBM bilayer. Fang and colleagues achieved a 19.12% PCE using a bilayer approach. This method mitigated the perovskite layer's defects within grains by incorporating dissolved PCBM. At the same time, the interface retained a fragile layer of fullerene, leading to an improved extraction of charges. The development of new fullerenes that are insoluble in perovskite solvent could improve the reproducibility.[237]

SnO_2/graphene quantum dots (GQDs) composite. A SnO_2/graphene quantum dots (GQD) composite was employed by Yu et al. and achieved a PCE of 20.23%. The device performance was improved by incorporating the GQDs, which aided in transporting electrons generated by light to the CB of SnO_2. Electron-trap sites were effectively occupied in this process, leading to an enhancement of the Fermi level and conductivity within SnO_2. Additionally, interfacial recombination between the ETL and perovskite was reduced.[238] *Table 13* provides a comprehensive overview of the effects of SnO_2 modifications, encompassing deposition methods, device structures, and associated solar cell parameters, for promoting a thorough understanding in this area.

Table 13 Overview of the effect of SnO_2 modifications, including the deposition methods, device structures, and solar cell parameters

Deposition method	Device structure	V_{oc} [V]	J_{sc} [mA cm^{-2}]	FF [%]	PCE (%)	Ref.
Spin-coating	FTO/SnO$_2$/PCBM/MAPbI$_3$/spiro-/Au	1.12	22.61	75.8	19.12	238
Spin-coating	ITO/In$_2$O$_3$/SnO$_2$/perovskite/spiro/Au	1.17	24.45	87.09	23.24	235
PEALD	FTO/SnO$_2$/C$_{60}$-SAM/MAPbI$_3$/spiro-/Au	1.13	21.56	78.11	19.3	237
Hydrothermal	FTO/SnO$_2$ nanosheet/C$_{60}$/MAPbI$_3$/spiro-/Au	1.039	23.62	75	18.31	238
Spin-coating	ITO/P-SnO$_2$/B-SnO$_2$/perovskite/spiroOMeAD/Au	1.21	23.6	76.2	21.75	235
Spin-coating	ITO/SnO$_2$:GQDs/MAPbI$_3$/spiro-/Au	1.134	23.05	77.8	20.31	237
Vacuum thermal evaporation	FTO/SnO$_2$/TiO$_2$/perovskite/spiro-OMeTAD/Ag	1.11	23.01	80.34	20.52	233

3. Role of Sn in the absorber layer

Solar power as a clean and renewable energy source has gained momentum in recent decades, offering a solution to reduce reliance on fossil fuels. However, the presence of toxic lead in traditional lead halide PSCs raises concerns. To address this issue, researchers are focusing efforts on lead-free alternatives, for ensuring high performance and mitigating environmental and health risks. Materials such as MAPbI$_3$ and FAPbI$_3$, which are lead halide perovskites, have exhibited improved PCEs due to their optoelectronic properties, including direct bandgap, high charge-carrier lifetime, high mobility, and strong light absorption. These attributes underpin their exceptional performance.[239–241] Yet, Pb toxicity poses challenges, and is linked to severe health effects and is subject to strict bans by bodies like the EU due to its potential harm to health and the environment.[242,243] Stability issues further hamper the use of lead halide PSCs, which are susceptible to degradation from factors like moisture, rain, heat, and air exposure. Outdoor installation compounds these concerns. Researchers are actively aiming to develop lead-free perovskite materials with comparable or better performance.[244–246] These materials can offer safer, sustainable options for solar cell technology, addressing the health and environmental risks associated with lead. Their development aligns with the global sustainability agenda, prioritizing safe, eco-friendly, and socially responsible technologies. As clean energy demand rises, ensuring technology safety and sustainability are becoming vital.

One approach that has been newly developed to tackle the Pb toxicity problem involves the replacement of every two Pb^{2+} cations with one monovalent cation and one trivalent cation. This results in the formation of charge-ordered double perovskites with the general formula A$_2$B^{I}B^{III}X$_6$. Among the various compositions featuring double perovskite structures, Cs$_2$SnI$_6$ is considered an important material in the photovoltaics community, and is known for its superior stability and optimal bandgap. Also, its intrinsic resistance to oxidation addresses the Pb toxicity concerns. However, Cs$_2$SnI$_6$ remains a rarely explored material, and needs further in-depth study to unlock its optoelectronic potential.

3.1. Synthesis methods

3.1.1. MASnI$_3$. Researchers have investigated the synthesis and fabrication of MASnI$_3$ Sn halide perovskite materials through various methods, each offering unique insights into optimizing the synthesis conditions. A straightforward approach was investigated by Koji et al., where all the procedures were conducted in ambient air at room temperature. SnI$_2$ precursor aqueous solutions with 6.0 M iodine sources, such as HI, LiI, or NaI, were exclusively employed to synthesize MASnI$_3$ perovskites. The formation of precipitates was induced by directly adding 0.5 M MAI powder to these solutions under magnetic stirring. The ensuing solid products were collected through suction filtration using PTFE membrane filters with an average pore diameter of 1 μm and were subjected to three washes with 2-propanol. The resulting samples, denoted as PVK-A-B, where

A represents the type of iodine sources and B indicates the presence and type of reductants (without reductants; with H$_3$PO$_2$; with AA), were then dried in a vacuum at room temperature for at least 2 h.[247] Yue Yu et al. utilized a different strategy for fabricating thin films of MASnI$_3$, employing a dual-source evaporation system. Two substrates were used: soda-lime glass (SLG) for material characterization and pre-patterned ITO-coated SLG for device fabrication and characterization. Before deposition, the substrates underwent a sequential ultrasonication process in diluted Micro-90 detergent, deionized water, acetone, and isopropanol, followed by drying in flowing nitrogen gas. Co-evaporation was carried out using SnI$_2$ and MAI as inorganic and organic precursors. The deposition rate of SnI$_2$ was monitored using a quartz crystal microbalance, while the vapor-phase pressure of MAI was monitored due to the difficulty in directly measuring its deposition rate. The deposition parameters included a 1:1 molar ratio between the two precursor sources, maintaining a constant substrate rotation speed of 10 rpm, and intentionally avoiding substrate heating. The stability of the as-deposited CH$_3$NH$_3$SnI$_3$ thin films was observed for up to months when they were stored in a nitrogen-filled glove box in the dark.[248]

A solution-based method for MASnI$_3$ perovskite layer fabrication was adopted by Fujihara et al. Here, glass substrates with ITO underwent cleaning through ultrasonication and ultraviolet-ozone treatment. Deposition of the hole-transporter poly(3,4-ethylenedioxythiophene) polystyrene sulfonate (PEDOT:PSS) on the substrates was performed via a two-step spin-coating process, followed by annealing. The precursor solution was then utilized, consisting of MAI, SnI$_2$, and SnF$_2$, in dimethyl sulfoxide (DMSO) in a specific molar ratio. In the SB method for Pb perovskites, MAI and MAPbI$_3$ were slightly dissolved in toluene, with toluene serving as an anti-solvent.[249] Ambient room condition synthesis was explored by Swati et al. using an anti-solvent crystallization technique. A stirred equimolar ratio of SnI$_2$ and MAI was employed in diethyl ether or toluene at 50 °C overnight. To obtain the MASnI$_3$ perovskite powder, the precursor solution underwent evaporation using a hot plate and was then annealed at 180 °C. For MASnI$_3$ perovskite films, the precursor solution was combined with toluene and sprayed onto an Au/Ti-coated polyimide substrate using an airbrush via a nitrogen gas flow. The deposition of Ti (10 nm)-buffered Au (100 nm) bottom electrodes onto a polyimide substrate was carried out via direct current (dc) sputtering.[250]

In the distinct approach of Zhun Yao et al., MASnI$_3$ wafers were prepared by an elaborate process. First, CH$_3$NH$_3$I (MAI) was prepared by reacting HI and MA with a molar ratio of 1:1.2. Freshly synthesized MAI and SnO were dissolved in a mixed solvent of HI and H$_3$PO$_2$ at 80 °C, leading to the formation of a transparent yellow precursor solution. The solution was then gradually cooled to 98 °C over 12 h, allowing tiny crystalline seeds to form on the solution surface. With extending the reaction time, these seeds grew into larger wafers, eventually sinking into the solution as they became enlarged. This meticulous process showcased an alternative route for the synthesis of MASnI$_3$ wafers.[251]

3.1.2. FASnI$_3$. The reviewed papers described a variety of innovative approaches for synthesizing FASnI$_3$ perovskite

crystals, contributing to the diversity of techniques for fabricating these materials. Ke et al. adopted a method involving the dissolution of $SnCl_2 \cdot 2H_2O$ and formamidine acetate salt in an aqueous HI and H_3PO_2 mixture. A bright yellow solution was obtained as a result of this process, with crystals forming upon cooling. The formed crystals were collected by suction filtration and dried, with adjustments made for different molar ratios, highlighting the tunability of the synthesis process.[252] Chen et al., on the other hand, employed a ligand-assisted reprecipitation (LARP) method. This technique was carried out in a N_2-filled glove box, ensuring an oxygen-free environment. Here, a precursor solution of FAI and SnI_2 in N,N-dimethylformamide (DMF) was added dropwise to toluene, a "poor solvent," in the presence of the ligands oleylamine (OLA) and oleic acid (OA). The non-equilibrium state of supersaturation induced spontaneous precipitation and crystallization reactions, allowing for the controlled formation of colloidal nanoparticles. The purification process involved centrifugation, and demonstrated the precision and control achievable through this method.[253]

Mengs et al.'s approach first involved the preparation of a precursor solution for a $FASnI_3$–FOEI perovskite film. This solution consisted of SnI_2, FAI, FOEI, and SnF_2 in DMSO. The spin-coating process and introduction of chlorobenzene during the coating process further highlight the intricacies involved in optimizing the film quality and thickness.[254] Kayesh et al. employed equimolar ratios of SnI_2 and FAI with SnF_2 in DMSO for obtaining a $FASnI_3$ film. Notably, the co-addition of N_2H_5Cl as a co-additive was utilized, showcasing an innovative modification to influence the film properties. The spin-coating process and annealing emphasized the importance of post-synthesis treatments for achieving the desired film characteristics.[255] Wang's team demonstrated the OA growth mechanism of THPs using POEBr to tune the surface energy. The obtained $FASnI_3$–POEBr perovskites exhibited OA kinetics, yielding dense, smooth, oriented THPs with fewer defects and achieving 14.32% efficiency. Further study is needed to understand the crystal interaction, microstructure influence, and the role of organic cations in the rational perovskite design and the novel potential applications.[256]

3.1.3. CsSnI₃. Various methods have been explored for the synthesis of $CsSnI_3$ perovskite materials, each offering distinctive approaches and advantages. A straightforward two-step process was presented by K. Shum et al., wherein an equimolar mixture of anhydrous CsI and SnI_2 was dissolved in DMF with DMSO solvent. This yellow-orange solution underwent filtration and was subsequently spin-coated multiple times to form the $CsSnI_3$ perovskite films.[257] The method employed by Yuanyuan Zhou et al. was a two-step synthesis process, in which anhydrous CsI and SnI_2 powders were dissolved in a mixed polar organic solvent. A clear yellow solution was obtained, from which thin films of B-γ-$CsSnI_3$ were obtained upon solvent evaporation. Furthermore, a solution diluted ten-fold was drop-cast onto transmission electron microscopy (TEM) sample grids, resulting in the formation of $CsSnI_3$ nanoparticles. It is noteworthy that all the procedures were carried out in a dry Ar glovebox.[258]

Yu Jin Kim et al. introduced a two-step process for the synthesis of $CsSnI_3$ crystals. In the first step, a Sn precursor layer comprising SnI_2 and SnF_2 was spin-cast onto an ITO/poly(3,4-ethylenedioxythiophene):polystyrene sulfonate (PEDOT:PSS) substrate and then annealed. The second step involved drop-casting a CsI precursor solution onto the crystallized Sn precursor layer, initiating the $CsSnI_3$ synthesis reaction. The entire process, including preparing the precursor solutions, was carried out in a nitrogen-filled glovebox.[259] Feng Liu et al.'s approach focused on the synthesis of $CsSnI_3$ QDs. Here, a mixture of SnI_2 and PbI_2 in tri-n-octylphosphine was injected into a solution of Cs_2CO_3, oleic acid, and OLA in octadecene. The resulting QDs were purified through centrifugation and washing with methyl acetate, providing a more refined $CsSnI_3$ QD solution. Notably, the synthesis and purification processes did not require use of a nitrogen-filled glovebox.[260]

Yangyang Wang et al. described a one-pot preparation process for $CsSnI_3$ QDs, comparing two parallel solutions with and without acetylsalicylic acid (ASA). The colour changes during the synthesis process indicated the influence of ASA on the reaction. Process 1, without ASA, resulted in a bright yellow solution, while process 2, with ASA, turned brown-red and eventually black after heating. The synthesis was conducted in a N_2 glovebox.[261] In contrast, M. Han et al. adopted a solid-source CVD method to synthesize lead-free $CsSnX_3$ nanowire arrays. Here, SnX_2 and CsX powders were positioned in different zones within a horizontal tube furnace, with the growth substrates placed downstream. The growth chamber was purged with argon, and the precursors were heated, and the nanowire arrays were allowed to grow before cooling to room temperature.[262] These diverse approaches highlight the versatility of synthesizing $CsSnI_3$ materials, offering researchers various options to tailor the perovskite properties for specific applications.

3.1.4. Cs₂SnI₆. Researchers have tried methods like spin-coating and electro-spraying hydrothermal and vacuum-based techniques to synthesize Cs_2SnI_6. Nairui and colleagues investigated a straightforward approach to obtain Cs_2SnI_6 powder in one swift step, exploring how different reaction conditions and solvent choices shape the end product. They discovered that specific ratios of CsI to SnI_4 or CsI to SnI_2, paired with solvents like acetonitrile or anhydrous ethanol, could yield pure and finely crystallized Cs_2SnI_6 powder with enhanced electrical properties and stability. Their investigations revealed the pivotal role of solvent selection in modulating the optical and electrical traits of the obtained Cs_2SnI_6 films. Films crafted with anhydrous ethanol boasted superior crystallinity, resulting in heightened optical absorption, enhanced mobility of the charge carriers, and reduced carrier concentration compared to those from other solvents. This underscores the significance of the solvent choice in tailoring Cs_2SnI_6 materials for diverse applications.[263] Pure CsI crystallites were obtained through electro-spraying. Following this, the CsI layer was treated with a solution of SnI_4 in ethanol to create the Cs_2SnI_6 film. Optimal conditions for the formation of the Cs_2SnI_6 film were found to be 110 °C for 20 min, with the CsI film subsequently annealed

at 300 °C for 30 min. However, increasing the annealing temperature of CsI resulted in an uneven formation of the Cs_2SnI_6 film. Achieving high efficiency relied heavily on precise control over the film morphology, as films with pinholes and uneven coverage led to decreased light absorption and resistance. The performance of Cs_2SnI_6 can be significantly impacted by factors like the reaction conditions, preparation methods, and CsI levels. A challenge in achieving an optimized Cs_2SnI_6 thickness is presented by the limited solubility of the CsI precursor, which can be addressed through the utilization of spray-coating.[264] Mora-Seró's research team utilized the co-evaporation technique to make $CsSnI_3$ films utilizing CsI and SnI_2 reactants. However, these films changed colour under normal atmospheric conditions from dark brown to yellow accompanied by a reduction in absorbance. Interestingly, it took about 3–5 days for the gradual degradation of $CsSnI_3$ to reach completion, resulting in the formation of a reflective Cs_2SnI_6 film. Over time, the film gradually regained its light-absorption ability within the range of 700–800 nm wavelength. Furthermore, the film's original gradual slope in absorption was replaced by a flat response with two distinctive peaks.[265]

A promising method known as aerosol-assisted chemical vapour deposition (AACVD) was discovered by researchers for crafting high-quality perovskite films. In a study conducted by Ke *et al.*, a one-step AACVD process was introduced to create high-purity Cs_2SnI_6 films. In this process, a Cs_2SnI_6 solution was prepared using anhydrous *N,N*-dimethylformamide solvent. Then spin-coating and AACVD processes were utilized for film deposition. To maintain an iodine-rich environment and prevent the formation of unwanted defects, hydroiodic acid was introduced. Films produced *via* AACVD showed minimal contamination, indicating their potential for forming pure-phase Cs_2SnI_6. Remarkably, Cs_2SnI_6 films fabricated using AACVD with added hydroiodic acid displayed larger grain sizes and surface areas compared to those obtained through spin-coating. Additionally, the addition of hydroiodic acid led to the formation of pinhole-free and uniform films. Conversely, films produced without hydroiodic acid exhibited lower homogeneity, higher roughness, and more pinholes. These results highlight the significance of hydroiodic acid in achieving a uniform formation of Cs_2SnI_6 films.[266]

3.2. Classification of Sn-based absorber layers

Tin-based perovskite materials, characterized by their chemical formula ABX_3, have emerged as pivotal contenders in scientific research, particularly within the realm of photovoltaic technology. These compounds exhibit a rich diversity of structural configurations and properties, offering a nuanced landscape for exploration in photovoltaic applications.

One significant classification of Sn perovskites revolves around compounds of the ABX_3 type. This category encompasses notable examples such as $MASnI_3$, $FASnI_3$, and $CsSnI_3$. $MASnI_3$, originating from pioneering synthesis efforts in the 1970s, manifests polymorphism, transitioning between cubic, tetragonal, and orthorhombic phases. Such structural adaptability underscores its importance for achieving efficient solar cell performance. $FASnI_3$, a derivative of $MASnI_3$, stands out for its narrow band gap, rendering it a compelling candidate for solar energy conversion. Conversely, $CsSnI_3$, with its deformed three-dimensional perovskite structure and distinctive electronic characteristics, holds promise for novel applications in solar cell technology.

Another notable classification encompasses double perovskites, *i.e.* $A_2B'B''X_6$, containing Sn cations, as exemplified by Cs_2SnI_6. These materials exhibit intriguing molecular octahedral configurations, endowing them with heightened environmental stability and resistance to oxidative degradation. The unique ionic character of Cs_2SnI_6, reminiscent of a molecular salt, underscores its suitability for diverse technological endeavours. These molecules are discussed below in brief.

3.2.1. Organic cations

3.2.1.1. MASnI₃. $MASnI_3$, a lead-free perovskite material first synthesized in the 1970s, has been applicable to SCs since 2014[267] using a mesoporous scaffold. It exhibits different phases at varying temperatures: cubic, tetragonal, and orthorhombic, as shown in Fig. 25. $MASnI_3$ demonstrates diverse and adaptable properties in terms of both the structure and photovoltaic performance.[268–270]

Key properties of $MASnI_3$ include:
- Optical band gap: approximately 1.3 eV.[272]
- Low carrier concentration: about 1×10^{14} cm^{-3}.[272]
- Good electron mobility: around 2000 cm^2 V^{-1} s^{-1}.[273–275]
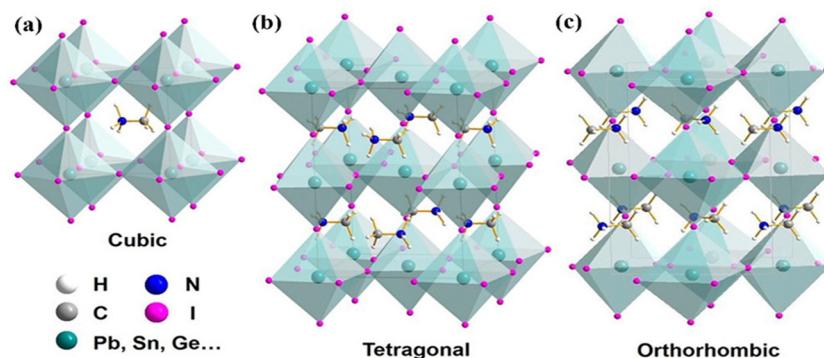

Fig. 25 Different phases of $MASnI_3$: (a) cubic, (b) tetragonal, and (c) orthorhombic. Reproduced with permission.[271] Copyright 2017, American Chemical Society.

• Bulk electrical conductivity: approximately 5×10^{-2} S cm^{-1}.[272]

• Seebeck coefficient: around 260 mV K^{-1}.[272]

• Room temperature behaviour: exhibits n-type behaviour.

Additionally, intermediate perovskites, like MASn$_{1-x}$Pb$_x$I$_3$, with increasing Sn content, exhibit superior optoelectronic performance compared to MAPbI$_3$, with a band gap of approximately 1.17 eV, high carrier concentration of about 7.94×10^{14} cm^{-3}, and large carrier mobility of around 2320 cm^2 V^{-1} s^{-1}. MASn$_{0.5}$Pb$_{0.5}$I$_3$, among various compositions, has demonstrated the best-reported PCE of approximately 14.35%, making it highly promising for energy conversion and detector devices. Furthermore, the PV output of MASn$_{0.5}$Pb$_{0.5}$I$_3$ can be influenced by its crystal symmetry and phase selection, leading to improved band gaps and economic viability compared to pure Pb-based perovskites.[276,277]

Enhancing the film quality and ensuring air stability is crucial for maximizing the PV performance of MASnI$_3$. Several fabrication techniques, including co-evaporation, sequential evaporation, and the low-temperature vapor-assisted solution process (LT-VASP), have been developed to address these challenges. SnF$_2$ doping in MASnI$_3$ films increases the fluorescence lifetime and allows the fabrication of planar structure devices without needing a mesoporous electron-selective layer. Integrating different halogens into MASnX$_3$ enables tuning the band gaps and allows control over the nucleation and growth processes, leading to an enhanced device FF. Nevertheless, there is a need to address obstacles concerning the resistance within the active and interfacial layers, as well as the electrode and contact, to enhance device performance and ensure a seamless integration with other substances. MASnI$_3$-based PSCs are susceptible to the self-doping levels of MASnI$_3$.[276,278] The cubic unit cell of a-phase MASnI$_3$ has a lattice parameter ranging from 6.231 to 6.243 Å.

The solid-state method or HI solution preparation method can be utilized to fabricate MASnI$_3$ materials, leading to variations in properties; in particular, incorporating different halides can adjust the bandgap, yielding energies ranging from 1.30 to 2.15 eV. Excellent crystallinity is exhibited by MASnX$_3$ films processed through solution methods. An estimated hole diffusion length of around 193 ± 46 nm was found for MASnI$_3$, while the electron-diffusion length was approximately 279 ± 88 nm.[272,279]

3.2.1.2. FASnI$_3$. In recent years, FASnI$_3$, a variant of the perovskite material MASnI$_3$, has garnered significant attention in photovoltaics. FASnI$_3$ possesses a relatively low band gap of approximately 1.41 eV, making it an attractive candidate for solar cell applications.[280] The rigid perovskite structure, resulting from strengthened hydrogen bonding between the larger-sized HC(NH$_2$)$_2^{+}$ cations and the Sn^{2+} matrix, contributes to enhanced temperature stability and film quality. Fig. 26 displays the unit cells with the cubic α phase, tetragonal β phase, and tetragonal γ phase. Unlike MASnI$_3$, FASnI$_3$ remains a single phase at room temperature and exhibits a high phase transition at high temperatures.

The performance of FASnI$_3$-based solar cells has been significantly improved through various optimization strategies. For instance, adding SnF$_2$ to FASnI$_3$ films led to an enhanced PCE of approximately 2.10%.[282] Further advancements have been achieved by incorporating SnF$_2$–pyrazine complex additives, which promote the growth of smooth and compact films without phase separation. These optimized films have exhibited reduced charge recombination, resulting in a high efficiency of approximately 4.8% without hysteresis behaviour.[283–286] Recent research has resulted in the development of dense, uniform, and full-coverage FASnI$_3$ films by combining a simple inverted device architecture with SnF$_2$-diethyl ether additives. A narrow band gap of around 1.40 eV was achieved by these films, achieving the highest reported PCE of about 14%.[287] The inverted device architecture, along with the incorporation of fullerene, minimized the hysteresis behaviour and demonstrated good long-term illumination stability under continuous illumination. Adding FA cations to Sn-based PSCs has proven beneficial for enhancing the performance. FA cations alleviate the tendency of Sn^{2+} oxidation and enable the formation of mixed-cation perovskites with a narrow band gap of approximately 1.33 eV.

Due to the low controllability of perovskite film growth and the inherent ease of oxidation of Sn^{2+}, Sn PSCs have been found to be significantly less efficient and stable than their Pb counterparts. Two pyridyl-substituted fulleropyrrolidines (PPF)
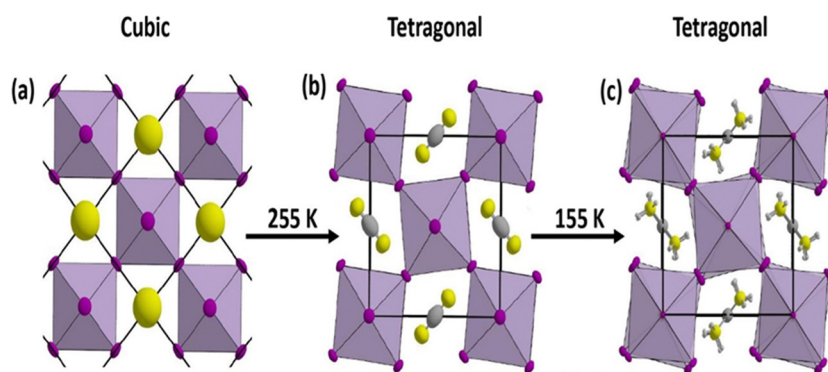

Fig. 26 Transformation of FASnI$_3$ from (a) cubic α phase at room temperature into (b) tetragonal β phase and, after that, into (c) tetragonal γ phase. Reproduced with permission.[281] Copyright 2020, American Chemical Society.

were synthesized by Chen *et al.* in the *cis* (CPPF) and *trans* (TPPF) configurations and were employed as precursor additives. The electron density distributions and interactions with perovskite components were found to be significantly influenced by the spatial arrangements of the CPPF and TPPF. In comparison to the CPPF, the TPPF featured spatially separated pyridine groups that could capture more perovskite colloids *via* coordination bonds, thereby slowing down the perovskite crystallization process. Furthermore, the crystal orientation and film quality were enhanced. The TPPF was mostly located at the grain boundaries, aiding in the improvement of the interfacial energy-level alignment by suppressing the oxidation of Sn^{2+}. Consequently, an excellent PCE of 15.38% (certified 15.14%) was exhibited by the TPPF-configured Sn PSC, with 99% and 93% of the initial PCE being maintained after 3000 h of storage and 500 h of constant irradiance, respectively.[288] Moreover, the application of $FASnI_3$-based perovskites extends beyond single-junction solar cells. A highly efficient four-terminal all-perovskite tandem solar cell, based on $FASnI_3$ perovskite as the rear junction, achieved a significant milestone, with a PCE of approximately 19.08%. Similarly, $FASn_{0.5}Pb_{0.5}I_3$ and $FA_{0.75}Cs_{0.25}Sn_{0.5}Pb_{0.5}I_3$ PSCs have achieved impressive PCEs of approximately 10.9% and 14.1%, respectively. Notably, these perovskites can be employed as rear junctions in solution-processed tandem solar cells, eliminating the need for high-temperature thermal processing.[289–295]

Research has also investigated the stability of $FASnI_3$-based perovskites. The incorporation of FA and Br into Pb- and Sn-based perovskites enables their band gaps to be tuned and their stability in the air to be enhanced. $FASnI_3$ has been found to exhibit similar thermal stability but lower conductivity compared to $MASnI_3$. Its growth conditions can be adjusted to achieve a range of conductivities, from p-type to intrinsic conductivity, while $MASnI_3$ predominantly demonstrates p-type conductivity. The large ionic size of the FA cation contributes to an increased formation energy for Sn vacancies, resulting in improved charge-carrier mobility. $FASnI_3$ has emerged as a promising absorber material for Sn-based PSCs due to its reduced bimolecular recombination and lower Auger rate than lead perovskites.[296] Furthermore, inverted $FASnI_3$-based PSCs have demonstrated superiority over $MASnI_3$-based PSCs, leading to improved device performance. Innovative growth methods and improved tolerance to oxygen make $FASnI_3$ a viable option for stable and efficient solar cell applications.[297–300] $FASnI_3$ offers numerous advantages over other perovskite materials, making it an attractive candidate for photovoltaic applications. Its low band gap, enhanced stability, and optimized film quality have contributed to the development of high-efficiency solar cells. Substantial improvements have been observed in the PCE of $FASnI_3$-based solar cells due to various optimization strategies and innovative device architectures. Great promise is held for the future of solar energy conversion by $FASnI_3$-based perovskites, supported by ongoing research and advancements.[301]

3.2.2. Inorganic cations

3.2.2.1. CsSnI₃. The distinctive characteristics and potential for advanced applications have led to considerable interest in $CsSnI_3$ perovskite materials within the realm of solar cell investigations. These perovskites come in multiple forms, such as a one-dimensional dual-chain structure with a yellow colour, a three-dimensional black perovskite configuration, and cubic black perovskite phases. $CsSnI_3$ takes on a deformed three-dimensional perovskite arrangement characterized by orthorhombic symmetry at ambient temperature.[302–305] This substance is categorized as a p-type element, displaying a moderately low density of carriers. The semiconductor capabilities of the black orthorhombic perovskite configuration of $CsSnI_3$, with a direct bandgap, can be utilized in applications, whereby light emission upon excitation and electrical conductivity both increase with rising temperature. $CsSnI_3$ also exhibits similar diffusion distances when compared to perovskite materials containing Pb. The number of carriers and the conductive properties of $CsSnI_3$ are contingent on the vacancies of Sn, I, and Cs within its structure.[306–311]

$CsSnI_3$ perovskites exhibit similar optical and electrical properties to $FASnI_3$, another popular perovskite material, but boast better thermal stability.[312,313] The three-dimensional perovskite building blocks of $CsSnI_3$ are shown in Fig. 27. Initially, they were employed as materials for transporting holes in dye-sensitized solar cells because of their significant p-type characteristic and excellent hole mobility. $CsSnI_3$'s ideal bandgap of 1.3 eV makes it intriguing for use in single-junction solar cells.[314–316] Substituting halides enables the tuning of the bandgap of $CsSnI_3$, leading to a variation from 1.3 to 1.7 eV for $CsSnBr_3$, accompanied by a change in the crystal structure from orthorhombic to cubic.[313,317] QDs of $CsSnI_3$ have achieved promising results, with a PCE of 5.03% and excellent stability over 90 days.[318] To enhance the performance of all-inorganic Sn-halide PSCs, defect passivation additives, such as thiosemicarbazide, have been utilized, resulting in a high PCE of 8.20%[319] $CsSnI_3$ PSCs have shown considerable potential, with reported PCE values of 0.9% to 8.20%, depending on various factors, such as composition engineering, device architecture, and surface passivation strategies.

Studies have demonstrated that the introduction of additives, including Sn halides, like SnF_2, $SnCl_2$, SnI_2, and $SnBr_2$, can improve film quality and enhance the performance of $CsSn(I, Br)_3$ PSCs. For instance, $CsSnI_3$ films with added $SnCl_2$ exhibited the highest pinhole density, and devices without a hole-transporting layer achieved the highest FF and PCE. Moreover, doping $CsSnI_3$ with Br resulted in $CsSnI_{3-x}Br_x$ perovskites, which exhibited higher FF values compared to pure $CsSnI_3$.[321] While all-organic $CsSnI_3$ shows possible application in inverted PSCs due to its outstanding air and thermal stability,[312,313] research efforts continue to explore different approaches to improve the stability and performance of $CsSnI_3$-based photovoltaic devices. These include localized electron density engineering, surface passivation strategies, and optimization of the device architectures. Research and development in the pursuit of high-efficiency and stable $CsSnI_3$ PSCs continues to be actively pursued. Table 14 provides a comparative analysis of lead-free perovskite device structures, presenting their corresponding solar cell parameters to understand their performance comprehensively.
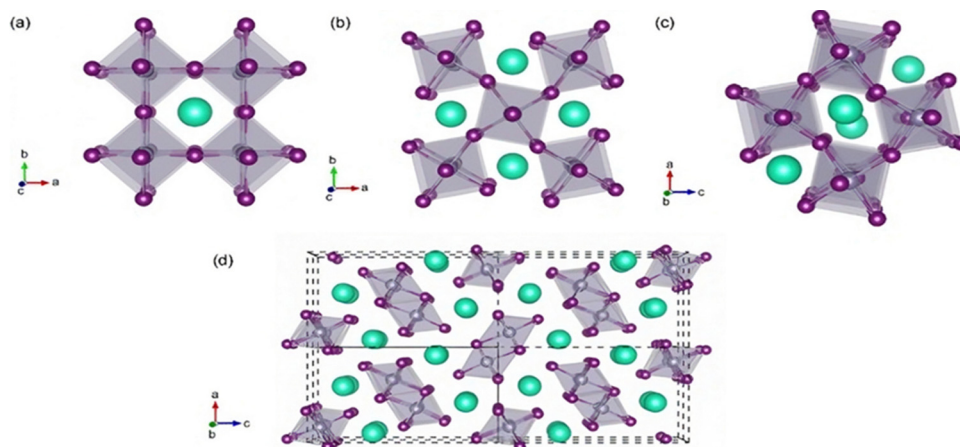
Fig. 27 One-dimensional images showing the (a) α phase in the cubic form, (b) β phase in the tetragonal form, (c) γ phase in the orthorhombic form, and (d) Sn halide octahedral networks, all broken down into one-dimensional chains in each image, the green spheres depict Cs atoms, while the purple polyhedra represent the octahedral perovskite cage formed by bonding Sn in steel blue and I in dark purple atoms. Reproduced with permission.[320] Copyright 2015, American Physical Society.

3.2.3. Double perovskites with Sn cations

3.2.3.1. Cs_2SnI_6. Cs_2SnI_6 belongs to the ⟨111⟩-oriented perovskite family, resulting from the cubic 3D structure of $CsSnI_3$, as shown in Fig. 28. Its crystallographic characteristics encompass a zero-dimensional configuration featuring distinct molecular $[SnI_6]^{2-}$ octahedra.[330,331] Within this arrangement, half of the Sn atoms within the octahedral structure at the B site remain unoccupied. This arrangement, resembling a molecular salt, exhibits a relatively ionic character, with Cs atoms occupying the spaces between the $[SnX_6]$ octahedra. The material's intrinsic resistance to oxidation and greater environmental stability are attributed to the presence of the Sn^{4+} state and strong Sn–I covalent bonds,[331–333] leading to a smaller Sn–I bond length (2.85 Å) compared to $CsSnI_3$ (3.11 Å) due to structural relaxation.[277]

The increased durability of Cs_2SnI_6 compared to $CsSnI_3$ has been validated by density functional theory (DFT) computations. Furthermore, Cs_2SnI_6 displays ambipolar characteristics, enabling it to undergo p-type or n-type semiconductor doping. Additionally, it showcases a finely tuned bandgap E_g spanning from 1.27 to 1.62 eV, rendering it a viable option for applications in photovoltaics.[334,335] The material's high absorption coefficients and carrier mobility further highlight its potential

for photovoltaics. The dual nature of Cs_2SnI_6 is due to the creation of p-type vacancies in the caesium or n-type vacancies/interstitial Sn in the iodide. Fig. 29 shows the band structure of Cs_2SnI_6, with an unmediated bandgap at the Γ juncture of around 1.3 eV, albeit minor disparities exist between the experimentally determined and theoretically projected bandgap values.[321,336,337]

Cs_2SnI_6 has shown great promise as a light-absorbing material for solar cells. Its favourable characteristics, including proximity to the Shockley–Queisser limit, suitable bandgap, and stability, have garnered significant research attention. Efforts to enhance its efficiency have been made by optimizing the device structure. For instance, Cs_2SnI_6 PSCs with c-TiO_2 and P3HT as the ETL and hole transport layer (HTL), respectively, resulted in a PCE of 0.96% and a V_{oc} of 0.51 V, mainly through optimization of the perovskite layer thickness.[339] Nevertheless, the effectiveness of Cs_2SnI_6 photovoltaic cells is impacted by the energy level disparity at the ETL/perovskite/HTL interfaces. This disparity results in a suboptimal extraction of electrons and holes, thereby resulting in the comparatively modest efficiency of the device. Under ambient conditions, the stability of Cs_2SnI_6 is considered significant, with Cs_2SnI_6 films showing

Table 14 Comparison of lead-free Sn perovskite device structures with their respective solar cell parameters

| Light absorber	Architecture	V_{oc} [V]	J_{sc} [mA cm^{-2}]	FF [%]	PCE [%]	Ref.
MASnI$_3$	FTO/c-TiO$_2$/mp-TiO$_2$/MASnI$_3$/spiro-OMeTAD/Au	0.88	16.8	0.42	6.4	269
MASnI$_3$	FTO/c-TiO$_2$/MASnI$_3$/spiro-OMeTAD/Au	0.716	15.18	0.50	5.44	322
MASnBr$_3$	FTO/c-TiO$_2$/mp-TiO$_2$/MASnBr$_3$/spiro-OMeTAD/Au	0.88	8.26	0.59	4.27	323
MASnI$_3$	FTO/c-TiO$_2$/mp-TiO$_2$/MASnI$_3$/PTAA/Au	0.27	17.4	0.39	1.86	324
MASnIBr$_2$	FTO/c-TiO$_2$/mp-TiO$_2$/MASnIBr$_2$/spiro-OMeTAD/Au	0.82	12.33	0.57	5.73	323
MASnBr$_3$	FTO/c-TiO$_2$/mp-TiO$_2$ MASnBr$_3$/P3HT/Au	0.50	4.27	0.49	1.12	325
MASnBr$_3$	ITO/PEDOT:PSS/MASnBr$_3$/PCBM/Bis-C$_{60}$/Ag	0.20	4.5	0.36	0.3	326
FASnI$_3$	ITO/PEDOT:PSS/FASnI$_3$/C$_{60}$/BCP/Ag	0.92	20.4	76.7	14.3	287
FASnI$_3$	ITO/PEDOT:PSS/FASnI$_3$/C$_{60}$/BCP/Ag	0.31	18.36	0.67	3.85	252
FASnI$_3$	ITO/PEDOT:PSS/FASnI$_3$/C$_{60}$/BCP/Ag	0.36	17.6	0.62	4.0	327
CsSnI$_3$	FTO/c-TiO$_2$/mp-TiO$_2$/CsSnI$_3$/spiro-OMeTAD/Au	0.52	10.21	0.65	3.31	328
CsSnI$_3$	ITO/PEDOT:PSS/CsSnI$_3$/PC$_{61}$BM/BCP/Ag	0.53	20.5	60.1	6.53	329
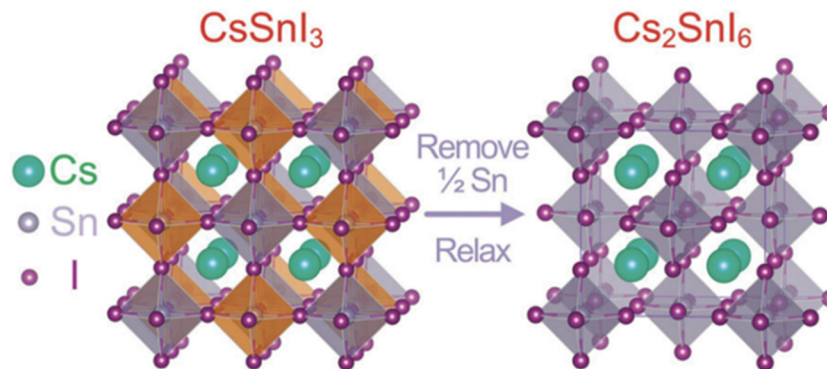
Fig. 28 Cs$_2$SnI$_6$ crystal structure derived from CsSnI$_3$. Reproduced with permission.[258] Copyright 2015, Royal Society of Chemistry.

fairly good stability for at least one week. However, the challenge of maintaining long-term stability in Cs$_2$SnI$_6$ PSCs remains. The degradation of Cs$_2$SnI$_6$ PSCs begins after one week of air exposure, and they tend to fail after one month of humidity exposure. To overcome this limitation, various materials, including the choice of the HTL, are being explored by researchers to enhance the stability and device efficiency of Cs$_2$SnI$_6$ in PSCs.[340] Despite the challenges faced in achieving high efficiency, Cs$_2$SnI$_6$ is still considered to have potential as a light-absorbing material for solar cells. A promising PCE of 0.86% was achieved in one study using a configuration with FTO/ZnO compact-layer/nanorods/ perovskite/P3HT/Ag.[341] Improvement in device performance was achieved by effectively suppressing charge recombination through the optimization of the surface morphology of the ZnO seed layer. Furthermore, the utilization of Cs$_2$SnI$_6$ in planar solar cells resulted in the attainment of a PCE of 0.46%.[342]

3.3. Methods to improve the overall performance of Sn PSCs

Apart from the use of cationic Sn in the perovskite mentioned above, researchers have developed different additive manufacturing methods to further enhance the performance of these perovskites, as discussed below.

3.3.1. Compositional engineering of tin-based perovskites. Compositional engineering crucially influences the modification of the electronic structure and stability of Sn-halide perovskites. The composition of Sn-halide perovskites can be engineered to achieve superior stability by modifying A, B, or X site cations. Successful approaches include modulating the A/X sites and employing low-dimensional composition routes. With the general formula ABX$_3$, the perovskite structure can be composed of different chemical combinations through compositional engineering. The A site can consist of organic cations, like methylammonium (MA$^+$) and formamidinium (FA$^+$), or alkali metal cations, such as caesium (Cs$^+$), which is discussed in the following sections. The B site represents a divalent metal cation (Pb^{2+}, Sn^{2+}, or Ge^{2+}), and X represents the halide anion (I$^-$, Br$^-$, or Cl$^-$). Recent advancements have introduced larger organic cations, like phenethyl-ammonium iodide (PEAI) and n-propyl-ammonium iodide (PAI), to improve stability by blocking moisture penetration and generating low-dimensional perovskite structures.[343–349] Additionally, compositional engineering can help tailor the optoelectronic properties of
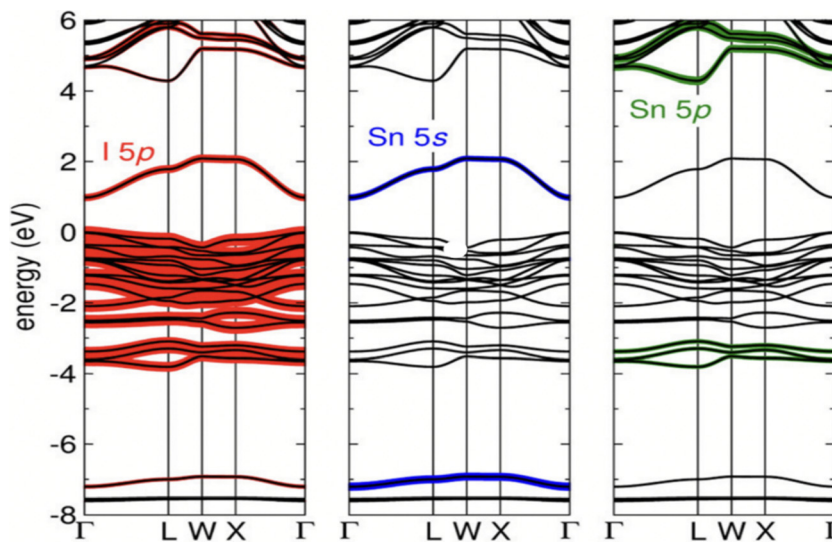

Fig. 29 Band structure of Cs$_2$SnI$_6$. Reproduced with permission.[338] Copyright 2016, American Chemical Society.

Sn-halide perovskites, reducing the formation of volatile products or irreversible disproportionation when exposed to thermal and light-induced degradation conditions. This review focuses on Sn-halide perovskites prepared as 2D or 3D films. These materials are sensitive to ambient conditions, which can impact device efficiency and long-term stability.[350–352] Compositional engineering offers a practical approach for enhancing the tolerance of Sn-halide perovskite layers by improving their optoelectronic properties and reducing degradation under challenging conditions.

3.3.1.1. Mixed cations. Perovskites based on mixed cations containing Sn have emerged as materials holding promise for the development of efficient and stable PSCs. Enhanced stability and PCEs have been exhibited by metal halide perovskites that initially explored mixed cations in Pb-based PSCs. However, previous attempts with the mixed cations MA and Cs yielded suboptimal PCEs, primarily due to the poor V_{oc}.[352–356] In this context, Zhao *et al.* investigated the influence of the mixed cations MA and FA on Sn-based perovskites. Their study revealed that the ratios of mixed cations strongly affected the optical properties of the perovskite materials. The introduction of the FA cation led to a blue-shifted emission of MASnI$_3$, indicating the tunability of the electronic structure. Control of the bandgap within the range of 1.26 to 1.36 eV for $(FA)_x(MA)_{1-x}SnI_3$ was achievable, with wider bandgaps produced by a higher FA content.[298] These mixed-cation perovskites demonstrated reduced charge-carrier recombination, improved film morphology, and enhanced photovoltaic performance. Notably, the $(FA)_{0.75}(MA)_{0.25}SnI_3$ perovskite, doped with 10 mol% SnF$_2$, exhibited an impressive maximum PCE of 8.12%.[298] The unpredictable dynamics of crystal formation of Sn perovskites result in low quality, poor orientation, and a high defect density. Jiang *et al.* used formamidine acetate (FAAc) and ammonium iodide (NH$_4$I) instead of formamidinium iodide (FAI) to grow Sn-perovskite films. The triple reagent (FAAc + NH$_4$I + SnI$_2$) technique extended the reaction path for forming Sn-perovskite films. At room temperature, it hindered the formation of 3D perovskite structures but had no effect on the low-dimensional structures. The low-dimensional structure generated at ambient temperature acted as a seed for 3D structure formation during further annealing processes. This triple reactant source produced a Sn-perovskite layer with improved orientation and long carrier lifetimes, resulting in a 14.6% efficiency for ITO/poly(3,4-ethylene dioxythiophene)/poly(styrene sulfonate) PEDOT/PSS/Sn- perovskite/indene-C$_{60}$-

bis-adduct (ICBA)/bathocuproine (BCP)/Ag perovskite solar cells.[357] Table 15 summarises the performance of this mixed cations and the respective solar cell parameters.

3.3.2. Additive engineering in organic and inorganic Sn perovskite solar cells. Initially, stabilizers and antioxidants, like SnF$_2$ and SnCl$_2$, were introduced to enhance the quality and morphology of the film, serving as stabilizers and antioxidants for Sn^{2+}. The challenges encountered in Sn PSCs have been addressed by the emergence of additive engineering, which has seen reducing additives, such as hypophosphorous acid (HPA) and metallic Sn powder, employed to reduce Sn^{4+} impurities in precursor solutions, resulting in superior film coverage and morphology. Furthermore, integrating large organic ammonium and Lewis base molecules played a pivotal role in optimizing the crystallization dynamics, thereby improving the efficiency and stability. The photovoltaic performance is summarised in Table 16. This article delves into some strategies to boost the efficiency and stability of Sn perovskite solar cells through additive engineering.

3.3.2.1. Antioxidants. Antioxidant additives are pivotal for enhancing the efficiency and long-term stability of Sn perovskite solar cells, as they shield Sn^{2+} from oxidation in ambient conditions. An array of additives, such as divalent Sn halides and hydrazine derivatives, have been incorporated to counteract this oxidation phenomenon. One notably influential group of additives among these is represented by Sn double halides, which are characterized by serving dual roles as antioxidants and Sn sources, thereby ensuring the protection of perovskite films. Mathews *et al.*[370] showcased the utilization of SnF$_2$ to diminish intrinsic Sn-cation vacancies in CsSnI$_3$ perovskites, and reported it could lower the carrier density and enhance the conductivity. The integration of 20 mol% SnF$_2$ resulted in a notable 2.02% efficiency, accompanied by an elevated current density and extended spectral response.

Similarly, Yan *et al.*[371] integrated SnF$_2$ into FASnI$_3$ films, effectively diminishing the carrier density and achieving a commendable efficiency of 6.22%. Hatton *et al.*[372] compared the efficacy of four SnX$_2$ additives (SnF$_2$, SnCl$_2$, SnBr$_2$, and SnI$_2$), and observed superior stability in SnCl$_2$, which acted as a barrier layer, effectively preventing the intrusion of oxygen and moisture. Further studies[373] showed that when SnF$_2$ and SnCl$_2$ were combined, they formed a protective layer with both amorphous and polycrystalline characteristics on the surface of perovskite films, effectively boosting the stability. This

Table 15 Comparison of mixed-cation Sn perovskite device structures with their respective solar cell parameters

Light absorber	Architecture	V_{oc} [V]	J_{sc} [mA cm^{-2}]	FF [%]	PCE [%]	Ref.
FAAc + NH$_4$I + SnI$_2$	ITO/PEDOT:PSS/FA$_{0.75}$MA$_{0.25}$SnI$_3$/ICBA/BCP/Ag	0.96	20.47	74.5	14.6	357
Cs$_{0.1}$FA$_{0.9}$SnI$_3$	FTO/c-TiO$_2$/mTiO$_2$/perovskite/ThMAI/PTAA/Au	0.521	24.12	72.02	9.06	358
FA$_{0.75}$MA$_{0.25}$SnI$_3$	ITO/PEDOT:PSS/FA$_{0.75}$MA$_{0.25}$SnI$_3$/PC$_{61}$BM/BCP/Ag	0.55	19.4	67	7.2	359
FA$_{0.75}$MA$_{0.25}$SnI$_3$	ITO/PEDOT:PSS/FA$_{0.75}$MA$_{0.25}$SnI$_3$/PC$_{61}$BM/BCP/Ag	0.55	20	65	7.1	359
FA$_{0.75}$MA$_{0.25}$SnI$_3$	ITO/PEDOT:PSS/FA$_{0.75}$MA$_{0.25}$SnI$_3$/PC$_{61}$BM/BCP/Ag	0.53	20.4	64	6.9	359
FA$_{0.75}$MA$_{0.25}$SnI$_3$	ITO/PEDOT:PSS/FA$_{0.75}$MA$_{0.25}$SnI$_3$/PC$_{61}$BM/BCP/Ag	0.54	17.2	61	5.7	359
$(FA)_{0.50}(MA)_{0.50}SnI_3$	ITO/PEDOT:PSS/(FA)$_{0.50}$(MA)$_{0.50}$SnI$_3$/PC$_{61}$BM/BCP/Ag	0.53	21.3	52.4	5.92	360
$(FA)_{0.25}(MA)_{0.75}SnI_3$	ITO/PEDOT:PSS/(FA)$_{0.25}$(MA)$_{0.75}$SnI$_3$/PC$_{61}$BM/BCP/Ag	0.48	20.7	45.2	4.49	360

Table 16 Performance of lead-free Sn perovskite devices with additive engineering and their respective solar cell parameters

Perovskite + additive	Structure of the device	V_{oc} [V]	J_{sc} [mA cm^{-2}]	FF [%]	PCE [%]	Ref.
MASnI$_3$ + SnF$_2$	FTO/c-TiO$_2$/mp-TiO$_2$/absorber/Au	0.32	21.4	0.46	3.15	361
MASnI$_3$ + hydrazine vapour	FTO/c-TiO$_2$/mp-TiO$_2$/absorber/PTAA/Au	0.38	19.9	0.51	3.80	362
MASnIBr$_{2-x}$Cl$_x$ + 0% SnCl$_2$ + 100% SnBr$_2$	Glass/FTO/TiO$_2$/absorber/carbon	0.31	13.37	0.52	2.18	147
MASnI$_3$ + SnF$_2$	FTO/PEDOT:PSS/absorber/C$_{60}$/BCP/Ag	0.45	11.8	0.40	2.14	363
en[MASnI$_3$] + SnF$_2$	FTO/c-TiO$_2$/mp-TiO$_2$/absorber/PTAA/Au	0.43	24.3	0.63	6.63	364
MASnI$_3$ + SnF$_2$	ITO/PEDOT:PSS/absorber/C$_{60}$/BCP/Ag	0.46	21.4	0.42	4.29	365
MASnI$_3$	ITO/PEDOT:PSS/poly-TPD/absorber/C$_{60}$/BCP/Ag	0.38	12.1	0.36	1.7	366
FASnI$_3$ + SnF$_2$ pyrazine	FTO/c-TiO$_2$/mp-TiO$_2$/absorber/spiro-OMeTAD/Au	0.32	23.7	0.63	4.8	56
FASnI$_3$ + 50% PEAI	ITO/PEDOT:PSS/absorber/C$_{60}$/BCP/Ag	0.38	19.96	0.69	5.28	114
FASnI$_3$ + SnF$_2$	FTO/c-TiO$_2$/mp-TiO$_2$/ZnS/absorber/PTAA/Au	0.38	23.1	0.60	5.27	75
FASnI$_3$ + LiF	ITO/PEDOT:PSS/absorber/C$_{60}$/BCP/Ag	0.38	19.65	0.71	5.04	367
FASnI$_3$ + SnF$_2$	FTO/c-TiO$_2$/mp-TiO$_2$/ZnS/absorber/PTAA/Au	0.38	23.1	0.60	5.27	75
FASnI$_3$ + LiF	ITO/PEDOT:PSS/absorber/C$_{60}$/BCP/Ag	0.38	19.65	0.71	5.04	367
FASnI$_3$ + SnF$_2$	FTO/c-TiO$_2$/mp-TiO$_2$/ZnS/absorber/PTAA/Au	0.38	23.1	0.60	5.27	75
FASnI$_3$ + diethyl ether	ITO/PEDOT:PSS/absorber/C$_{60}$/BCP/Ag	0.47	22.1	0.60	6.22	368
FASnI$_3$ + SnF$_2$	ITO/PEDOT:PSS/absorber/C$_{60}$/BCP/Ag	0.48	21.3	0.64	6.6	365
FASnI$_3$ + LiF	ITO/PEDOT:PSS/absorber/C$_{60}$/BCP/Ag	0.38	19.65	0.71	5.04	367
CsSnI$_3$ + SnF$_2$	FTO/TiO$_2$/CsSnI$_3$/m-MTDATA/Au	0.24	22.70	37.0	2.02	369
FASnI$_3$ + EVA	ITO/PEDOT:PSS/absorber/C$_{60}$/BCP/Ag	0.523	22.80	64.7	7.72	141
CsFASnI$_3$ + SnF$_2$, SnCl$_2$	FTO/PEDOT:PSS/CsFASnI$_3$/PTAA/Au	0.64	22.2	70.8	10.08	121
FASnI$_3$ + trimethylthiourea	ITO/PEDOT:PSS/absorber/C$_{60}$/BCP/Ag	0.9	21	75.69	14.06	61

protective layer was confirmed through grazing incident X-ray diffraction (GIXRD) and high-resolution transmission electron microscopy (HRTEM). As a result, the PSCs exhibited remarkable stability, experiencing minimal performance degradation even over prolonged operational periods.

3.3.2.2. Co-additives. The use of co-additives can be instrumental in enhancing the stability and performance of Sn perovskite solar cells by addressing the phase segregation problems induced by surplus SnX$_2$ salts. These additives interact with SnX$_2$ to create complexes, impeding phase separation and ensuring the uniform encapsulation of Sn perovskite grains. Pyrazine, renowned for its formidable binding affinity, is often engaged in the formation of complexes with SnF$_2$, resulting in the effective eradication of micrometre-sized aggregations on perovskite surfaces, thereby enhancing stability. Similarly, Wang *et al.*[374] employed HPA to mitigate phase separation in CsSnIBr$_2$ perovskite films, thereby effectively decreasing the carrier density and improving the thermal stability. Small molecules containing electronegative heteroatoms, such as piperazine, 8-hydroxyquinoline, and trimethylamine, were developed by them to enhance both the efficiency and stability. Co-additives were also employed to alleviate the phase segregation of SnCl$_2$. Yan *et al.*[375] investigated hydroxybenzene sulfonic acid or salt to establish a robust coordination with SnCl$_2$ for impeding phase separation and enhancing stability. Furthermore, additives such as ammonium hypophosphite (AHP) and gallic acid (GA) were incorporated to improve efficiency and stability. In particular, GA facilitated the formation of a SnCl$_2$–GA antioxidant layer, resulting in a record PCE of 9.03% for FASnI$_3$-based PSCs that also demonstrated exceptional stability exceeding 1000 h without encapsulation.

3.3.2.3. Hydrazine derivatives. Hydrazine derivatives, well-known for their potent reducing properties, have emerged as effective antioxidant agents for ASnX$_3$ perovskites. The

pioneering work of Kanatzidis *et al.*[376] utilized hydrazine vapour (N$_2$H$_4$) treatment to prevent Sn^{2+} oxidation during Sn perovskite film fabrication. The vapour reacted with SnI$_6^{2-}$ components, reducing Sn^{4+} to Sn^{2+}, thereby improving film conductivity. This treatment resulted in efficiencies of 3.89%, 1.83%, and 3.04% for MASnI$_3$, CsSnI$_3$, and CsSnBr$_3$, respectively. Similarly, hydrazine vapour treatment-modified CsSnI$_3$ films achieved a champion efficiency of 4.81%.[377] Jiang *et al.* utilized trihydrazine dihydroiodide (THDH) to fabricate an efficient FASnI$_3$-based solar cell, yielding a maximum efficiency of 8.48%.[378] Hydrazinium halide salts, which is hydrazinium iodide (HAI), offers improved stability too. Tsarev *et al.*[379] employed HAI as an additive, resulting in high-quality MASnI$_3$ films with enhanced photostability.

3.3.2.4. Alkali cations. To tackle the challenges of poor crystallinity and phase instability in FASnI$_3$ perovskites, Wu *et al.*[380] introduced a structural regulation strategy involving Cs doping. Incorporating Cs reduced lattice distortion, thereby giving the cubic structure rather than orthorhombic. This transition enhanced the UV-vis light absorption and crystalline degree, consequently improving the thermodynamic stability. As a result, there was a significant efficiency boost, reaching 6.08% with 8 mol% CsI. Similarly, Miyano *et al.*[381] investigated Rb doping in FASnI$_3$ perovskite, and found it reduced the optical bandgap and trap density. Incorporating 8 mol% Rb resulted in high-coverage Sn perovskite films and improved the device efficiency by approximately 80% compared to pristine FASnI$_3$-based devices, achieving a PCE of 5.89%.

3.3.2.5. Large-sized monovalent organic ammonium. Optimizing the crystal orientation and facilitating the formation of 2D or quasi-2D perovskite structures could be achieved by incorporating large-sized monovalent organic ammonium into the Sn perovskite lattice. This enhanced the resistance to oxygen and moisture and acted as a passivation agent, thereby

increasing the V_{oc} of Sn PSCs. For example, research conducted by Kanatzidis *et al.* demonstrated the crystallographic and photo-electric properties of $(BA)_2(MA)_{n-1}SnnI_{3n+1}$ perovskites,[382] resulting in an efficiency improvement of 5.94% for Sn PSCs. The unstable nature of Sn perovskite solar cells in the presence of oxygen has hampered their technological development to date. To address this issue, Liao *et al.* reported $(PEA)_2FA_8Sn_9I_{28}$, a low-dimensional Sn perovskite with significantly higher air stability than its 3D counterparts. The reduced degradation during air exposure was due to its increased thermodynamic stability, through encapsulating organic ligands, and the compact perovskite coating that prevents oxygen entry. Further, the perpendicular development of perovskite domains between electrodes promotes effective charge-carrier transport, resulting in power conversion efficiencies of 5.94% without additional device structural engineering. Also over 100 hours, the unencapsulated devices revealed no significant decrease in efficiency.[383] Moreover, Diau *et al.* utilized GA^+ to partially replace FA^+ in $FASnI_3$ perovskite, resulting in an efficiency of 9.6% alongside durable moisture resistance.[384] Additionally, HEA+ was employed to enlarge the unit cell of $FASnI_3$ perovskite, thereby enhancing the lattice symmetry. 5-AVA^+ could cross-link Sn perovskite crystals *via* hydrogen bonding, decelerating the crystallization rates and improving the film quality and stability.[385] Co-doping with NH_4Cl produced highly vertically oriented perovskite films, resulting in a PCE of 8.71% for Sn PSCs. Fluorine-functionalized cations, like 2-F-PEA^+ and FOE^+, can passivate $FASnI_3$ perovskite surfaces, diminishing the trap density and optimizing crystal alignment, resulting in a certified steady-state efficiency of 10.16% for Sn PSCs.[386,387]

3.3.2.6. Large-sized divalent organic ammonium. Diau *et al.* demonstrated that 1 mol% $EDAI_2$ doping in $FASnI_3$ perovskite could yield a pinhole-free morphology and increase the V_{oc} of Sn PSCs from 0.360 to 0.516 V. In addition, storage time induced lattice relaxation, prolonging the carrier lifetime and increasing the efficiency to 8.9% after 1462 h.[388] Sn perovskite films doped with PN^{2+} and TN^{2+} showed an increased coverage ratio and widened optical bandgap, thereby enhancing the device efficiency. TN-doped $FASnI_3$ exhibited higher efficiency due to the more significant blue shift in the photoluminescence peak. BEA^{2+} incorporation formed a Dion–Jacobson (DJ) phase 2D Sn perovskite, enhancing the structural stability and carrier diffusion length. Sn PSCs based on $(BEA)FA_{n-1}Sn_nI_{3n+1}$ perovskite achieved high efficiency and stability.[389] Padture *et al.* revealed that $4AMP^{2+}$ integration could form a DJ-phase 2D Sn perovskite with enhanced interlayer bonding and a longer carrier recombination lifetime. The optimized $4AMP^{2+}$ doping concentration yielded a high-efficiency Sn PSC with a V_{oc} of 0.69 V.[390,391] Although the ideal bandgap and eco-friendliness of Sn perovskites are very promising for PSCs, the short carrier diffusion length and high defect density in nominally synthesized films restrict its application. Consequently, Li *et al.* showed that Sn-based perovskite films with high-member low-dimensional Ruddlesden–Popper (RP) phases and a favoured crystal orientation distribution could achieve extended carrier diffusion lengths. The film's synthesis

relied on a molecular additive composed of phenylethylammonium cations and ideally blended halide-pseudo-halide anions. This additive could optimize the quasi-2D crystallization kinetics of Sn-based perovskites. The high-member RP film structure improved the J_{sc} and increased the PCE to 14.6%. The ITO/PEDOT/Perovskite/ICBA/BCP/Ag device exhibited near-unity shelf stability after 1000 h in nitrogen. A sample of 50 devices demonstrated remarkable reproducibility, with PCEs ranging from 13.0% to 14.6%.[392]

3.3.2.7. Lewis adduct and hydrogen bonding. Additives that induce further chemical interactions with Sn halide precursors, such as Lewis acid–base interactions and hydrogen bonding, have shown promise for reduction of the crystallization rates and the passivation of surface trap states in Sn perovskite films. For example, modulation of the crystallization rate of $MASnI_3$ perovskite was achieved by Kanatzidis *et al.* through the use of DMSO, leading to the formation of uniform and pinhole-free $MASnI_3$ films after annealing, accompanied by the attainment of an efficiency of 3.15% and a remarkable J_{sc} of 21.4 mA cm^{-2}.[393] Chen *et al.* reported the use of poly(ethylene-*co*-vinyl acetate) (EVA) as an additive to control the nucleation and orientation of $FASnI_3$ perovskite, leading to a 47.6% increase in device PCE.[394] Ning *et al.* used ammonium thiocyanate (NH_4SCN) as an additive to regulate the growth dynamics of quasi-2D intermediate phases in Sn perovskite films, resulting in improved stability.[395] Triphenylamine-based Lewis base additives were studied for their effects on $FASnI_3$ perovskite film crystallization dynamics, with CDTA enabling a significant enhancement in device PCE.[396] Moreover, the addition of PVA with hydroxyl groups into a $FASnI_3$ perovskite precursor led to an increase in V_{oc} and operational stability under continuous illumination.[397] Sn-halide perovskites use less regulated ingredients than Pb in conventional perovskite solar cells. However, even the best tin-halide perovskite thin films have a restricted carrier diffusion length and poor morphology. Jiang *et al.* developed a synthetic method to react metallic Sn and I_2 in DMSO, resulting in a well-dispersed $SnI_2 \cdot (DMSO)_x$ adduct in the precursor solution. The adduct promoted the out-of-plane crystal orientation, producing a more uniform structure in polycrystalline perovskite thin films. This method enhanced the electron-diffusion length of Sn-halide perovskite to 290 ± 20 nm, compared to 210 ± 20 nm in the reference films. An (ITO)–glass/PEDOT/tin-halide perovskite/indene-C_{60} bis-adduct (ICBA)/bathocuproine (BCP)/Ag PSC achieved a PCE of 14.6%, as validated by an independent lab. This represented an approximately 20% gain over the previous best-performing certified Sn-halide perovskite solar cells. The cells surpassed previous inorganic-active-layer-based thin-film solar cells, including those based on amorphous silicon, $Cu_2ZnSn(S/Se)_4$, and $Sb_2(S/Se)_3$.[398]

4. Disadvantages of using Sn in PSCs

Despite the numerous benefits associated with utilizing Sn in solar cells, Sn-based perovskite solar cells still face significant hurdles that must be addressed for their commercialization. As
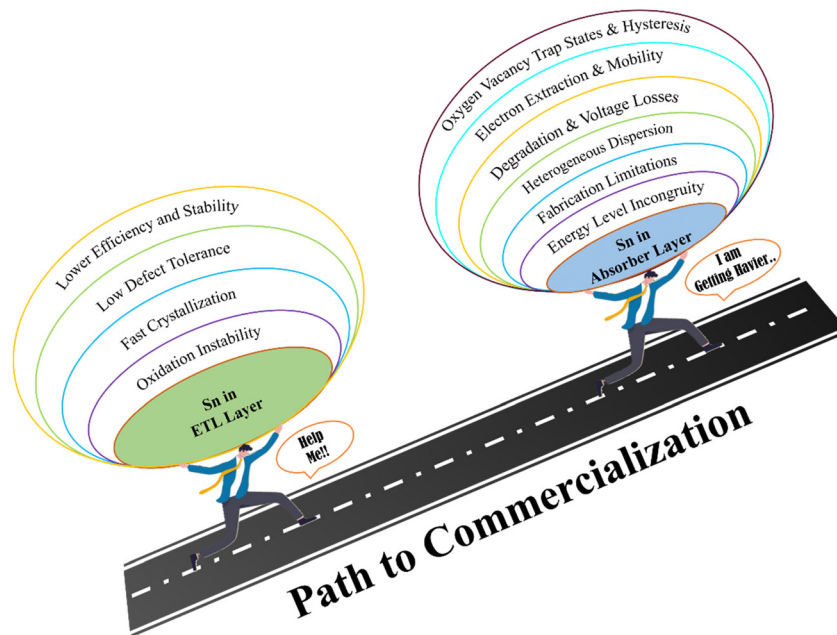
Fig. 30 Disadvantages of using Sn in the ETLs and absorber layers of MH-PSCs.

illustrated in Fig. 30, these drawbacks are evident. Below, we briefly discuss these disadvantages.

4.1. Sn in the ETL layer

4.1.1. Energy level incongruity and carrier extraction. The energy level mismatch between SnO_2 and perovskite poses a significant challenge for efficient carrier extraction. This disparity results in inefficient charge transfer and accumulation at the interface, reducing the overall device performance.[399] Nonradiative recombination processes occurring at the SnO_2–perovskite interface exacerbate these issues by facilitating the loss of photogenerated carriers before they can be collected, thereby diminishing the PCE of the solar cell.[400]

4.1.2. Heterogeneous dispersion and fabrication limitations. Commercial SnO_2 colloidal precursors often exhibit a heterogeneous dispersion, resulting in non-uniform film formation. This inconsistency in film morphology can compromise the overall device performance, particularly regarding charge transport and collection. Furthermore, the lack of efficient strategies for fabricating high-quality SnO_2 ETLs at lower temperatures presents a significant obstacle, especially for applications involving flexible plastic substrates. The inability to achieve uniform and defect-free films on flexible substrates limits the scalability and performance of flexible perovskite solar cells.[401]

4.1.3. Electron extraction and mobility. SnO_2-based ETLs face challenges in effectively extracting and transporting electrons from the perovskite layer. This inefficiency in charge extraction leads to charge accumulation and recombination within the device, resulting in a reduced photocurrent and PCE. Moreover, experiments with sputtered SnO_2 films have revealed limitations in electron mobility due to suboptimal structural configurations. These limitations contributes to inadequate

charge separation at the SnO_2–perovskite interface, further diminishing the overall performance of the solar cell.[402]

4.1.4. Fabrication process challenges. Fabrication processes for mixed-phase SnO_2 ETLs present intricate challenges that require meticulous optimization. The formation of mixed-phase structures influences the electronic properties and stability of the ETL, directly impacting device performance. Additionally, the high annealing temperatures required to achieve a favourable crystallinity in SnO_2 layers pose challenges, particularly for flexible substrate-based devices. The inability to maintain substrate integrity at elevated temperatures limits the scalability and applicability of SnO_2-based perovskite solar cells.[403]

4.1.5. Degradation and voltage losses. SnO_2 degradation during high-temperature processing introduces defects and can alter the electronic properties of the ETL, leading to increased recombination losses and decreased device efficiency. Furthermore, the incongruence of SnO_2's CB with the perovskite layer results in potential voltage losses, impacting the overall power output of the solar cell.[404]

4.1.6. Oxygen vacancy trap states and hysteresis. The presence of oxygen vacancy trap states at the surface of SnO_2 introduces additional recombination pathways for charge carriers, contributing to the hysteresis behaviour observed in devices with SnO_2 ETLs. This hysteresis phenomenon results in transient changes in device performance under varying operating conditions, leading to inaccuracies in power output measurements and reduced long-term stability.[405]

4.2. Sn in the absorber layer

4.2.1. Oxidation instability. Tin-based perovskites are highly sensitive to oxidation compared to lead-based ones. This sensitivity stems from the absence of inactive lone pairs in tin, which provide oxidative resistivity in lead-based perovskites.

The conversion of Sn^{2+} to Sn^{4+} leads to self-doping of the perovskite absorber layer, resulting in increased hole concentrations and the degradation of solar cell devices. This instability poses significant challenges for maintaining the stability and longevity of tin-based solar cells.[406]

4.2.2. Fast crystallization. Tin-based perovskites undergo rapid and uncontrollable crystallization, unlike lead-based perovskites, which allow for controlled crystallization during thermal annealing. The lack of control over crystallization during the formation process results in uneven and defective film structures with micron-sized pinholes, even at the spin-coating stage. These defects significantly limit the efficiency and performance of tin-based solar cells, impacting their overall effectiveness in converting sunlight into electricity.[407]

4.2.3. Low defect tolerance. Tin-based perovskites exhibit a low tolerance to defects compared to their lead-based counterparts. Vacancies in the Sn lattice, known as Sn vacancies, often result in deep-level defects with a low formation energy. These defects contribute to non-radiative charge recombination, which diminishes the photovoltaic performance of solar cells. The emergence of these deep-level defects leads to an average V_{oc} of around 0.4 eV for tin-based perovskite solar cells, further highlighting their inferior defect tolerance compared to lead-based alternatives.[408]

4.2.4. Lower efficiency and stability. Sn-based PSCs exhibit lower PCEs and stability than their Pb-based counterparts. While Pb-based PSCs have achieved efficiencies upwards of 15%, Sn-based PSCs lag behind at around 6.4%. Additionally, the stability of tin-based PSCs is poorer, with shorter lifespans, making them less reliable for long-term energy generation. These performance deficiencies hinder the widespread adoption of tin-based PSCs as a viable alternative to lead-based technologies.[409,410]

4.3. Environmental concerns

The integration of Sn and SnO_2 in perovskite solar cell technology brings forth critical considerations regarding both the environmental impact and toxicity, necessitating a comprehensive examination for informed decision-making. While lead-based perovskite cells have been shown to cause minimal environmental harm during the manufacturing stages, their tin-based counterparts present a contrasting scenario. The inherent attributes of tin-based cells, including their lower efficiency, heightened energy consumption in production, and increased material usage, collectively contribute to amplified environmental footprints, thereby underscoring the urgency of evaluating their sustainability from an ecological perspective.[411–413]

Moreover, comparative analyses have revealed that tin-based perovskite cells manifest heightened terrestrial ecotoxicity and contribute more substantially to global warming than lead-based alternatives. These findings not only accentuate the environmental concerns associated with tin-based solar cell technologies but also underscore the imperative to address the potential long-term repercussions they may have on ecosystems and human health. The complexities surrounding the toxicity of Sn compounds further underscore the necessity for in-depth exploration. While SnO_2 is generally perceived as less toxic than its lead-based counterparts, empirical evidence suggests nuanced toxicity concerns, particularly concerning exposure to certain Sn compounds. Studies highlight the heightened toxicity of Sn compounds like SnI_2, attributing it to acidification effects, necessitating a nuanced understanding of their environmental impact. Additionally, adverse effects observed on plant life in response to exposure to Sn-based perovskites accentuate the necessity for comprehensive ecological assessments.[414,415]

Furthermore, the toxicity profile of SnO_2 compounds warrants meticulous consideration, especially in occupational settings where exposure risks are pronounced. Chronic exposure to inorganic Sn compounds during processing may elicit respiratory and gastrointestinal symptoms, necessitating stringent safety protocols to safeguard human health and minimize environmental contamination.

5. Conclusion and future perspectives

As the landscape of SnO_2-based PSCs continues to evolve, formidable challenges remain around their stability, scalability, and hysteresis mitigation, as well as optimizing the fabrication process for the duration and cost. This has created an arena ripe for further research and innovation, shaping a trajectory toward enhanced performance and expanded applicability. The realm of SnO_2-based solar cells has already witnessed remarkable progress, marked by improved efficiencies and enhanced stability, but as we look ahead, several avenues for future advancements have emerged that can elevate the potential of SnO_2-based solar cell technology. The following outlines some potential directions that research and innovation may take:

The pursuit of higher efficiency and exceptional stability remains a cornerstone of future research endeavours. Advanced material engineering approaches, including controlled synthesis and optimization strategies, are pivotal pathways in this regard.

The refinement of SnO_2 nanocrystal synthesis techniques holds promise for fine-tuning their essential attributes, such as band structure, size, and morphology. The aim is for the resulting high-quality SnO_2 compact layers to foster enhanced light trapping and charge collection, ultimately improving overall cell performance.

Addressing the stability of SnO_2-based solar cells is essential for realizing high reproducibility and extended device lifetimes.

Harnessing novel materials and coatings is important to safeguard SnO_2 against degradation mechanisms, such as moisture and oxygen infiltration, which could significantly enhance device robustness.

Moreover, exploring advanced encapsulation techniques and developing efficient passivation layers may boost the cells' resistance to external stresses, opening new avenues for reliable long-term operation.

The translation of laboratory successes to practical applications hinges on scalable manufacturing methods. Therefore,

investigating large-scale production techniques, such as roll-to-roll manufacturing and high-quality perovskite film deposition, is critical to facilitate the fabrication of cost-effective, high-performance solar modules.

These strategies can expedite the integration of SnO_2-based solar cells into the mainstream energy landscape, enabling their widespread adoption. Using a carrier concentration-controlled SnO_2 QD ETL presents a promising route to obtaining stable, efficient, reproducible, large-scale, and flexible planar solar cells. Exploring the potential of tandem solar cells, where SnO_2-based materials can serve as a complementary component, offers the prospect of elevating overall energy-conversion efficiencies. This avenue necessitates an inclusive understanding of the intricate association between SnO_2's structure and properties, driving accurate control of the SnO_2 layers and thus promoting the holistic advancement of SnO_2-based solar cells. The future of SnO_2-based solar cells is full of exciting possibilities and challenges. As researchers delve deeper into synthesis techniques and manufacturing strategies, we are poised to witness breakthroughs that will redefine the landscape of renewable energy technology. By embracing the multidisciplinary nature of the field and fostering collaborative efforts, the vision of efficient, stable, and cost-effective SnO_2-based solar cells can transition from a concept to a tangible reality, contributing significantly to the global pursuit of sustainable energy solutions.

The future of solar energy hinges on the development of efficient and sustainable photovoltaic technologies. There are some key directions in which further advancements could be helpful to bring this technology from the lab scale to use by society, as shown in Fig. 31. Among the promising alternatives to lead-based perovskite solar cells, Sn-based perovskites have emerged as frontrunner candidates. However, several challenges must be addressed to realize their full potential and enable their widespread adoption. By integrating innovative approaches and interdisciplinary collaborations, researchers aim to overcome these obstacles and unlock the remarkable capabilities of Sn-based perovskite solar cells. The main challenge for Sn-based perovskite solar cells is achieving a higher V_{oc}. Despite achieving remarkable PCEs up to 9%, their V_{oc} remains unacceptably low, limiting their overall performance. More basic research is needed to understand the origins of the low V_{oc}, but focusing on enhancing both the V_{oc} and FF simultaneously. A V_{oc} higher than 1.0 V and an FF above 75% are critical targets to match the PCEs of Pb-based perovskite solar cells.

Another significant challenge is restraining the oxidation of Sn^{2+} ions and improving the air stability of Sn-based perovskite materials. Chemical composition and device engineering methods can help contain and control the instability issues, which would make Sn-based perovskites more commercially attractive and a viable option. Understanding whether the tendency of Sn-based halide perovskites to become hole-doped is intrinsic or extrinsic is crucial for overcoming this challenge and realizing their full potential.

Environmental impact and material stability: Sn-based perovskites, like their lead-based counterparts, can decompose upon exposure to water, releasing potentially toxic by-products. Efforts should focus on investigating the environmental impact of halide perovskite materials and developing innovative, stable, and low-toxicity alternatives. Further research is needed to understand the chemical and physical properties of Pb-free perovskite materials to fabricate improved devices and mitigate environmental concerns.

Beyond solar cells, future directions may explore applications such as LEDs, lasers, detectors, TFTs, and memory

Fig. 31 Future prospects of Sn-based ETLs and absorber layers for MH-PSCs. This schematic shows a typical approach required to make Sn PSCs an alternate viable solar energy-harvesting technology.

devices using Sn-based perovskites. Material discovery and physical studies, coupled with device engineering improvements, will enable Sn-based perovskites to realize their full potential in various applications. For materials with high "electronic" dimensionality, optimizing charge transport rather than just the physical structure will be crucial for achieving high-performance devices. Both the film quality and device architecture are vital components for achieving high-performance Sn-based perovskite solar cells. Various methods for depositing high-quality Sn-based perovskite films have been developed, such as the solvent-engineering method, which can give ultra-smooth films suitable for inverted planar structured devices.

The journey towards high-performance, Pb-free perovskite solar cells is fraught with challenges but also brimming with opportunities. As researchers delve deeper into understanding the intricacies of the material properties and device engineering, breakthroughs are on the horizon. With continuous advancements in material discovery and device optimization, the unique properties of Sn-based perovskites hold promise for revolutionizing not only solar energy but also a myriad of other technological applications.

6. Summary

In this review article, Sn has been discussed as an alternative and potential option to replace toxic Pb in PSCs. Due to toxicity concerns and the hazardous nature of lead-based potential solar cell compounds, their industrial and commercial applications are restricted, leading to the search for alternative and new options. In the search for alternative compositions, Sn-based perovskites have materialized as a favourable candidate. Sn-based perovskites have narrow band gaps, superior carrier mobilities, and offer an option for low-temperature production, in an economical process, with reduced hysteresis. Besides as absorber layers, SnO_2 have also emerged as an effective and well-performing material as an ETL. These Sn perovskites exhibit competitive PCEs while addressing the toxicity issues of Pb. This review extensively examined the incorporation of Sn within PSCs and ETL layers encompassing various dimensions, such as various synthesis techniques, attempts to fabricate Pb-free solar cell configurations, and integration into double PSCs. This provides insights and ready literature to new entrants in this research area to guide future endeavours in this field.

Author contributions

Azaharuddin Saleem Shaikh: writing – original draft, writing – review and editing. Subhash Chand Yadav: writing – original draft, writing – review and editing. Abhishek Srivastava: proof reading and editing. Archana R. Kanwade: proof reading and editing. Manish Kumar Tiwari: proof reding and editing. Shraddha Manohar Rajore: proof reading and editing. Jena Akash Kumar Satrughna: proof reading and editing. Mahesh Dhonde proof reading and editing. Parasharam M. Shirage:

formal analysis, methodology, resources, validation, writing and editing, supervision, and project administration.

Conflicts of interest

The authors declare that they have no known competing financial interests or personal relationships that could have influenced the work reported in this paper.

Acknowledgements

References

1 A. Kojima, K. Teshima, Y. Shirai and T. Miyasaka, *J. Am. Chem. Soc.*, 2009, **131**, 6050–6051.

2 F. F. Targhi, Y. S. Jalili and F. Kanjouri, *Results Phys.*, 2018, **10**, 616–627.

3 M. Ren, X. Qian, Y. Chen, T. Wang and Y. Zhao, *J. Hazard. Mater.*, 2022, **426**, 127848.

4 M. G. Ju, M. Chen, Y. Zhou, J. Dai, L. Ma, N. P. Padture and X. C. Zeng, *Joule*, 2018, **2**, 1231–1241.

5 S. F. Hoefler, G. Trimmel and T. Rath, *Monatsh. Chem.*, 2017, **148**, 795–826.

6 V. M. Goldschmidt, *Naturwissenschaften*, 1926, **14**, 477–485.

7 S. Chand Yadav, A. Srivastava, V. Manjunath, A. Kanwade, R. S. Devan and P. M. Shirage, *Mater. Today Phys.*, 2022, **26**, 100731.

8 R. Kour, S. Arya, S. Verma, J. Gupta, P. Bandhoria, V. Bharti, R. Datt and V. Gupta, *Global Challenges*, 2019, **3**, 1900050.

9 U. Farooq, M. Ishaq, U. A. Shah, S. Chen, Z. H. Zheng, M. Azam, Z. H. Su, R. Tang, P. Fan, Y. Bai and G. X. Liang, *Nano Energy*, 2022, **92**, 106710.

10 Q. Chen, N. De Marco, Y. Yang, T. Bin Song, C. C. Chen, H. Zhao, Z. Hong, H. Zhou and Y. Yang, *Nano Today*, 2015, **10**, 355–396.

11 M. Pazoki and T. Edvinsson, *Sustainable Energy Fuels*, 2018, **2**, 1430–1445.

12 X. Jiang, Z. Zang, Y. Zhou, H. Li, Q. Wei and Z. Ning, *Acc. Mater. Res.*, 2021, **2**, 210–219.

13 T. Zhu, Y. Yang and X. Gong, *ACS Appl. Mater. Interfaces*, 2020, **12**, 26776–26811.

14 W. Ke, C. C. Stoumpos and M. G. Kanatzidis, *Adv. Mater.*, 2019, **31**, 1803230.

15 W. Ayaydah, E. Raddad and Z. Hawash, *Micromachines*, 2023, **14**, 806.

16 G. K. Dalapati, H. Sharma, A. Guchhait, N. Chakrabarty, P. Bamola, Q. Liu, G. Saianand, A. M. Sai Krishna, S. Mukhopadhyay, A. Dey, T. K. S. Wong, S. Zhuk, S. Ghosh, S. Chakrabortty, C. Mahata, S. Biring, A. Kumar, C. S. Ribeiro, S. Ramakrishna, A. K. Chakraborty, S. Krishnamurthy, P. Sonar and M. Sharma, *J. Mater. Chem. A Mater.*, 2021, **9**, 16621–16684.

17 H. S. Rao, B. X. Chen, W. G. Li, Y. F. Xu, H. Y. Chen, D. Bin Kuang and C. Y. Su, *Adv. Funct. Mater.*, 2015, **25**, 7200–7207.

18 C. Liu, L. Zhang, X. Zhou, J. Gao, W. Chen, X. Wang and B. Xu, *Adv. Funct. Mater.*, 2019, **29**, 1807604.

19 D. Zhang, H. Tian, S. Bu, T. Yan, J. Ge, T. Lei, W. Bi, L. Huang and Z. Ge, *J. Alloys Compd.*, 2020, **831**, 154717.

20 L. Xiong, Y. Guo, J. Wen, H. Liu, G. Yang, P. Qin and G. Fang, *Adv. Funct. Mater.*, 2018, **28**, 1802757.

21 B. Roose, J. P. C. Baena, K. C. Gödel, M. Graetzel, A. Hagfeldt, U. Steiner and A. Abate, *Nano Energy*, 2016, **C**, 517–522.

22 Q. Jiang, L. Zhang, H. Wang, X. Yang, J. Meng, H. Liu, Z. Yin, J. Wu, X. Zhang and J. You, *Nat. Energy*, 2017, **2**, 16177.

23 Y. Yang, H. Lu, S. Feng, L. Yang, H. Dong, J. Wang, C. Tian, L. Li, H. Lu, J. Jeong, S. M. Zakeeruddin, Y. Liu, M. Grätzel and A. Hagfeldt, *Energy Environ. Sci.*, 2021, **14**, 3447–3454.

24 M. Shekargoftar, J. Pospisil, M. Kratochvíl, J. Vida, P. Souček and T. Homola, *Energy Technol.*, 2021, **9**, 2001076.

25 L. Huang, X. Zhou, R. Xue, P. Xu, S. Wang, C. Xu, W. Zeng, Y. Xiong, H. Sang and D. Liang, *Nano-Micro Lett.*, 2020, **12**, 44.

26 N. Li, J. Yan, Y. Ai, E. Jiang, L. Lin, C. Shou, B. Yan, J. Sheng and J. Ye, *Sci. China Mater.*, 2020, **63**, 207–215.

27 S. W. Lee, K. J. Choi, B. H. Kang, J. S. Lee, S. W. Kim, J. B. Kwon, S. A. Gopalan, J. H. Bae, E. S. Kim, D. H. Kwon and S. W. Kang, *Org. Electron.*, 2016, **39**, 250–257.

28 S. Y. Kim, C. C. F. Kumachang and N. Y. Doumon, *Solar RRL*, 2023, **7**, 2300155.

29 F. Li, M. Xu, X. Ma, L. Shen, L. Zhu, Y. Weng, G. Yue, F. Tan and C. Chen, *Nanoscale Res. Lett.*, 2018, **13**, 216.

30 N. Irannejad, N. Y. Nia, S. Adhami, E. Lamanna, B. Rezaei and A. Di Carlo, *Energies*, 2020, **13**, 2059.

31 Z. Song, W. Bi, X. Zhuang, Y. Wu, B. Zhang, X. Chen, C. Chen, Q. Dai and H. Song, *Sol. RRL*, 2020, **4**, 1900266.

32 B. Taheri, E. Calabrò, F. Matteocci, D. Di Girolamo, G. Cardone, A. Liscio, A. Di Carlo and F. Brunetti, *Energy Technol.*, 2020, **8**, 1901284.

33 S. Das and V. Jayaraman, *Prog. Mater. Sci.*, 2014, **66**, 112–255.

34 C. G. Granqvist, *Solar Energy Mater. Sol. Cells*, 2007, **91**, 1529–1598.

35 L. Xiong, Y. Guo, J. Wen, H. Liu, G. Yang, P. Qin and G. Fang, *Adv. Funct. Mater.*, 2018, **28**, 1802757.

36 M. K. Tiwari, S. C. Yadav, A. Srivastava, A. Kanwade, J. A. K. Satrughna, S. S. Mali, J. V. Patil, C. K. Hong and P. M. Shirage, *RSC Adv.*, 2022, **12**, 32249–32261.

37 A. S. Teja, A. Srivastava, J. A. K. Satrughna, M. K. Tiwari, A. Kanwade, S. Chand Yadav and P. M. Shirage, *Dyes Pigm.*, 2023, **210**, 110997.

38 A. Srivastava, B. Singh Chauhan, S. Chand Yadav, M. Kumar Tiwari, J. Akash Kumar Satrughna, A. Kanwade, K. Bala and P. M. Shirage, *Chem. Phys. Lett.*, 2022, **807**, 140087.

39 D. Navas, S. Fuentes, A. Castro-Alvarez and E. Chavez-Angel, *Gels*, 2021, **7**, 275.

40 A. L. Hector, *Chem. Soc. Rev.*, 2007, **36**, 1745.

41 A. Kanwade, S. Gupta, A. Kankane, M. K. Tiwari, A. Srivastava, J. A. Kumar Satrughna, S. Chand Yadav and P. M. Shirage, *RSC Adv.*, 2022, **12**, 23284–23310.

42 A. Kanwade, S. Gupta, A. Kankane, A. Srivastava, S. C. Yadav and P. M. Shirage, *Sustainable Energy Fuels*, 2022, **6**, 3114–3147.

43 V. R. Reddy Boddu, M. Palanisamy, L. Sinha, S. C. Yadav, V. G. Pol and P. M. Shirage, *Sustainable Energy Fuels*, 2021, **5**, 3219–3228.

44 Q. Dong, Y. Shi, K. Wang, Y. Li, S. Wang, H. Zhang, Y. Xing, Y. Du, X. Bai and T. Ma, *J. Phys. Chem. C*, 2015, **119**, 10212–10217.

45 W. Ke, G. Fang, Q. Liu, L. Xiong, P. Qin, H. Tao, J. Wang, H. Lei, B. Li, J. Wan, G. Yang and Y. Yan, *J. Am. Chem. Soc.*, 2015, **137**, 6730–6733.

46 Z. Zhu, Y. Bai, X. Liu, C. C. Chueh, S. Yang and A. K. Y. Jen, *Adv. Mater.*, 2016, **28**, 6478–6484.

47 H. Liu, Z. Chen, H. Wang, F. Ye, J. Ma, X. Zheng, P. Gui, L. Xiong, J. Wen and G. Fang, *J. Mater. Chem. A*, 2019, **7**, 10636–10643.

48 F. Gu, S. Fen Wang, C. Feng Song, M. Kai Lü, Y. Xin Qi, G. Jun Zhou, D. Xu and D. Rong Yuan, *Chem. Phys. Lett.*, 2003, **372**, 451–454.

49 R. Adnan, N. A. Razana, I. A. Rahman and M. A. Farrukh, *J. Chin. Chem. Soc.*, 2010, **57**, 222–229.

50 J. Zhang and L. Gao, *J. Solid State Chem.*, 2004, **177**, 1425–1430.

51 M. Aziz, S. Saber Abbas and W. R. Wan Baharom, *Mater. Lett.*, 2013, **91**, 31–34.

52 G. Yang, C. Chen, F. Yao, Z. Chen, Q. Zhang, X. Zheng, J. Ma, H. Lei, P. Qin, L. Xiong, W. Ke, G. Li, Y. Yan and G. Fang, *Adv. Mater.*, 2018, **30**, 1706023.

53 Y. Wang, C. Duan, J. Li, W. Han, M. Zhao, L. Yao, Y. Wang, C. Yan and T. Jiu, *ACS Appl. Mater. Interfaces*, 2018, **10**, 20128–20135.

54 A. H. Yuwono, F. Septiningrum, H. Nagaria, N. Sofyan, D. Dhaneswara, T. Arini, L. Andriyah, L. H. Lalasari, Y. W. Ardianto and R. W. Pawan, *EUREKA: Phys. Eng.*, 2023, 189–198.

55 S. C. Yadav, A. Sharma, R. S. Devan and P. M. Shirage, *Opt. Mater.*, 2022, **124**, 112066.

56 S. Suthakaran, S. Dhanapandian, N. Krishnakumar and N. Ponpandian, *Mater. Res. Express*, 2019, **6**, 0850i3.

57 S. Wu, H. Cao, S. Yin, X. Liu and X. Zhang, *J. Phys. Chem. C*, 2009, **113**, 17893–17898.

58 N. Talebian and H. Sadeghi Haddad Zavvare, *J. Photochem. Photobiol., B*, 2014, **130**, 132–139.

59 H. Bin Wu, J. S. Chen, X. W. David Lou and H. H. Hng, *J. Phy. Chem. C*, 2011, **115**, 24605–24610.

60 X. Wu, H. Chen, L. Gong, F. Qu and Y. Zheng, *Adv. Nat. Sci.: Nanosci. Nanotechnol.*, 2011, **2**, 035006.

61 X. Yang and L. Wang, *Mater. Lett.*, 2007, **61**, 3705–3707.

62 B. Cheng, J. M. Russell, Shi, L. Zhang and E. T. Samulski, *J. Am. Chem. Soc.*, 2004, **126**, 5972–5973.

63 M. Periyasamy and A. Kar, *J. Mater. Chem. C*, 2020, **8**, 4604–4635.

64 S. Hussain, J. Jacob, N. Riaz, K. Mahmood, A. Ali, N. Amin, G. Nabi, M. Isa and M. H. R. Mahmood, *Ceram. Int.*, 2019, **45**, 4053–4058.

65 Y. X. Li, Z. Guo, Y. Su, X. B. Jin, X. H. Tang, J. R. Huang, X. J. Huang, M. Q. Li and J. H. Liu, *ACS Sens.*, 2017, **2**, 102–110.

66 X. Yang and L. Wang, *Mater. Lett.*, 2007, **61**, 3705–3707.

67 S. Wu, H. Cao, S. Yin, X. Liu and X. Zhang, *J. Phys. Chem. C*, 2009, **113**, 17893–17898.

68 A. B. Bhise and R. B. Bhise, *Int. Res. J. Sci. Eng.*, 2018, **A2**, 192–194.

69 L. Zhang, R. Tong, W. Ge, R. Guo and S. Shirsath, *J. Alloys Compd.*, 2020, **814**, 152266.

70 H. Bin Wu, J. S. Chen, X. W. Lou and H. H. Hng, *J. Phys. Chem. C*, 2011, **115**, 24605–24610.

71 D. S. Torkhov, A. A. Burukhin, B. R. Churagulov, M. N. Rumyantseva and V. D. Maksimov, *Inorg. Mater.*, 2003, **39**, 1158–1162.

72 N. Talebian and H. S. H. Zavvare, *J. Photochem. Photobiol., B*, 2014, **130**, 132–139.

73 D. Deng and J. Y. Lee, *Chem. Mater.*, 2008, **20**, 1841–1846.

74 T. K. Nguyen, S. H. Yu, J. Yan and D. H. C. Chua, *J. Mater. Sci.*, 2020, **55**, 15588–15601.

75 P. J. Sephra, P. Baraneedharan, M. Sivakumar, T. D. Thangadurai and K. Nehru, *Mater. Res. Bull.*, 2018, **106**, 103–112.

76 D. Bekermann, D. Barreca, A. Gasparotto and C. MacCato, *Cryst. Eng. Commun.*, 2012, **14**, 6347.

77 W. Lu, C. Jiang, D. Caudle, C. Tang, Q. Sun, J. Xu and J. Song, *Phys. Chem. Chem. Phys.*, 2013, **15**, 13532.

78 M. A. Chowdhury, D. M. Nuruzzaman and M. L. Rahaman, *Int. J. Chem. React. Eng.*, 2011, **9**, 1.

79 S. Sun, G. Meng, G. Zhang and L. Zhang, *Cryst. Growth Des.*, 2007, **7**, 1988–1991.

80 L. Zhang, S. Ge and Y. Zuo, *J. Electrochem. Soc.*, 2010, **157**, K162.

81 R. Müller, F. Hernandez-Ramirez, H. Shen, H. Du, W. Mader and S. Mathur, *Chem. Mater.*, 2012, **24**, 4028–4035.

82 X.-B. Li, X.-W. Wang, Q. Shen, J. Zheng, W.-H. Liu, H. Zhao, F. Yang and H.-Q. Yang, *ACS Appl. Mater. Interfaces*, 2013, **5**, 3033–3041.

83 S. P. Mondal, S. K. Ray, J. Ravichandran and I. Manna, *Bull. Mater. Sci.*, 2010, **33**, 357–364.

84 Y. Liu, E. Koep and M. Liu, *Chem. Mater.*, 2005, **17**, 3997–4000.

85 J. B. Zhang, X. N. Li, S. L. Bai, R. X. Luo, A. F. Chen and Y. Lin, *Mater. Res. Bull.*, 2012, **47**, 3277–3282.

86 S. Mathur and S. Barth, *Small*, 2007, **3**, 2070–2075.

87 L. Zhang, S. Ge, Y. Zuo, B. Zhang and L. Xi, *J. Phys. Chem. C*, 2010, **114**, 7541–7547.

88 S. Mathur, S. Barth, H. Shen, J.-C. Pyun and U. Werner, *Small*, 2005, **1**, 713–717.

89 Z. Li, T. Zhuang, J. Dong, L. Wang, J. Xia, H. Wang, X. Cui and Z. Wang, *Ultrason. Sonochem.*, 2021, **71**, 105384.

90 Z. Li, J. Dong, H. Zhang, Y. Zhang, H. Wang, X. Cui and Z. Wang, *Nanoscale Adv.*, 2021, **3**, 41.

91 M. K. Tiwari, A. Kanwade, S. C. Yadav, A. Srivastava, J. A. K. Satrughna and P. M. Shirage, *J. Mater. Chem. C*, 2023, **11**, 5469–5480.

92 A. Sharma, A. Sharma, S. C. Yadav, A. N. Acharya, and P. M. Shirage, *Research Square*, 2023.

93 S. C. Yadav, M. K. Tiwari, A. Kanwade, H. Lee, A. Ogura and P. M. Shirage, *Electrochim. Acta*, 2023, **441**, 141793.

94 J. A. K. Satrughna, A. Kanwade, A. Srivastava, M. K. Tiwari, S. C. Yadav, S. T. Akula and P. M. Shirage, *J. Energy Storage*, 2023, **65**, 107371.

95 H. Ullah, I. Khan, Z. H. Yamani and A. Qurashi, *Ultrason. Sonochem.*, 2017, **34**, 484–490.

96 Y. C. Goswami, V. Kumar and P. Rajaram, *Mater. Lett.*, 2014, **128**, 425–428.

97 J. Zhu, Z. Lu, S. T. Aruna, D. Aurbach and A. Gedanken, *Chem. Mater.*, 2000, **12**, 2557–2566.

98 S. Zhu, D. Zhang, J. Gu, J. Xu, J. Dong and J. Li, *J. Nanopart. Res.*, 2010, **12**, 1389–1400.

99 S. Kundu, A. Kumar, S. Sen and A. Nilabh, *J. Alloys Compd.*, 2020, **818**, 152841.

100 J. Zhu, Z. Lu, S. T. Aruna, D. Aurbach and A. Gedanken, *Chem. Mater.*, 2000, **12**, 2557–2566.

101 D. N. Srivastava, S. Chappel, O. Palchik, A. Zaban and A. Gedanken, *Langmuir*, 2002, **18**, 4160–4164.

102 S. Mosadegh, Y. Mortazavi, A. A. Khodadadi and O. A. Sahraei, *Int. J. Chem. Biol. Eng.*, 2009, **2**, 2.

103 H. M. T. Albuquerque, D. C. G. A. Pinto and A. M. S. Silva, *Molecules*, 2021, **26**, 6293.

104 A. Grewal, K. Kumar, S. Redhu and S. Bhardwa, *Int. Res. J. Pharm. App. Sci.*, 2013, **3**, 278–285.

105 A. D. La Hoz, J. Alcázar, J. Carrillo, M. A. Herrero, J. D. M. Muñoz, P. Prieto, A. De Cózar and A. Diaz-Ortiz, *Microwave Heating*, 2011.

106 A. Kar, S. Kundu and A. Patra, *J. Phys. Chem. C*, 2011, **115**, 118–124.

107 A. Asdim, K. Manseki, T. Sugiura and T. Yoshida, *New J. Chem.*, 2014, **38**, 598–603.

108 A. Kar, S. Sain, S. Kundu, A. Bhattacharyya, S. Kumar Pradhan and A. Patra, *Chem. Phys. Chem.*, 2015, **16**, 1017–1025.

109 L. Zhu, M. Wang, T. Kwan Lam, C. Zhang, H. Du, B. Li and Y. Yao, *Sens. Actuators, B*, 2016, **236**, 646–653.

110 L. Xiao, H. Shen, R. von Hagen, J. Pan, L. Belkoura and S. Mathur, *Chem. Commun.*, 2010, **46**, 6509.

111 D. V. Szabó, S. Schlabach and R. Ochs, *Microsc. Microanal.*, 2007, **13**, 430–431.

112 L. Xiao, H. Shen, R. von Hagen, J. Pan, L. Belkoura and S. Mathur, *Chem. Commun.*, 2010, **46**, 6509.

113 C. Y. Yuan and D. A. Dornfeld, *J. Manuf. Sci. Eng.*, 2010, **132**, 030918.

114 D. Muñoz-Rojas, T. Maindron, A. Esteve, F. Piallat, J. Kools and J. Decams, *Mater. Today Chem.*, 2019, **12**, 96–120.

115 A. S. Subbiah, A. K. Dhara, N. Mahuli, S. Banerjee and S. K. Sarkar, *Energy Technol.*, 2019, **8**, 4.

116 E. Erdenebileg, H. Wang, J. Li, N. Singh, H. A. Dewi, N. Tiwari, N. Mathews, S. Mhaisalkar and A. Bruno, *Sol. RRL*, 2022, **6**, 2100842.

117 K. Motoyama, K. Fujii, J. Li, G. Chai, X. Wang, L. Li, G. Chai and X. Wang, *Int. J. Extreme Manuf.*, 2023, **5**, 29.

118 Y. Chen, Q. Meng, L. Zhang, C. Han, H. Gao, Y. Zhang and H. Yan, *J. Energy Chem.*, 2019, **35**, 144–167.

119 J. Lu, J. Sundqvist, M. Ottosson, A. Tarre, A. Rosental, J. Aarik and A. Hårsta, *J. Cryst. Growth*, 2004, **260**, 191–200.

120 M. J. Choi, C. J. Cho, K. C. Kim, J. J. Pyeon, H. H. Park, H. S. Kim, J. H. Han, C. G. Kim, T. M. Chung, T. J. Park, B. Kwon, D. S. Jeong, S. H. Baek, C. Y. Kang, J. S. Kim and S. K. Kim, *Appl. Surf. Sci.*, 2014, **320**, 188–194.

121 J. Sundqvist, J. Lu, M. Ottosson and A. Hårsta, *Thin Solid Films*, 2006, **514**, 63–68.

122 H.-E. Cheng, D.-C. Tian and K.-C. Huang, *Procedia Eng.*, 2012, **36**, 510–515.

123 J. Lu, J. Sundqvist, M. Ottosson, A. Tarre, A. Rosental, J. Aarik and A. Hårsta, *J. Cryst. Growth*, 2004, **260**, 191–200.

124 A. Tarre, A. Rosental, J. Sundqvist, A. Hårsta, T. Uustare and V. Sammelselg, *Surf. Sci.*, 2003, **532–535**, 514–518.

125 A. Rosental, A. Tarre, A. Gerst, J. Sundqvist, A. Hårsta, A. Aidla, J. Aarik, V. Sammelselg and T. Uustare, *Sens. Actuators, B*, 2003, **93**, 552–555.

126 J. W. Elam, D. A. Baker, A. J. Hryn, A. B. F. Martinson, M. J. Pellin and J. T. Hupp, *J. Vac. Sci. Technol., A*, 2008, **26**, 244–252.

127 D. H. Kim, J.-H. Kwon, M. Kim and S.-H. Hong, *J. Cryst. Growth*, 2011, **322**, 33–37.

128 S. Kannan Selvaraj, A. Feinerman and C. G. Takoudis, *J. Vac. Sci. Technol., A*, 2014, **32**, 01A112.

129 J. P. Correa Baena, L. Steier, W. Tress, M. Saliba, S. Neutzner, T. Matsui, F. Giordano, T. J. Jacobsson, A. R. Srimath Kandada, S. M. Zakeeruddin, A. Petrozza, A. Abate, M. K. Nazeeruddin, M. Grätzel and A. Hagfeldt, *Energy Environ. Sci.*, 2015, **8**, 2928–2934.

130 C. Wang, D. Zhao, C. R. Grice, W. Liao, Y. Yu, A. Cimaroli, N. Shrestha, P. J. Roland, J. Chen, Z. Yu, P. Liu, N. Cheng, R. J. Ellingson, X. Zhao and Y. Yan, *J. Mater. Chem. A*, 2016, **4**, 12080–12087.

131 C. Wang, C. Xiao, Y. Yu, D. Zhao, R. A. Awni, C. R. Grice, K. Ghimire, I. Constantinou, W. Liao, A. J. Cimaroli, P. Liu, J. Chen, N. J. Podraza, C. S. Jiang, M. M. Al-Jassim, X. Zhao and Y. Yan, *Adv. Energy Mater.*, 2017, **7**, 1700414.

132 C. Wang, L. Guan, D. Zhao, Y. Yu, C. R. Grice, Z. Song, R. A. Awni, J. Chen, J. Wang, X. Zhao and Y. Yan, *ACS Energy Lett.*, 2017, **2**, 2118–2124.

133 X. Li, P. Li, Z. Wu, D. Luo, H. Y. Yu and Z. H. Lu, *Mater. Rep.: Energy*, 2021, **1**, 100001.

134 G. T. Chavan, Y. Kim, M. Q. Khokhar, S. Q. Hussain, E. C. Cho, J. Yi, Z. Ahmad, P. Rosaiah and C. W. Jeon, *Nanomaterials*, 2023, **13**, 1226.

135 E. Fortunato, P. Nunes, A. Marques, D. Costa, H. Águas, I. Ferreira, M. E. V. Costa, M. H. Godinho, P. L. Almeida, J. P. Borges and R. Martins, *Surf. Coat. Technol.*, 2002, **151–152**, 247–251.

136 A. Tchenka, A. Agdad, M. C. Samba Vall, S. K. Hnawi, A. Narjis, L. Nkhaili, E. Ibnouelghazi and E. Ech-Chamikh, *Adv. Mater. Sci. Eng.*, 2021, 1687–8434.

137 A. Baptista, F. Silva, J. Porteiro, J. Míguez and G. Pinto, *Coatings*, 2018, **8**, 402.

138 Z. Z. Wu and S. Xiao, *Plasma Sources Sci. Technol.*, 2020, **29**, 113001.

139 D. Depla, S. Mahieu and J. E. Greene, *Sci. Appl. Technol.*, 2010, 253–296.

140 B. L. Zhu, X. Zhao, W. C. Hu, T. T. Li, J. Wu, Z. H. Gan, J. Liu, D. W. Zeng and C. S. Xie, *J. Alloys Compd.*, 2017, **719**, 429–437.

141 M. Ferreira, J. Loureiro, A. Nogueira, A. Rodrigues, R. Martins and I. Ferreira, *Mater. Today Proc.*, 2015, **2**, 647–653.

142 A. F. Khan, M. Mehmood, A. M. Rana, M. T. Bhatti and A. Mahmood, *Chin. Phys. Lett.*, 2009, **26**, 077803.

143 P. Venkatesh and T. S. Shyju, *Mater. Today Proc.*, 2021, **47**, 1035–1039.

144 S. Saipriya, M. Sultan and R. Singh, *Phys. B*, 2011, **406**, 812–817.

145 A. M. Serventi, D. G. Rickerby, M. C. Horrillo and R. G. Saint-Jacques, *Thin Solid Films*, 2003, **445**, 38–47.

146 M. Ruske, G. Bräuer, J. Pistner, U. Pfäfflin and J. Szczyrbowski, *Thin Solid Films*, 1999, **351**, 146–150.

147 Q. T. Khuc, X. H. Vu, D. V. Dang and D. C. Nguyen, *Adv. Nat. Sci.: Nanosci. Nanotechnol.*, 2010, **1**, 025010.

148 Y. Li, Q. Xin, L. Du, Y. Qu, H. Li, X. Kong, Q. Wang and A. Song, *Sci. Rep.*, 2016, **6**, 36183.

149 M. Di Giulio, G. Micocci, A. Serra, A. Tepore, R. Rella and P. Siciliano, *Sens. Actuators, B*, 1995, **25**, 465–468.

150 A. Alhuthali, M. M. El-Nahass, A. A. Atta, M. M. Abd El-Raheem, K. M. Elsabawy and A. M. Hassanien, *J. Lumin.*, 2015, **158**, 165–171.

151 K. Y. Park, H. J. Cho, T. K. Song, H. J. Ko and B. H. Koo, *Trans. Nonferrous Met. Soc. China*, 2014, **24**, s129–s133.

152 Y. Lian, X. Huang, J. Yu, T. B. Tang, W. Zhang and M. Gu, *AIP Adv.*, 2018, **8**, 125226.

153 Q. Zhang, P. Liu, C. Miao, Z. Chen, C. M. Lawrence Wu and C.-H. Shek, *RSC Adv.*, 2015, **5**, 39285–39290.

154 B. Gu, Y. Du, B. Chen, R. Zhao, H. Lu, Q. Xu and C. Guo, *ACS Appl. Mater. Interfaces*, 2022, **14**, 11264–11272.

155 J. Hays, A. Punnoose, R. Baldner, M. H. Engelhard, J. Peloquin and K. M. Reddy, *Phys. Rev. B*, 2005, **72**, 075203.

156 J. Haines, J. M. Léger and O. Schulte, *Science*, 1996, **271**, 629–631.

157 B. Zhu, C.-M. Liu, M.-B. Lv, X.-R. Chen, J. Zhu and G.-F. Ji, *Phys. B Condens. Matter.*, 2011, **406**, 3508–3513.

158 J.-Y. Bae, J. Park, H. Y. Kim, H.-S. Kim and J.-S. Park, *ACS Appl. Mater. Interfaces*, 2015, **7**, 12074–12079.

159 J. H. Won, S. H. Han, B. K. Park, T.-M. Chung and J. H. Han, *Coatings*, 2020, **10**, 692.

160 S. Kim, D.-H. Kim and S.-H. Hong, *J. Cryst. Growth*, 2012, **348**, 15–19.

161 F. J. Lamelas and S. A. Reid, *Phys. Rev. B: Condens. Matter Mater. Phys.*, 1999, **60**, 9347–9352.

162 Z. Chen, J. K. L. Lai and C.-H. Shek, *Appl. Phys. Lett.*, 2014, **66**, 112–255.

163 A. Saldaña-Ramírez, M. R. A. Cruz, I. Juárez-Ramírez and L. M. Torres-Martínez, *Opt. Mater*, 2020, **110**, 110501.

164 S. Ono, K. Funakoshi, A. Nozawa and T. Kikegawa, *J. Appl. Phys.*, 2005, **97**, 073523.

165 Y. Lian, X. Huang, J. Yu, T. B. Tang, W. Zhang and M. Gu, *AIP Adv.*, 2018, **8**, 125226.

166 A. F. Khan, M. Mehmood, M. Aslam and M. Ashraf, *Appl. Surf. Sci.*, 2010, **256**, 2252–2258.

167 W. Ke, G. Fang, Q. Liu, L. Xiong, P. Qin, H. Tao, J. Wang, H. Lei, B. Li, J. Wan, G. Yang and Y. Yan, *J. Am. Chem. Soc.*, 2015, **137**, 6730–6733.

168 L. Xiong, M. Qin, C. Chen, J. Wen, G. Yang, Y. Guo, J. Ma, Q. Zhang, P. Qin, S. Li and G. Fang, *Adv. Funct. Mater.*, 2018, **28**, 1706276.

169 G. Yang, C. Chen, F. Yao, Z. Chen, Q. Zhang, X. Zheng, J. Ma, H. Lei, P. Qin, L. Xiong, W. Ke, G. Li, Y. Yan and G. Fang, *Adv. Mater.*, 2018, **30**, 1706023.

170 F. J. Arlinghaus, *J. Phys. Chem. Solids*, 1974, **35**, 931–935.

171 Ph Barbarat and S. F. Matar, *Comput. Mater. Sci.*, 1998, **10**, 368–372.

172 S. Kucheyev, T. Baumann, P. Sterne, Y. Wang, T. van Buuren, A. Hamza, L. Terminello and T. Willey, *Phys. Rev. B: Condens. Matter Mater. Phys.*, 2005, **72**, 035404.

173 W. Zhou, Y. Liu, Y. Yang and P. Wu, *J. Phys. Chem. C*, 2014, **118**, 6448–6453.

174 F. Bouamra, A. Boumeddiene, M. Rérat and H. Belkhir, *Appl. Surf. Sci.*, 2013, **269**, 41–44.

175 W. Z. Xiao, G. Xiao and L. L. Wang, *J. Chem. Phys.*, 2016, **145**, 174702.

176 Y. Li, W. Yin, R. Deng, R. Chen, J. Chen, Q. Yan, B. Yao, H. Sun, S. H. Wei and T. Wu, *NPG Asia Mater.*, 2012, **4**, e30.

177 F. J. Arlinghaus, *J. Phys. Chem. Solids*, 1974, **35**, 931–935.

178 A. K. Abass and M. T. Mohammad, *J. Appl. Phys.*, 1986, **59**, 1641–1643.

179 S. J. Ikhmayies and R. N. Ahmad-Bitar, *Renewable Energy*, 2013, **49**, 143–146.

180 X. Cai, P. Zhang and S.-H. Wei, *J. Semicond.*, 2019, **40**, 092101.

181 X. Han, R. Deng, B. Sun, D. Jiang, M. Zhao, B. Yao and Y. Li, *J. Alloys Compd.*, 2021, **885**, 160974.

182 A. Slassi, M. Hammi, Z. Oumekloul, A. Nid-bahami, M. Arejdal, Y. Ziat and O. El Rhazouani, *Opt. Quantum Electron.*, 2018, **50**, 8.

183 Y. Li, J. Zhu, Y. Huang, F. Liu, M. Lv, S. Chen, L. Hu, J. Tang, J. Yao and S. Dai, *RSC Adv.*, 2015, **5**, 28424–28429.

184 J. Song, E. Zheng, J. Bian, X.-F. Wang, W. Tian, Y. Sanehira and T. Miyasaka, *J. Mater. Chem. A*, 2013, **00**, 1–3.

185 W. Ke, G. Fang, Q. Liu, L. Xiong, P. Qin, H. Tao, J. Wang, H. Lei, B. Li, J. Wan, G. Yang and Y. Yan, *J. Am. Chem. Soc.*, 2015, **137**, 6730–6733.

186 J. P. Correa Baena, L. Steier, W. Tress, M. Saliba, S. Neutzner, T. Matsui, F. Giordano, T. J. Jacobsson, A. R. Srimath Kandada, S. M. Zakeeruddin, A. Petrozza, A. Abate, M. K. Nazeeruddin, M. Grätzel and A. Hagfeldt, *Energy Environ. Sci.*, 2015, **8**, 2928–2934.

187 Q. Jiang, Z. Chu, P. Wang, X. Yang, H. Liu, Y. Wang, Z. Yin, J. Wu, X. Zhang, J. You, Q. Jiang, Z. Chu, P. Wang, X. Yang, H. Liu, Y. Wang, Z. Yin, J. Wu and X. Zhang, *Adv. Mat.*, 2017, **29**, 1703852.

188 P. Zhu, S. Gu, X. Luo, Y. Gao, S. Li, J. Zhu and H. Tan, *Adv. Energy Mater.*, 2020, **10**, 1903083.

189 L. Zhang, C. Fu, S. Wang, M. Wang, R. Wang, S. Xiang, Z. Wang, J. Liu, H. Ma, Y. Wang, Y. Yan, M. Chen, L. Shi, Q. Dong, J. Bian and Y. Shi, *Adv. Funct. Mater.*, 2023, **33**, 2213961.

190 Z. Li, Z. Wan, C. Jia, M. Zhang, M. Zhang, J. Xue, J. Shen, C. Li, C. Zhang and Z. Li, *J. Energy Chem.*, 2023, **85**, 335–342.

191 S. Ullah, M. F. U. Din, J. Khan Kasi, A. Khan Kasi, K. Vegso, M. Kotlar, M. Micusik, M. Jergel, V. Nadazdy, P. Siffalovic, E. Majkova and A. Fakharuddin, *ACS Appl. Nano Mater.*, 2022, **5**, 7822–7830.

192 Z. Xu, Y. Jiang, Z. Li, C. Chen, X. Kong, Y. Chen, G. Zhou, J. M. Liu, K. Kempa and J. Gao, *ACS Appl. Energy Mater.*, 2021, **4**, 1887–1893.

193 M. S. Kiani, Z. T. Sadirkhanov, A. G. Kakimov, H. P. Parkhomenko, A. Ng and A. N. Jumabekov, *Nanomaterials*, 2022, **12**, 2615.

194 Z. Qian, L. Chen, J. Wang, L. Wang, Y. Xia, X. Ran, P. Li, Q. Zhong, L. Song, P. Müller-Buschbaum, Y. Chen and H. Zhang, *Adv. Mater. Interfaces*, 2021, **8**, 2100128.

195 B. Taheri, E. Calabrò, F. Matteocci, D. Di Girolamo, G. Cardone, A. Liscio, A. Di Carlo and F. Brunetti, *Energy Technol.*, 2020, **8**, 1901284.

196 Z. Yelzhanova, G. Nigmetova, D. Aidarkhanov, B. Daniyar, B. Baptayev, M. P. Balanay, A. N. Jumabekov and A. Ng, *Nanomaterials*, 2022, **12**, 1686.

197 X. Zhou, W. Zhang, X. Wang, P. Lin, S. Zhou, T. Hu, L. Tian, F. Wen, G. Duan, L. Yu, Y. Xiang, B. Huang and Y. Huang, *Appl. Surf. Sci.*, 2022, **584**, 152651.

198 R. Keshtmand, M. R. Zamani-Meymian and N. Taghavinia, *Surfaces Interfaces*, 2022, **28**, 101596.

199 H. Luo, J. Wang, L. Yuan, H. Tang, L. Wu, Q. Jiang, J. Ren, M. Rao and K. Yan, *Surfaces Interfaces*, 2022, **28**, 101584.

200 A. A. Eliwi, M. Malekshahi Byranvand, P. Fassl, M. R. Khan, I. M. Hossain, M. Frericks, S. Ternes, T. Abzieher, J. A. Schwenzer, T. Mayer, J. P. Hofmann, B. S. Richards, U. Lemmer, M. Saliba and U. W. Paetzold, *Mater. Adv.*, 2022, **3**, 456–466.

201 H. Wang, H. Liu, F. Ye, Z. Chen, J. Ma, J. Liang, X. Zheng, C. Tao and G. Fang, *J. Power Sources*, 2021, **481**, 229160.

202 E. Wang, P. Chen, X. Yin, Y. Wu and W. Que, *Org. Electron.*, 2020, **84**, 105751.

203 E. H. Anaraki, A. Kermanpur, L. Steier, K. Domanski, T. Matsui, W. Tress, M. Saliba, A. Abate, M. Grätzel, A. Hagfeldt and J. P. Correa-Baena, *Energy Environ. Sci.*, 2016, **9**, 3128–3134.

204 J. Y. Chen, C. C. Chueh, Z. Zhu, W. C. Chen and A. K. Y. Jen, *Sol. Energy Mater. Sol. Cells*, 2017, **164**, 47–55.

205 Q. Jiang, L. Zhang, H. Wang, X. Yang, J. Meng, H. Liu, Z. Yin, J. Wu, X. Zhang and J. You, *Nat. Energy*, 2016, **2**, 1–7.

206 L. Zuo, H. Guo, D. W. DeQuilettes, S. Jariwala, N. De Marco, S. Dong, R. DeBlock, D. S. Ginger, B. Dunn, M. Wang and Y. Yang, *Sci. Adv.*, 2017, **3**, 1700106.

207 C. Wang, C. Xiao, Y. Yu, D. Zhao, R. Awni, C. R. Grice, K. Ghimire, W. Liao, A. J. Cimaroli, N. J. Podraza, Y. Yan, P. Liu, X. Zhao, C. Jiang, M. M. Al-Jassim and J. Chen, *Adv. Energy Mater.*, 2017, **17**, 1700414.

208 G. Yang, C. Chen, F. Yao, Z. Chen, Q. Zhang, X. Zheng, J. Ma, H. Lei, P. Qin, L. Xiong, W. Ke, G. Li, Y. Yan and G. Fang, *Adv. Mater.*, 2018, **30**, 1706023.

209 L. Lin, Z. Yang, E. Jiang, Z. Wang, J. Yan, N. Li, Z. Wang, Y. Ai, C. Shou, B. Yan, Y. Zhu, J. Sheng and J. Ye, *ACS Appl. Energy Mater.*, 2019, **2**, 7062–7069.

210 P. D. Matthews, D. J. Lewis and P. O'Brien, *J. Mater. Chem. A*, 2017, **5**, 17135–17150.

211 Q. Jiang, Z. Chu, P. Wang, X. Yang, H. Liu, Y. Wang, Z. Yin, J. Wu, X. Zhang and J. You, *Adv. Mater.*, 2017, **29**, 1703852.

212 W. Ke, G. Fang, Q. Liu, L. Xiong, P. Qin, H. Tao, J. Wang, H. Lei, B. Li, J. Wan, G. Yang and Y. Yan, *J. Am. Chem. Soc.*, 2015, **137**, 6730–6733.

213 Y. Li, J. Zhu, Y. Huang, F. Liu, M. Lv, S. Chen, L. Hu, J. Tang, J. Yao and S. Dai, *RSC Adv.*, 2015, **5**, 28424–28429.

214 C. Wang, D. Zhao, C. R. Grice, W. Liao, Y. Yu, A. Cimaroli, N. Shrestha, P. J. Roland, J. Chen, Z. Yu, P. Liu, N. Cheng, R. J. Ellingson, X. Zhao and Y. Yan, *J. Mater. Chem. A*, 2016, **4**, 12080–12087.

215 G. Yang, H. Lei, H. Tao, X. Zheng, J. Ma, Q. Liu, W. Ke, Z. Chen, L. Xiong, P. Qin, Z. Chen, M. Qin, X. Lu, Y. Yan and G. Fang, *Small*, 2017, **13**, 1601769.

216 J. A. Christians, P. Schulz, J. S. Tinkham, T. H. Schloemer, S. P. Harvey, B. J. Tremolet de Villers, A. Sellinger, J. J. Berry, J. M. Luther, J. A. Christians, P. Schulz, J. S. Tinkham, T. H. Schloemer, S. P. Harvey, B. J. Tremolet de Villers, A. Sellinger, J. J. Berry and J. M. Luther, *Nat. Energy*, 2018, **3**, 68.

217 Q. Liu, X. Zhang, C. Li, H. Lu, Z. Weng, Y. Pan, W. Chen, X.-C. Hang, Z. Sun and Y. Zhan, *Appl. Phys. Lett.*, 2019, **115**, 143903.

218 J.-J. Cao, K.-L. Wang, C. Dong, X.-M. Li, W.-F. Yang and Z.-K. Wang, *Org. Electron.*, 2021, **88**, 105972.

219 J. Liang, Z. Chen, G. Yang, H. Wang, F. Ye, C. Tao and G. Fang, *ACS Appl. Mater. Interfaces*, 2019, **11**, 23152–23159.

220 W. Gong, H. Guo, H. Zhang, J. Yang, H. Chen, L. Wang, F. Hao and X. Niu, *J. Mater. Chem. C*, 2020, **8**, 11638–11646.

221 N. Zhou, Q. Cheng, L. Li and H. Zhou, *J. Phys. D: Appl. Phys.*, 2018, **51**, 394001.

222 Y. Huang, S. Li, C. Wu, S. Wang, C. Wang and R. Ma, *Chem. Phys. Lett.*, 2020, **745**, 37220.

223 M. Park, J. Y. Kim, H. J. Son, C. H. Lee, S. S. Jang and M. J. Ko, *Nano Energy*, 2016, **26**, 208–215.

224 X. Meng, J. Deng, Q. Sun, B. Zong, Z. Zhang, B. Shen, B. Kang, S. Ravi, P. Silva and L. Wang, *J. Colloid Interface Sci.*, 2022, **609**, 547–556.

225 Q. Guo, J. Wu, Y. Yang, X. Liu, Z. Lan, J. Lin, M. Huang, Y. Wei, J. Dong, J. Jia and Y. Huang, *Research*, 2019, 4049793.

226 P. Sakthivel, S. Foo, M. Thambidurai, P. C. Harikesh, N. Mathews, R. Yuvakkumar, G. Ravi and C. Dang, *J. Power Sources*, 2020, **471**, 228443.

227 M. Spalla, E. Planes, L. Perrin, M. Matheron, S. Berson and L. Flandin, *ACS Appl. Energy Mater.*, 2019, **2**, 7183–7195.

228 C. Yang, M. Chen, J. Wang and H. Lu, *Int. J. Photoenergy*, 2021, **2021**, 1–10.

229 H. Ye, Z. Liu, X. Liu, B. Sun, X. Tan, Y. Tu, T. Shi, Z. Tang and G. Liao, *Appl. Surf. Sci.*, 2019, **478**, 417–425.

230 Y. Bai, Y. Fang, Y. Deng, Q. Wang, J. Zhao, X. Zheng, Y. Zhang and J. Huang, *ChemSusChem*, 2016, **9**, 2686–2691.

231 S. S. Mali, J. v Patil, H. Arandiyan and C. K. Hong, *J. Mater. Chem. A*, 2019, **7**, 17516–17528.

232 P. Wang, R. Li, B. Chen, F. Hou, J. Zhang, Y. Zhao and X. Zhang, *Adv. Mater.*, 2020, **32**, 1905766.

233 H. Li, G. Liu, H. Chen, W. Du, L. Ke, H. Li and C. Zhou, *Appl. Phys. Lett.*, 2022, **120**, 103502.

234 J. Ye, J. Li, A. A. Medjahed, S. Pouget, D. Aldakov, Y. Liu and P. Reiss, *Small*, 2021, **17**, 2005671.

235 W. Q. Wu, D. Chen, Y. B. Cheng and R. A. Caruso, *Sol. RRL*, 2017, **1**, 1700117.

236 C. Wang, D. Zhao, C. R. Grice, W. Liao, Y. Yu, A. Cimaroli, N. Shrestha, P. J. Roland, J. Chen, Z. Yu, P. Liu, N. Cheng, R. J. Ellingson, X. Zhao and Y. Yan, *J. Mater. Chem. A*, 2016, **4**, 12080–12087.

237 W. Ke, D. Zhao, C. Xiao, C. Wang, A. J. Cimaroli, C. R. Grice, M. Yang, Z. Li, C. S. Jiang, M. Al-Jassim, K. Zhu, M. G. Kanatzidis, G. Fang and Y. Yan, *J. Mater. Chem. A*, 2016, **4**, 14276–14283.

238 J. Xie, K. Huang, X. Yu, Z. Yang, K. Xiao, Y. Qiang, X. Zhu, L. Xu, P. Wang, C. Cui and D. Yang, *ACS Nano*, 2017, **11**, 9176–9182.

239 L. Gollino, A. Leblanc, J. Dittmer, N. Mercier and T. Pauporté, *ACS Omega*, 2023, **17**, 13.

240 S. H. Teo, C. H. Ng, Y. H. Ng, A. Islam, S. Hayase and Y. H. Taufiq-Yap, *Nano Energy*, 2022, **99**, 107401.

241 A. Srivastava, J. A. K. Satrughna, M. K. Tiwari, A. Kanwade, S. C. Yadav, K. Bala and P. M. Shirage, *Mater. Today Commun.*, 2023, **35**, 105686.

242 J. Il Kwak, S. H. Nam, L. Kim and Y. J. An, *J. Hazard. Mater.*, 2020, **392**, 122297.

243 M. Ren, X. Qian, Y. Chen, T. Wang and Y. Zhao, *J. Hazard. Mater.*, 2022, **426**, 127848.

244 C. Otero-Martínez, N. Fiuza-Maneiro and L. Polavarapu, *ACS Appl. Mater. Interfaces*, 2022, **14**, 34291.

245 T. A. Chowdhury, M. A. Bin Zafar, M. Sajjad-Ul Islam, M. Shahinuzzaman, M. A. Islam and M. U. Khandaker, *RSC Adv.*, 2023, **13**, 1787; T. T. Ava, A. Al Mamun, S. Marsillac and G. Namkoong, *Appl. Sci.*, 2019, **9**, 188.

246 S. Mazumdar, Y. Zhao and X. Zhang, *Front. Electron.*, 2021, **2**, 712785.

247 S. C. Yadav, V. Manjunath, A. Srivastava, R. S. Devan and P. M. Shirage, *Opt. Mater.*, 2022, **132**, 112676.

248 K. Yokoyama, T. Omata, S. Yokoyama and H. Takahashi, *ACS Appl. Energy Mater.*, 2023, **6**, 11070–11080.

249 Y. Yu, D. Zhao, C. R. Grice, W. Meng, C. Wang, W. Liao, A. J. Cimaroli, H. Zhang, K. Zhu and Y. Yan, *RSC Adv.*, 2016, **6**, 90248–90254.

250 S. Ippili, V. Jella, J. H. Eom, J. Kim, S. Hong, J. S. Choi, V. D. Tran, N. Van Hieu, Y. J. Kim, H. J. Kim and S. G. Yoon, *Nano Energy*, 2019, **57**, 911–923.

251 Z. Yao, Z. Yang, Y. Liu, W. Zhao, X. Zhang, B. Liu, H. Wu and S. F. Liu, *RSC Adv.*, 2017, **7**, 38155–38159.

252 W. Ke, C. C. Stoumpos, M. Zhu, L. Mao, I. Spanopoulos, J. Liu, O. Y. Kontsevoi, M. Chen, D. Sarma, Y. Zhang, M. R. Wasielewski and M. G. Kanatzidis, *Sci. Adv.*, 2017, **3**, 8.

253 Z. Chen and T. P. Dhakal, Conference Record of the IEEE Photovoltaic Specialists Conference, 2021, pp. 2430–2433.

254 X. Meng, Y. Wang, J. Lin, X. Liu, X. He, J. Barbaud, T. Wu, T. Noda, X. Yang and L. Han, *Joule*, 2020, **4**, 902–912.

255 M. E. Kayesh, T. H. Chowdhury, K. Matsuishi, R. Kaneko, S. Kazaoui, J. J. Lee, T. Noda and A. Islam, *ACS Energy Lett.*, 2018, **3**, 1584–1589.

256 J. Wang, C. Yang, H. Chen, M. Lv, T. Liu, H. Chen, D.-J. Xue, J.-S. Hu, L. Han, S. Yang and X. Meng, *ACS Energy Lett.*, 2023, **8**, 1590–1596.

257 K. Shum, Z. Chen, J. Qureshi, C. Yu, J. J. Wang, W. Pfenninger, N. Vockic, J. Midgley and J. T. Kenney, *Appl. Phys. Lett.*, 2012, 101.

258 Z. Xiao, Y. Zhou, H. Hosono and T. Kamiya, *Phys. Chem. Chem. Phys.*, 2015, **17**, 18900–18903.

259 Y. J. Kim and D.-W. Kang, *J. Mater. Chem. A*, 2022, **10**, 4782–4790.

260 F. Liu, C. Ding, Y. Zhang, T. S. Ripolles, T. Kamisaka, T. Toyoda, S. Hayase, T. Minemoto, K. Yoshino, S. Dai, M. Yanagida, H. Noguchi and Q. Shen, *J. Am. Chem. Soc.*, 2017, **139**, 16708.

261 Y. Wang, J. Tu, T. Li, C. Tao, X. Deng and Z. Li, *J. Mater. Chem. A*, 2019, **7**, 7683–7690.

262 X. Han, J. Liang, J. H. Yang, K. Soni, Q. Fang, W. Wang, J. Zhang, S. Jia, A. A. Martí, Y. Zhao and J. Lou, *Small*, 2019, **15**, 1901650.

263 X. Nairui, T. Yehua, Q. Yali, L. Duoduo and W. Ke-Fan, *Sol. Energy*, 2020, **204**, 429.

264 G. Kapil, T. Ohta, T. Koyanagi, M. Vigneshwaran, Y. Zhang, Y. Ogomi, S. S. Pandey, K. Yoshino, Q. Shen, T. Toyoda, M. M. Rahman, T. Minemoto, T. N. Murakami, H. Segawa and S. J. Hayase, *Phys. Chem. C*, 2017, **121**, 13092.

265 Y. Jiang, H. Zhang, X. Qiu and B. Cao, *Mater. Lett.*, 2017, **199**, 50.

266 J. C. R. Ke, A. S. Walton, D. J. Lewis, A. Tedstone, P. O'Brien, A. G. Thomas and W. R. Flavell, *J. Mater. Chem. A*, 2018, **00**, 1.

267 Z. Shi, J. Guo, Y. Chen, Q. Li, Y. Pan, H. Zhang, Y. D. Xia and W. Huang, *Adv. Mater.*, 2017, **29**, 1605005.

268 C. C. Stoumpos, C. D. Malliakas and M. G. Kanatzidis, *Inorg. Chem.*, 2013, **52**, 9019–9038.

269 N. K. Noel, S. D. Stranks, A. Abate, C. Wehrenfennig, S. Guarnera, A. A. Haghighirad, A. Sadhanala, G. E. Eperon, S. K. Pathak, M. B. Johnston, A. Petrozza, L. M. Herz and H. J. Snaith, *Energy Environ. Sci.*, 2014, **7**, 3061–3068.

270 M. Alla, V. Manjunath, N. Chawki, D. Singh, S. C. Yadav, M. Rouchdi and F. Boubker, *Opt. Mater.*, 2022, **124**, 112044.

271 L. Jiang, T. Orcid, L. Sun, Y. Li, A. Li, R. Orcid, K. Zou and D. Orcid, *J. Phys. Chem. C*, 2017, **121**, 24359–24364.

272 F. Hao, C. C. Stoumpos, D. H. Cao, R. P. H. Chang and M. G. Kanatzidis, *Nat. Photonics*, 2014, **8**, 489–494.

273 Y. Takahashi, R. Obara, Z.-Z. Lin, Y. Takahashi, T. Naito, T. Inabe, S. Ishibashi and K. Terakura, *Dalton Trans.*, 2011, **40**, 5563–5568.

274 Y. Takahashi, H. Hasegawa, Y. Takahashi and T. Inabe, *J. Solid-State Chem.*, 2013, **205**, 39–43.

275 D. B. Mitzi, C. A. Feild, Z. Schlesinger and R. B. Laibowitz, *J. Solid State Chem.*, 1995, **114**, 159–163.

276 Q. Zhang, F. Hao, J. Li, Y. Zhou, Y. Wei and H. Lin, *Sci. Technol. Adv. Mater.*, 2018, **19**, 425–442.

277 S. Ullah, J. Wang, P. Yang, L. Liu, J. khan, S. E. Yang, T. Xia, H. Guo and Y. Chen, *Sol. RRL*, 2021, **5**, 2000830.

278 L. Xu, X. Feng, W. Jia, W. Lv, A. Mei, Y. Zhou, Q. Zhang, R. Chen and W. Huang, *Energy Environ. Sci.*, 2021, **14**, 4292–4317.

279 L. Ma, F. Hao, C. C. Stoumpos, B. T. Phelan, M. R. Wasielewski and M. G. Kanatzidis, *J. Am. Chem. Soc.*, 2016, **138**, 14750–14755.

280 Y. Zhao and K. Zhu, *Chem. Soc. Rev.*, 2016, **45**, 655–689.

281 S. Kahmann, O. Nazarenko, S. Shao, O. Hordiichuk, M. Kepenekian, J. Even, M. V. Kovalenko, G. Blake and M. A. Loi, *ACS Energy Lett.*, 2020, **5**, 2512–2519.

282 T. M. Koh, T. Krishnamoorthy, N. Yantara, C. Shi, W. L. Leong, P. P. Boix, A. C. Grimsdale, S. G. Mhaisalkar and N. Mathews, *J. Mater. Chem. A*, 2015, **3**, 14996–15000.

283 S. J. Lee, S. S. Shin, Y. C. Kim, D. Kim, T. K. Ahn, J. H. Noh, J. Seo and S. Il Seok, *J. Am. Chem. Soc.*, 2016, **138**, 3974–3977.

284 I. Chung, J.-H. Song, J. Im, J. Androulakis, C. D. Malliakas, H. Li, A. J. Freeman, J. T. Kenney and M. G. Kanatzidis, *J. Am. Chem. Soc.*, 2012, **134**, 8579–8587.

285 F. Gu, S. Ye, Z. Zhao, H. Rao, Z. Liu, Z. Bian and C. Huang, *Sol. RRL*, 2018, **2**, 1870217.

286 F. Li, C. Zhang, J. Huang, H. Fan, H. Wang, P. Wang, C. Zhan, C. Liu, X. Li, L. Yang, Y. Song and K. Jiang, *Angew. Chem., Int. Ed.*, 2019, **58**, 6688–6692.

287 Z. Zhu, X. Jiang, D. Yu, N. Yu, Z. Ning and Q. Mi, *ACS Energy Lett.*, 2022, **7**, 2079–2083.

288 J. Chen, J. Luo and E. Hou, *Nat. Photon.*, 2024, **18**, 1–7.

289 D. Zhao, Y. Yu, C. Wang, W. Liao, N. Shrestha, C. R. Grice, A. J. Cimaroli, L. Guan, R. J. Ellingson, K. Zhu, X. Zhao, R.-G. Xiong and Y. Yan, *Nat. Energy*, 2017, **2**, 17018.

290 S. J. Lee, S. S. Shin, Y. C. Kim, D. Kim, T. K. Ahn, J. H. Noh, J. Seo and S. Il Seok, *J. Am. Chem. Soc.*, 2016, **138**, 3974–3977.

291 T. M. Koh, T. Krishnamoorthy, N. Yantara, C. Shi, W. L. Leong, P. P. Boix, A. C. Grimsdale, S. G. Mhaisalkar and N. Mathews, *J. Mater. Chem. A*, 2015, **3**, 14996–15000.

292 W. Rehman, D. P. McMeekin, J. B. Patel, R. L. Milot, M. B. Johnston, H. J. Snaith and L. M. Herz, *Energy Environ. Sci.*, 2017, **10**, 361–369.

293 D. P. McMeekin, G. Sadoughi, W. Rehman, G. E. Eperon, M. Saliba, M. T. Hörantner, A. Haghighirad, N. Sakai, L. Korte, B. Rech, M. B. Johnston, L. M. Herz and H. J. Snaith, *Science*, 2016, **351**, 151–155.

294 Z. Li and K. Zhu, *Mater. Matters*, 2018, **3**, 1.

295 S. Ašmontas and M. Mujahid, *Nanomaterials*, 2023, **13**, 1886.

296 E. M. Hutter, G. E. Eperon, S. D. Stranks and T. J. Savenije, *J. Phys. Chem. Lett.*, 2015, **6**, 3082–3090.

297 X. Meng, J. Lin, X. Liu, X. He, Y. Wang, T. Noda, T. Wu, X. Yang and L. Han, *Adv. Mater.*, 2019, **31**, 1903721.

298 Z. Zhao, F. Gu, Y. Li, W. Sun, S. Ye, H. Rao, Z. Liu, Z. Bian, C. Z. Huang Zhao, F. Gu, Y. Li, W. Sun, S. Ye, H. Rao, Z. Liu, Z. Bian and C. Huang, *Adv. Sci.*, 2017, **4**, 1700204.

299 C. Wang, Y. Zhang, F. Gu, Z. Zhao, H. Li, H. Jiang, Z. Bian and Z. Liu, *Matter.*, 2021, **4**, 709–721.

300 Y. Yu, C. R. Grice, C. Wang, A. J. Cimaroli, P. Schulz, W. Meng, K. Zhu, R. G. Xiong and Y. Yan, *Adv. Mater.*, 2016, **28**, 9333–9340.

301 C. C. Stoumpos, C. D. Malliakas and M. G. Kanatzidis, *Inorg. Chem.*, 2013, **52**, 9019–9038.

302 J. M. Frost and A. Walsh, *Acc. Chem. Res.*, 2016, **49**, 528–535.

303 Y. K. Jung, J. H. Lee, A. Walsh and A. Soon, *Chem. Mater.*, 2017, **29**, 3181–3188.

304 M. G. Ju, J. Dai, L. Ma and X. C. Zeng, *Adv. Energy Mater.*, 2017, **7**, 1700216.

305 D. Zhou, T. Zhou, Y. Tian, X. Zhu and Y. Tu, *J. Nanomater.*, 2018, **2018**, 1687.

306 M. N. Islam, J. Podder and M. L. Ali, *RSC Adv.*, 2021, **11**, 39553.

307 M. K. Hossain, M. S. Uddin, G. F. I. Toki, M. K. A. Mohammed, R. Pandey, J. Madan, Md. F. Rahman, Md. R. Islam, S. Bhattarai, H. Bencherif, D. P. Samajdar, M. Amami and D. K. Dwivedi, *RSC Adv.*, 2023, **13**, 23514–23537.

308 Q. Chen, N. De Marco, Y. Yang, T. Bin Song, C. C. Chen, H. Zhao, Z. Hong, H. Zhou and Y. Yang, *Nano Today*, 2015, **10**, 355–396.

309 M. N. Islam, J. Podder and M. L. Ali, *RSC Adv.*, 2021, **11**, 39553.

310 M. G. Ju, J. Dai, L. Ma and X. C. Zeng, *Adv. Energy Mater.*, 2017, **7**, 1700216.

311 J. M. Frost, K. T. Butler, F. Brivio, C. H. Hendon, M. Van Schilfgaarde and A. Walsh, *Nano Lett.*, 2014, **14**, 2584–2590.

312 I. Chung, J. H. Song, J. Im, J. Androulakis, C. D. Malliakas, H. Li, A. J. Freeman, J. T. Kenney and M. G. Kanatzidis, *J. Am. Chem. Soc.*, 2012, **134**, 8579–8587.

313 I. Chung, B. Lee, J. He, R. Chang, M. K. Chung, B. Lee, J. He, R. P. H. Chang and M. G. Kanatz, *Nature*, 2012, **485**(7399), 486–489.

314 K. Shum, Z. Chen, J. Qureshi, C. Yu, J. J. Wang, W. Pfenninger, N. Vockic, J. Midgley and J. T. Kenney, *Appl. Phys. Lett.*, 2010, **96**, 221903.

315 M. Konstantakou and T. Stergiopoulos, *J. Mater. Chem. A*, 2017, **5**, 11518–11549.

316 A. E. Maughan, A. M. Ganose, M. M. Bordelon, E. M. Miller, D. O. Scanlon and J. R. Neilson, *J. Am. Chem. Soc.*, 2016, **138**, 8453–8464.

317 D. Sabba, H. K. Mulmudi, R. R. Prabhakar, T. Krishnamoorthy, T. Baikie, P. P. Boix, S. Mhaisalkar and N. Mathews, *J. Phys. Chem. C*, 2015, **119**, 1763–1767.

318 Y. Wang, J. Tu, T. Li, C. Tao, X. Deng and Z. Li, *Mater. Chem. A*, 2019, **7**, 7683–7690.

319 B. Li, H. Di, B. Chang, R. Yin, L. Fu, Y.-N. Zhang and L. Yin, *Adv. Funct. Mater.*, 2021, **31**, 2007447.

320 E. Silva, J. Skelton, S. Parker and A. Walsh, *Phys. Rev. B: Condens. Matter Mater. Phys.*, 2015, **91**, 144107.

321 K. P. Marshall, M. Walker, R. I. Walton and R. A. Hatton, *Nat. Energy*, 2016, **1**, 1–9.

322 F. Hao, C. C. Stoumpos, R. P. H. Chang and M. G. Kanatzidis, *J. Am. Chem. Soc.*, 2014, **136**, 8094–8099.

323 F. Hao, C. C. Stoumpos, D. H. Cao, R. P. H. Chang and M. G. Kanatzidis, *Nat. Photonics*, 2014, **8**, 489–494.

324 T. Yokoyama, D. H. Cao, C. C. Stoumpos, T. Bin Song, Y. Sato, S. Aramaki and M. G. Kanatzidis, *J. Phys. Chem. Lett.*, 2016, **7**, 776–782.

325 M.-C. Jung, S. R. Raga and Y. Qi, *RSC Adv.*, 2016, **6**, 2819–2825.

326 X. Liu, Z. Yang, C.-C. Chueh, A. Rajagopal, S. T. Williams, Y. Sun and A. K.-Y. Jen, *J. Mater. Chem. A*, 2016, **4**, 17939–17945.

327 E. Jokar, C. H. Chien, A. Fathi, M. Rameez, Y. H. Chang and E. W. G. Diau, *Energy Environ. Sci.*, 2018, **11**, 2353–2362.

328 N. Wang, Y. Zhou, M. Ju, H. F. Garces, T. Ding, S. Pang, X. C. Zeng, N. P. Padture and X. W. Sun, *Adv. Energy Mater.*, 2016, **6**, 1601130.

329 Q. Sun, A. Gu, H. Yu, Y. Shen and M. Wang, *J. Mater. Chem. A*, 2023, **11**, 17292–17297.

330 A. E. Maughan, A. M. Ganose, M. M. Bordelon, E. M. Miller, D. O. Scanlon and J. R. Neilson, *J. Am. Chem. Soc.*, 2016, **138**, 8453–8464.

331 B. Saparov, J. P. Sun, W. Meng, Z. Xiao, H. S. Duan, O. Gunawan, D. Shin, I. G. Hill, Y. Yan and D. B. Mitzi, *Chem. Mater.*, 2016, **28**, 2315–2322.

332 J. Wang, S. Ullah, P. Yang, L. Liu, S.-E. Yang, T. Xia, H. Guo and Y. Chen, *J. Phys. D: Appl. Phys.*, 2021, **54**, 145101.

333 J. C. R. Ke, D. J. Lewis, A. S. Walton, B. F. Spencer, P. O'Brien, A. G. Thomas and W. R. Flavell, *J. Mater. Chem. A*, 2018, **6**, 11205–11214.

334 B. Saparov, J. P. Sun, W. Meng, Z. Xiao, H. S. Duan, O. D. , I. G. Hill, Y. Yan and D. B. Mitzi, *Chem. Mater.*, 2016, **28**, 2315–2322.

335 B. Lee, A. Krenselewski, S. Il Baik, D. N. Seidman and R. P. H. Chang, *Sustainable Energy Fuels*, 2017, **1**, 710–724.

336 A. Kaltzoglou, M. Antoniadou, A. G. Kontos, C. C. Stoumpos, D. Perganti, E. Siranidi, V. Raptis, K. Trohidou, V. Psycharis, M. G. Kanatzidis and P. Falaras, *J. Phys. Chem. C*, 2016, **120**, 11777–11785.

337 B. Lee, C. C. Stoumpos, N. Zhou, F. Hao, C. Malliakas, C. Y. Yeh, T. J. Marks, M. G. Kanatzidis and R. P. H. Chang, *J. Am. Chem. Soc.*, 2014, **136**, 15379–15385.

338 A. E. Maughan, A. M. Ganose, M. M. Bordelon, E. M. Miller, D. O. Scanlon and J. R. Neilson, *J. Am. Chem. Soc.*, 2016, **138**, 8453–8464.

339 X. Qiu, B. Cao, S. Yuan, X. Chen, Z. Qiu, Y. Jiang, Q. Ye, H. Wang, H. Zeng, J. Liu and M. G. Kanatzidis, *Solar Energy Mater. Sol. Cells*, 2017, **159**, 227–234.

340 A. Abate, S. Paek, F. Giordano, J. P. Correa-Baena, M. Saliba, P. Gao, T. Matsui, J. Ko, S. M. Zakeeruddin, K. H. Dahmen, A. Hagfeldt, M. Grätzel and M. K. Nazeeruddin, *Energy Environ. Sci.*, 2015, **8**, 2946–2953.

341 X. Qiu, Y. Jiang, H. Zhang, Z. Qiu, S. Yuan, P. Wang and B. Cao, *Phys. Status Solidi RRL*, 2016, **10**, 587–591.

342 Y. Jiang, H. Zhang, X. Qiu and B. Cao, *Mater. Lett.*, 2017, **199**, 50–52.

343 G. Chen, B.-B. Yu, Z. Chen, Y. Zhu, Y. Wang, B. Han, X. Zhang, Z. Du, Z. He, B.-B. Yu, Y. Zhu, Y. Wang and B. Han, *Adv. Mater.*, 2021, **33**, 2102055.

344 X. Liu, T. Wu, J. Y. Chen, X. Meng, X. He, T. Noda, H. Chen, X. Yang, H. Segawa, Y. Wang and L. Han, *Energy Environ. Sci.*, 2020, **13**, 2896–2902.

345 I. C. Smith, E. T. Hoke, D. Solis-Ibarra, M. D. McGehee and H. I. Karunadasa, *Angew. Chem., Int. Ed.*, 2014, **53**, 11232–11235.

346 E. Aktas, N. Rajamanickam, J. Pascual, S. Hu, M. H. Aldamasy, D. Di Girolamo, W. Li, G. Nasti, E. Martínez-Ferrero, A. Wakamiya, E. Palomares and A. Abate, *Commun. Mater.*, 2022, **3**, 1–14.

347 M. Saliba, T. Matsui, J. Y. Seo, K. Domanski, J. P. Correa-Baena, M. K. Nazeeruddin, S. M. Zakeeruddin, W. Tress, A. Abate, A. Hagfeldt and M. Grätzel, *Energy Environ. Sci.*, 2016, **9**, 1989–1997.

348 F. Wang, X. Jiang, H. Chen, Y. Shang, H. Liu, J. Wei, W. Zhou, H. He, W. Liu and Z. Ning, *Joule*, 2018, **2**, 2732–2743.

349 M. Chen, M. G. Ju, H. F. Garces, A. D. Carl, L. K. Ono, Z. Hawash, Y. Zhang, T. Shen, Y. Qi, R. L. Grimm, D. Pacifici, X. C. Zeng, Y. Zhou and N. P. Padture, *Nat. Commun.*, 2019, **10**, 1–8.

350 E. Aktas, N. Rajamanickam, J. Pascual, S. Hu, M. H. Aldamasy, D. Di Girolamo, W. Li, G. Nasti, E. M. Ferrero, A. Wakamiya, E. Palomares and A. Abate, *Commun. Mater.*, 2022, **3**, 104.

351 I. Metcalf, S. Sidhik, H. Zhang, A. Agrawal, J. Persaud, J. Hou, J. Even and A. D. Mohite, *Chem. Rev.*, 2023, **123**, 9565–9652.

352 W. F. Yang, F. Igbari, Y.-H. Lou, Z.-K. Wang and L.-S. Liao, *Adv. Energy Mater.*, 2020, **10**, 1902584.

353 Y. Liu, W. Gao, C. Ran, H. Dong, N. Sun, X. Ran, Y. Xia, L. Song, Y. Chen and W. Huang, *ChemSusChem*, 2020, **13**, 6477.

354 H. Zhu, J. Ma, P. Li, S. Zang, Y. Zhang and Y. Song, *Chemistry*, 2022, **8**, 2939–2960.

355 A. Pisanu, A. Speltini, P. Quadrelli, G. Drera, L. Sangaletti and L. Malavasi, *J. Mater. Chem. C*, 2019, **7**, 7020–7026.

356 C. Ferrara, M. Patrini, A. Pisanu, P. Quadrelli, C. Milanese, C. Tealdi and L. Malavasi, *J. Mater. Chem. A*, 2017, **5**, 9391–9395.

357 X. Jiang, Z. Zang, M. Ma, J. Wang, H. Wang and Z. Ning, *ACS Photonics*, 2023, **10**, 1992–1998.

358 M. Hu, R. Nie, H. Kim, J. Wu, S. Chen, B.-W. Park, G. Kim, H.-W. Kwon and S. I. Seok, *ACS Energy Lett.*, 2021, **6**, 3555.

359 Z. Zhao, F. Gu, Y. Li, W. Sun, S. Ye, H. Rao, Z. Liu, Z. Bian and P. C. Huang, *Adv. Sci.*, 2017, **4**, 1700204.

360 T. B. Song, T. Yokoyama, J. Logsdon, M. R. Wasielewski, S. Aramaki and M. G. Kanatzidis, *ACS Appl. Energy Mater.*, 2018, **1**, 4221–4226.

361 F. Hao, C. C. Stoumpos, P. Guo, N. Zhou, T. J. Marks, R. P. H. Chang and M. G. Kanatzidis, *J. Am. Chem. Soc.*, 2015, **137**, 11445–11452.

362 C. M. Tsai, N. Mohanta, C. Y. Wang, Y. U.-P. Lin, Y. W. Yang, C. L. Wang, C.-H. Hung, E. W.-G. Diau, C. Tsai, N. Mohanta, C. Ang, Y. P. Lin, D. L. Wang, D. W. G. Diau, D. W. Yang and D. H. Hung, *Angew. Chem., Int. Ed.*, 2017, **56**, 13819–13823.

363 T. Fujihara, S. Terakawa, T. Matsushima, C. Qin, M. Yahiro and C. Adachi, *J. Mater. Chem. C*, 2017, **5**, 1121–1127.

364 W. Ke, C. C. Stoumpos, I. Spanopoulos, L. Mao, M. Chen, M. R. Wasielewski and M. G. Kanatzidis, *J. Am. Chem. Soc.*, 2017, **139**, 14800–14806.

365 Z. Zhao, F. Gu, Y. Li, W. Sun, S. Ye, H. Rao, Z. Liu, Z. Bian and C. Huang, *Adv. Sci.*, 2017, **4**, 1700204.

366 Y. Yu, D. Zhao, C. R. Grice, W. Meng, C. Wang, W. Liao, A. J. Cimaroli, H. Zhang, K. Zhu and Y. Yan, *RSC Adv.*, 2016, **6**, 90248–90254.

367 C. Ran, J. Xi, W. Gao, F. Yuan, T. Lei, B. Jiao, X. Hou and Z. Wu, *ACS Energy Lett.*, 2018, **3**, 713–721.

368 W. Liao, D. Zhao, Y. Yu, C. R. Grice, C. Wang, A. J. Cimaroli, P. Schulz, W. Meng, K. Zhu, R. G. Xiong and Y. Yan, *Adv. Mater.*, 2016, **28**, 9333–9340.

369 M. H. Kumar, S. Dharani, W. L. Leong, P. P. Boix, R. R. Prabhakar, T. Baikie, C. Shi, H. Ding, R. Ramesh, M. Asta, M. Graetzel, S. G. Mhaisalkar and N. Mathews, *Adv. Mater.*, 2014, **26**, 7122–7127.

370 M. Hemant Kumar, S. Dharani, W. Lin Leong, P. P. Boix, R. Ramanujam Prabhakar, T. Baikie, C. Shi, H. Ding, R. Ramesh, M. Asta, M. Graetzel, S. G. Mhaisalkar, N. Mathews, M. H. Kumar, S. Dharani, P. P. Boix, R. R. Prabhakar, T. Baikie, M. Graetzel, S. G. Mhaisalkar, N. Mathews, W. L. Leong, C. Shi, H. Ding, R. Ramesh and M. Asta, *Adv. Mater.*, 2014, **26**, 7122–7127.

371 W. Liao, D. Zhao, Y. Yu, C. R. Grice, C. Wang, A. J. Cimaroli, P. Schulz, W. Meng, K. Zhu, R.-G. Xiong, Y. Yan, W. Liao, D. Zhao, Y. Yu, C. R. Grice, C. Wang, A. J. Cimaroli, W. Meng, Y. Yan, R. Xiong, P. Schulz and K. Zhu, *Adv. Mater.*, 2016, **28**, 9333–9340.

372 S. J. Lee, S. S. Shin, J. Im, T. K. Ahn, J. H. Noh, N. J. Jeon, S. Il Seok and J. Seo, *ACS Energy Lett.*, 2018, **3**, 46–53.

373 X. Liu, Y. Wang, T. Wu, X. He, X. Meng, J. Barbaud, H. Chen, H. Segawa, X. Yang and L. Han, *Nat. Commun.*, 2020, **11**, 1–7.

374 W. Li, J. Li, J. Li, J. Fan, Y. Mai and L. Wang, *J. Mater. Chem. A*, 2016, **4**, 17104–17110.

375 Q. Tai, X. Guo, G. Tang, P. You, T. W. Ng, D. Shen, J. Cao, C. K. Liu, N. Wang, Y. Zhu, C. S. Lee and F. Yan, *Angew. Chem., Int. Ed.*, 2019, **58**, 806–810.

376 T. Bin Song, T. Yokoyama, C. C. Stoumpos, J. Logsdon, D. H. Cao, M. R. Wasielewski, S. Aramaki and M. G. Kanatzidis, *J. Am. Chem. Soc.*, 2017, **139**, 836–842.

377 T. Bin Song, T. Yokoyama, S. Aramaki and M. G. Kanatzidis, *ACS Energy Lett.*, 2017, **2**, 897–903.

378 F. Li, H. Fan, J. Zhang, J. H. Huang, P. Wang, C. Gao, L. M. Yang, Z. Zhu, A. K. Y. Jen, Y. Song and K. J. Jiang, *Sol. RRL*, 2019, **3**, 1900285.

379 S. Tsarev, A. G. Boldyreva, S. Y. Luchkin, M. Elshobaki, M. I. Afanasov, K. J. Stevenson and P. A. Troshin, *J. Mater. Chem. A*, 2018, **6**, 21389–21395.

380 W. Gao, C. Ran, J. Li, H. Dong, B. Jiao, L. Zhang, X. Lan, X. Hou and Z. Wu, *J. Phys. Chem. Lett.*, 2018, **9**, 6999–7006.

381 D. B. Khadka, Y. Shirai, M. Yanagida and K. Miyano, *J. Mater. Chem. C*, 2020, **8**, 2307–2313.

382 D. H. Cao, C. C. Stoumpos, T. Yokoyama, J. L. Logsdon, T. Bin Song, O. K. Farha, M. R. Wasielewski, J. T. Hupp and M. G. Kanatzidis, *ACS Energy Lett.*, 2017, **2**, 982–990.

383 Y. Liao, H. Liu, W. Zhou, D. Yang, Y. Shang, Z. S. Orcid, B. Li, X. Jiang, L. Z. Orcid, L. N. Quan, R. Quintero-Bermudez, B. R. Sutherland, Q. Mi, E. H. Sargent and Z. Ning, *J. Am. Chem. Soc.*, 2017, **139**, 6693–6699.

384 C. Ran, W. Gao, J. Li, J. Xi, L. Li, J. Dai, Y. Yang, X. Gao, H. Dong, B. Jiao, I. Spanopoulos, C. D. Malliakas, X. Hou, M. G. Kanatzidis and Z. Wu, *Joule*, 2019, **3**, 3072–3087.

385 M. E. Kayesh, K. Matsuishi, R. Kaneko, S. Kazaoui, J. J. Lee, T. Noda and A. Islam, *ACS Energy Lett.*, 2019, **4**, 278–284.

386 X. Meng, Y. Wang, J. Lin, X. Liu, X. He, J. Barbaud, T. Wu, T. Noda, X. Yang and L. Han, *Joule*, 2020, **4**, 902–912.

387 P. Li, H. Dong, J. Xu, J. Chen, B. Jiao, X. Hou, J. Li and Z. Wu, *ACS Energy Lett.*, 2020, **5**, 2327–2334.

388 E. Jokar, C.-H. Chien, A. Fathi, M. Rameez, Y.-H. Chang and E. W.-G. Diau, *Energy Environ. Sci.*, 2018, **11**, 2353–2362.

389 W. Ke, C. C. Stoumpos, I. Spanopoulos, M. Chen, M. R. Wasielewski and M. G. Kanatzidis, *ACS Energy Lett.*, 2018, **3**, 1470–1476.

390 M. Chen, Q. Dong, F. T. Eickemeyer, Y. Liu, Z. Dai, A. D. Carl, B. Bahrami, A. H. Chowdhury, R. L. Grimm, Y. Shi, Q. Qiao, S. M. Zakeeruddin, M. Grätzel and N. P. Padture, *ACS Energy Lett.*, 2020, **5**, 2223–2230.

391 M. Chen, M.-G. Ju, M. Hu, Z. Dai, Y. Hu, Y. Rong, H. Han, X. C. Zeng, Y. Zhou and N. P. Padture, *ACS Energy Lett.*, 2019, **4**(1), 276–277.

392 H. Li, Z. Zang, Q. Wei, X. Jiang, M. Ma, Z. Xing, J. Wang, D. Yu, F. Wang, W. Zhou, K. S. Wong, P. C. Y. Chow, Y. Zhou and Z. Ning, *Sci. China: Chem.*, 2023, **66**, 459–465.

393 F. Hao, C. C. Stoumpos, P. Guo, N. Zhou, T. J. Marks, R. P. H. Chang and M. G. Kanatzidis, *J. Am. Chem. Soc.*, 2015, **137**, 11445–11452.

394 G. Liu, C. Liu, Z. Lin, J. Yang, Z. Huang, L. Tan and Y. Chen, *ACS Appl. Mater. Interfaces*, 2020, **12**, 14049–14056.

395 H. Kim, Y. H. Lee, T. Lyu, J. H. Yoo, T. Park and J. H. Oh, *J. Mater. Chem. A*, 2018, **6**, 18173–18182.

396 T. Wu, X. Liu, X. He, Y. Wang, X. Meng, T. Noda, X. Yang and L. Han, *Sci. China: Chem.*, 2020, **63**, 107–115.

397 X. Meng, J. Lin, X. Liu, X. He, Y. Wang, T. Noda, T. Wu, X. Yang and L. Han, *Adv. Mater.*, 2019, **31**, 1903721.

398 C. Jiang, H. Li, Q. Zhou, Q. Wei, M. Wei, L. Jiang, Z. Wang, Z. Peng, F. Wang, Z. Zang, K. Xu, Y. Hou, S. Teale, W. Zhou, R. Si, X. Gao, E. H. Sargent and Z. Ning, *J. Am. Chem. Soc.*, 2021, **143**, 10970–10976.

399 Y. Chen, Q. Meng, L. Zhang, C. Han, H. Gao, Y. Zhang and H. Yan, *J. Energy Chem.*, 2019, **35**, 144–167.

400 B. Roose and R. H. Friend, *Adv. Mater. Interfaces*, 2019, **6**, 1801788.

401 M. Haghighi, N. Ghazyani, S. Mahmoodpour, R. Keshtmand, A. Ghaffari, H. Luo, R. Mohammadpour, N. Taghavinia and M. Abdi-Jalebi, *Sol. RRL*, 2023, **7**, 2201080.

402 A. Uddin and H. Yi, *Sol. RRL*, 2022, **6**, 2100983.

403 L. Xiong, Y. Guo, J. Wen, H. Liu, G. Yang, P. Qin and G. Fang, *Adv. Funct. Mater.*, 2018, **28**, 1802757.

404 M. Batzill and U. Diebold, *Prog. Surf. Sci.*, 2005, **79**, 47–154.

405 A. Aftab and M. I. Ahmad, *Sol. Energy*, 2021, **216**, 26–47.

406 H. Dong, C. Ran, W. Gao, N. Sun, X. Liu, Y. Xia, Y. Chen and W. Huang, *Adv. Energy Mater.*, 2022, **12**, 2102213.

407 B. Li, B. Chang, L. Pan, Z. Li, L. Fu, Z. He and L. Yin, *ACS Energy Lett.*, 2020, **5**, 3752–3772.

408 S. A. U. Hasan, D. S. Lee, S. H. Im and K.-H. Hong, *Sol. RRL*, 2022, **4**, 1900310.

409 M. Li, F. Li, J. Gong, T. Zhang, F. Gao, W.-H. Zhang and M. Liu, *Small Structures*, 2022, **3**, 2100102.

410 N. K. Noel, S. D. Stranks, A. Abate, C. Wehrenfennig, S. Guarnera, A.-A. Haghighirad, A. Sadhanala, G. E. Eperon, S. K. Pathak, M. B. Johnston, A. Petrozza, L. M. Herz and H. J. Snaith, *Energy Environ. Sci.*, 2014, **7**, 3061.

411 Directive 2011/65/EU of the European Parliment and of the Council of 8 June 2011 on the restriction of the use of certain hazardous substances in electrical and electronic equipment, 2011.

412 N. Espinosa, L. Serrano-Luján, A. Urbina and F. C. Krebs, *Solar Energy Mater. Sol. Cells*, 2015, **137**, 303.

413 E. Voet, R. Salminen, R. Eckelman, G. Mudd, T. Norgate and R. Hischier, *Environmental Risks and Challenges and Anthropogenic Metals Flows and Cycles, UNEP*, Paris, 2013.

414 L. Li, G. Qi, C. Yuan, Y. Sun, X. Lei, H. Xu and Y. Wang, *Energy Environ. Sci.*, 2015, **8**, 1616.

415 P.-Y. Chen, J. Qi, M. T. Klug, X. Dang, P. T. Hammond and A. M. Belcher, *Energy Environ. Sci.*, 2015, **8**, 1618.